Structural analysis of the Gamma closure, northern Horda Platform

Ingrid Grendahl Vold

Master Thesis in Geosciences
Structural Geology and Tectonics
60 credits

Department of Geosciences
The Faculty of Mathematics and Natural Sciences
UNIVERSITY OF OSLO
September 2022

Structural analysis of the Gamma closure, northern Horda Platform

Supervisors: Sian Lianne Evans and Alvar Braathen

This work is published digitally through DUO – Digitale Utgivelser ved UiO
http://www.duo.uio.no/

Printed: Reprosentralen, Universitetet i Oslo

Acknowledgements

I want to express my gratitude to my principal supervisor Sian Lianne Evans and co-supervisor Alvar Braathen for their encouragement, guidance and feedback throughout this study. I would also like to thank past supervisor Mark J. Mulrooney for his contributions while employed at UiO. Secondly, I want to thank Muhamad Hassaan, Jonathon L. Osmond, and Nora Holden for their guidance and assistance with Petrel and Move software.

A personal thank you to my friends and fellow students at the Geoscience M.Sc. program at UiO for providing support and guidance and making it fun to work on my master thesis.

Finally, a most personal thank you goes to my family for motivational words, support, and encouragement throughout this process.

Ingrid Grendahl Vold

Oslo, Norway, September15th, 2022

Preface

This master's thesis (ECTS 60) is submitted to the Department of Geosciences, University of Oslo (UiO), in the candidacy of the Master of Science program Structural Geology and Tectonics (ECTS 120). The main supervisor is Postdoctoral Fellow Sian Lianne Evans together with co-supervisor Professor Alvar Braathen (UiO).

This thesis is a contribution to the University of Oslo and the Norwegian CCS Research Center (NCCS), under Task 9 – structural de-risking. The main ambition of Task 9 is to reduce the risk related to injecting and storing CO_2 on the Norwegian Continental Shelf, with a focus on the geology and faults in the Horda Platform area.

3D seismic data is courtesy of CGG, well data is courtesy of the NPD Diskos repository and the Northern Lights project (Equinor ASA, Total E&P Norge AS, and A/S Norske Shell). Software is courtesy of Schlumberger (Petrel E&P Software Platform) and Petroleum Experts (Move Suite).

Abstract

The Gamma closure, a possible CO_2 storage prospect, is located in the northern Horda Platform, northern North Sea. The Gamma closure is one of three possible storage prospects in the Smeaheia fault block, which was a suggested CO_2 storage hub in the Northern Lights Project. However, Aurora, located southwest to Smeaheia, was chosen as the primary storage target due to unacceptably large uncertainties for use at the initial storage site. Nevertheless, Smeaheia remains an important site for additional volumes of CO_2 because of its scale-up potential and location.

Within the study area and Gamma, two storage aquifers together with an overlying seal, which is a part of the Jurassic Dunlin and Viking Groups, serve as a possible CO_2 storage complex. The Gamma closure is within a fault block bordered by two thick-skinned faults (first-order), the Vette Fault Zone (VFZ) and the Øygarden Fault Complex. In addition, numerous intra-block thin-skinned (second-order) faults intersect the study area and Gamma closure. To assess their possible role for CO_2 containment and improve the geological understanding of the study area, fault geometries are determined by applying a structural geomodel created using the CGG NVG 3D seismic survey, regional 2D seismic lines, and well data. The geomodel is used to determine if across-fault juxtaposition and membrane seals are present, assess the evolution of faults, calculate gross rock volumes (GRV) and storage capacities of mapped structural closures, and finally, discuss plausible CO_2 injection points and migration pathways.

Results herein show that the first-order VFZ are N-S striking, west-dipping, and formed during the Permo-Triassic rifting (Rift Phase 1). Second-order faults show predominately NW-SE strikes, with varying dip directions, and formed during the Late Jurassic to Early Cretaceous rifting (Rift Phase 2). Overall, mapped second-order faults display low calculated throws. Gamma comprises of four structural traps, with a combined GRV of $4.5 * 10^8$ m^3, with a total storage capacity of 4.88 Mt, potentially increasing the storage capacity of the Smeaheia fault block.

Table of Contents

1 Introduction

This study provides a high-resolution geomodel, structural analysis, storage capacities of closures, and discusses possible CO_2 migration pathways in the Smeaheia fault block, with a focus on the Gamma closure. This chapter introduces the motivations behind this study, the Gamma closure, previous research on structural characterization and CO_2 containment in the proximity of the Gamma closure, and the main research objectives of this study.

1.1 Motivations and research background

In 2018, the European Commission outlined an ambitious target to reduce greenhouse gas emissions by 80 – 95% by 2050 with reference to 1990 levels (E. U. Comission, 2018). Carbon capture and storage (CCS) presents one of several technologies that can be used as a greenhouse gas mitigation action and thus help to meet this target. CCS involves the capture of CO_2 at CO_2-emitting industrial plants and transporting the CO_2 to suitable injection sites by ships or pipelines. The injection sites are located within the subsurface, for example in saline aquifers and depleted hydrocarbon fields (Intergovernmental Panel on Climate Change, 2005). CCS technologies have previously been shown to be feasible, particularly in offshore Norway both in the North Sea, through the Sleipner CO_2 sequestration project (Furre et al., 2017), and in the Barents Sea, through the Snøhvit CO_2 storage project (Hansen et al., 2013). The Sleipner and Snøhvit CCS projects provide a useful experience of industrial-scale CCS, but these projects are not integrated with the decarbonization of the European industry (Wu et al., 2021). Furthermore, current CCS projects in relation to the EU will not cover the estimated 12 Gt of CO_2 storage required to meet the climate targets set for 2050 (International Energy Agency, 2013). It is therefore desirable to discover additional CO_2 storage sites.

Possible storage sites on the Norwegian Continental Shelf (NCS) are currently evaluated under the project 'Northern Lights', with partners Equinor, Total, and Shell. The Horda platform is one of these possible sites, located in the Norwegian sector of the northern North Sea. In the first phase of the Northern Lights project, 1.5 Mt CO_2 per year over 25 years will be injected in the subsurface (Equinor, 2019). Two candidates have been evaluated for subsurface CO_2 storage within the Horda Platform by the Northern Lights project, Smeaheia, and Aurora, located in proximity to the Troll hydrocarbon field (Figure 1.1). Aurora and Smeaheia are considered because of their reservoir quality, and sufficient CO_2 storage capacities, and are already connected to the Norwegian coastline and existing subsea infrastructure (Mulrooney et al., 2020). Here, a CO_2 storage site, or a "CO_2 storage complex" is defined as an interval of rock including storage formations (saline aquifers herein) and seal formations, which can be a sum of multiple formations. Geological storage of CO_2 over time is achieved via four mechanisms of trapping, structural (both stratigraphic and structural), residual, dissolution, and mineral trapping (Ringrose et al., 2021). Structural traps may represent only one aspect of CO_2 storage in saline aquifers; however, they are easily mappable and are predictable in terms of migration pathways and accumulation points in the subsurface. Furthermore, structural traps also contain the majority of hydrocarbon accumulations globally (Nelson et al., 1999), implying that structural traps can be effective. Many structural traps are faulted, making lateral seals by juxtaposing low-permeability rocks onto higher-permeability rocks (Allan, 1989). Also, the fault rock itself can behave as a membrane seal for across-fault migration (Fisher & Knipe, 2001). Overall, structural traps overlain by thick top seals and faults providing substantial low-permeability juxtapositions against a storage formation are favored over thin seals or traps relying on fault rock membrane seals (Osmond et al., 2021).

CCS studies have undertaken structural analyses of parts of the Horda platform to identify potential subsurface CO_2 storage sites. This includes Smeaheia, a fault block bounded by two thick-skinned, N-S trending faults, the Vette fault Zone (VFZ), and the Øygarden Fault Complex (ØFC) (Figure 1.1). Here, two storage prospects, Alpha, and Beta were analyzed to discern their storage properties. However, the risk of pressure depletion within the Alpha prospect and unknown sealing properties due to Beta's juxtaposition with crystalline basement rocks across the ØFC have been observed (Mulrooney et al., 2020; Wu et al., 2021). Thus, Smeaheia was found to have unacceptably large uncertainties for use as the initial storage site for the Northern Lights project. As a result, Aurora was selected and was chosen as the primary storage target, located southwest to Smeaheia (Figure 1.1). Nevertheless, Smeaheia remains an important site for additional volumes of CO_2 because of its scale-up potential and location (Wu et al., 2021)

Approximately 20 km south of the Alpha prospect, another possible prospect, Gamma, with a suggested storage capacity of 0.15 – 3 Gt (Lothe et al., 2019), is located (Figure 1.1). Its suitability for CO_2 containment is uncertain, as only a few studies have examined the prospect (e.g., Lothe et al., 2019, Nazarian et al., 2018). Furthermore, the availability of Gamma regarding CO_2 storage was uncertain at the time of these studies, as Equinor was going to drill a hydrocarbon exploration well in the prospect in October 2019 (Lothe et al., 2019; NPD, 2019). Another objective of the drilling was to evaluate the ability of Middle and Lower Jurassic, as well as Upper Triassic reservoir rocks to store CO_2, and the sealing capacity of caprocks of interest (NPD, 2019). The results of drilling the 'Gladsheim well', or 32/4-3 S (Figure 1.1), were that the well was dry and that the reservoir quality of the Middle and Lower Jurassic reservoirs varied from moderate to very good (NPD, 2019), and as such, Gamma now offers potential for CO_2 storage.

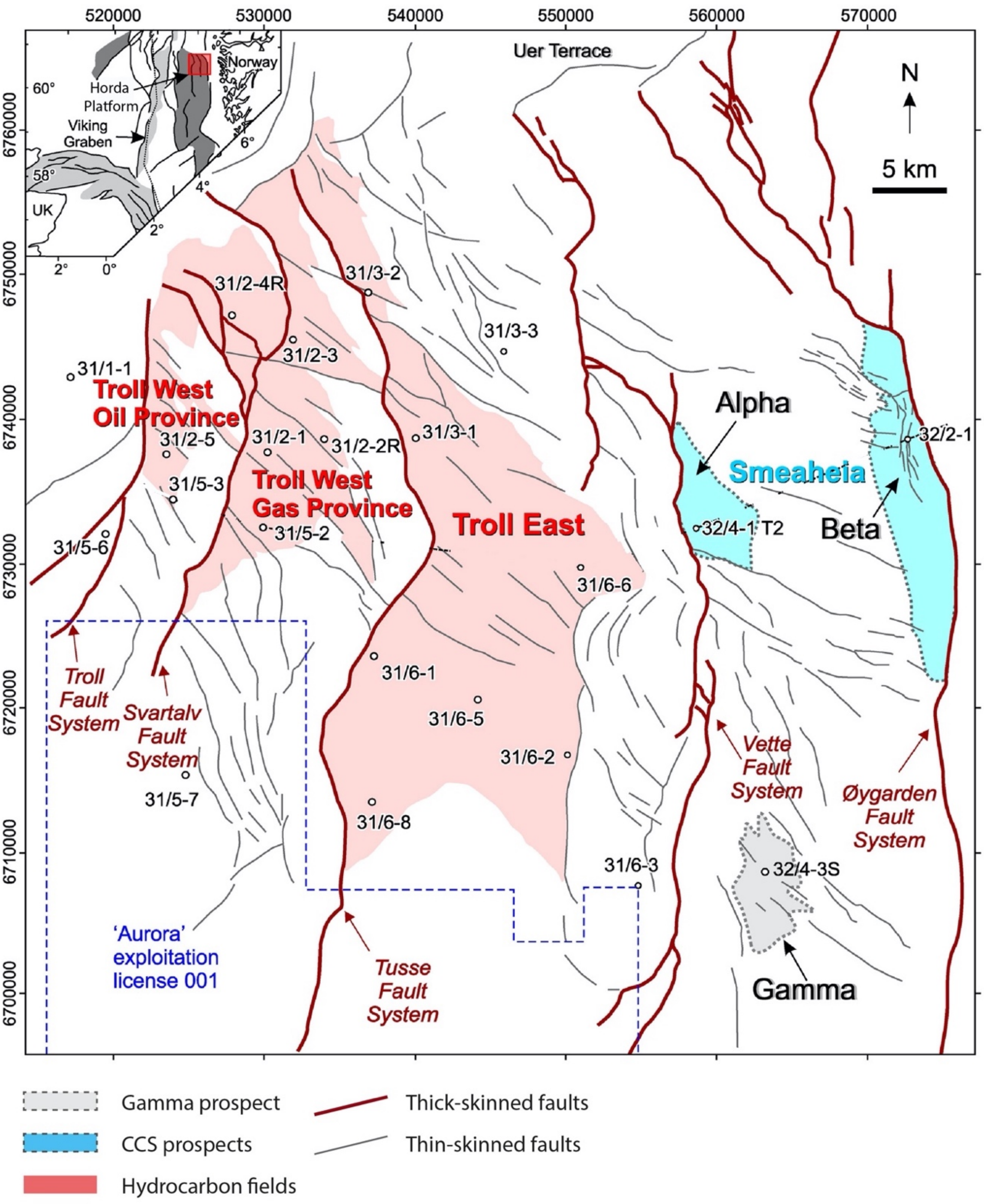

Figure 1.1. Structural map of the Horda platform area, showing the location of Gamma, CCS prospects, Aurora, and hydrocarbon fields. Note that the dark grey color in the index figure represents Permo-Triassic rifting, while the light grey color represents Jurassic rifting. The figure is taken from Wu et al. (2021) and modified.

The Gamma prospect and the northern North Sea are cut by several faults developed during multiple rift phases (Figure 1.1). Through the years, studies have been completed on the structural characterization and evolution of the faults in the northern North Sea (Færseth, 1996; Whipp et al., 2014; Ziegler, 1975). As for Smeaheia, numerous studies have been conducted regarding structural characterization, evolution, fault seal assessment, and simulations of CO_2 storage through the last years (Mulrooney et al., 2020; Nazarian et al., 2018; Osmond et al., 2021; Wu et al., 2021). However, these studies were in proximity to Gamma, and not detailed studies on the prospect itself regarding structural characterization. Nonetheless, a few studies simulated CO_2 storage in Gamma, for example, Nazarian et al. (2018), simulated storage of between 600 Mt and 3 Gt CO_2, under continuous pressure depletion from the Troll Field, while Lothe et al. (2019), simulated injection with 3 Mt per year for 50 years. Lothe et al. (2019) suggested that new interpretations of seismic reflection data in the area would provide a better representation of the structural traps than those available for the present work.

1.2 Research objectives

Meeting the need for the knowledge presented in section 1.1, i.e., to discern Gamma's suitability for CO_2 containment, the main objectives of this study are to i) generate a high-resolution structural geomodel, ii) discern if trapping structures are present, iii) discern if continuous caprock are present, iv) discern volumetric capacity of storage formations within Gamma, and v) discuss plausible CO_2 migration pathways.

Objectives will be achieved by creating a high-resolution 3D geomodel of the Cretaceous-Jurassic storage and seal units, and intersecting faults, determining lateral variations in fault throw, creating juxtaposition diagrams, conducting volumetric analysis to assess gross rock volumes and storage capacities of closures, and finally discussing possible CO_2 migration pathways to said closures. By completing these objectives, this study contributes to give a better understanding regarding the suitability for CO_2 storage in Smeaheia.

1.3 Thesis outline

The outline of this study is as follows: Chapter 2 provides background information about the geological setting, structural framework, and geological evolution in the northern North Sea in general, with a focus on the Horda platform. Chapter 3 gives an overview of theoretical concepts, data, and methods used to create a 3D geomodel and conduct volumetric and fault analysis. Chapter 4 presents the results of this study, consisting of structural and stratigraphic characterization of Gamma and the area around the prospect, and calculated gross rock volumes and storage capacities. In Chapter 5 the results are discussed and compared with previous relevant studies. Chapter 6 concludes this study by summarizing the main findings. Finally, a reference list is included at the end.

2 Geological setting

This chapter aims to place the study area and the potential storage complex into a geological context. The storage structure, i.e., the Gamma closure, is situated within the Horda Platform in the northern North Sea. The formations targeted for CO_2 injection are the Upper Jurassic Sognefjord formation in the Viking Group and the Lower Jurassic Johansen Formation within the Dunlin Group. First, the structural framework and a brief overview of the tectonic history of the North Sea and the study area will be outlined, followed by the geological evolution of these areas (Chapter 2.2).

2.1 Structural framework

The Horda platform is situated in the North Sea, which is a part of the Norwegian Continental Shelf (NCS). The NCS is in offshore Norway and consists of two other provinces in addition to the North Sea: The Mid-Norwegian continental margin to the north (60°N) and the Western Barents Sea to the northeast (75°N). The North Sea is an intracratonic rift basin, i.e., a basin located on continental crust (Bjørlykke, 2010), and is characterized by three rift arms that form a trilete junction (Davies et al., 2001); the Viking Graben, the Central Graben, and the Moray Firth Basin (Figure 2.1A). The present-day Northern North Sea's overall structure and fault pattern resulted from major rift events in the Devonian, Permo-Triassic, and Middle-Late Jurassic to Early Cretaceous (Færseth, 1996). Major listric and planar normal faults bound tilted fault-blocks and sedimentary basins: The Viking Graben, Sogn Graben, Horda Platform, Tampen Spur, and the East Shetland Basin (Færseth, 1996), and the faults strike N-S, NE-SW, and NW-SE predominately (Figure 2.1).

The Horda platform makes an approximately 300 km elongated, N-S trending structural high (Mulrooney et al., 2020) in the eastern parts of the Norwegian North Sea (Figure 2.1A), bounded to the west by the North Viking Graben and the to the east by the Øygarden Fault Complex (Figure 2.1B). The present geometry of the Horda platform is dominated by five N-S striking basement-involved faults that offset the Paleozoic, Mesozoic, and Cenozoic sedimentary succession from east to west: the Øygarden Fault Complex (ØFC) and the Vette (VFZ), Tusse, Svartalv, and Troll fault zones. These major faults dip to the west, segmenting the platform into adjacent half-graben basins associated with each fault block. The faults display throws in the 4-5 km range and is spaced ca. 15-20 km apart (Bell et al., 2014; Duffy et al., 2015; Færseth, 1996; Whipp et al., 2014). The Gamma prospect is located on the Horda Platform, in the south, within the Smeaheia fault block, between ØFC and the VFZ to the east.

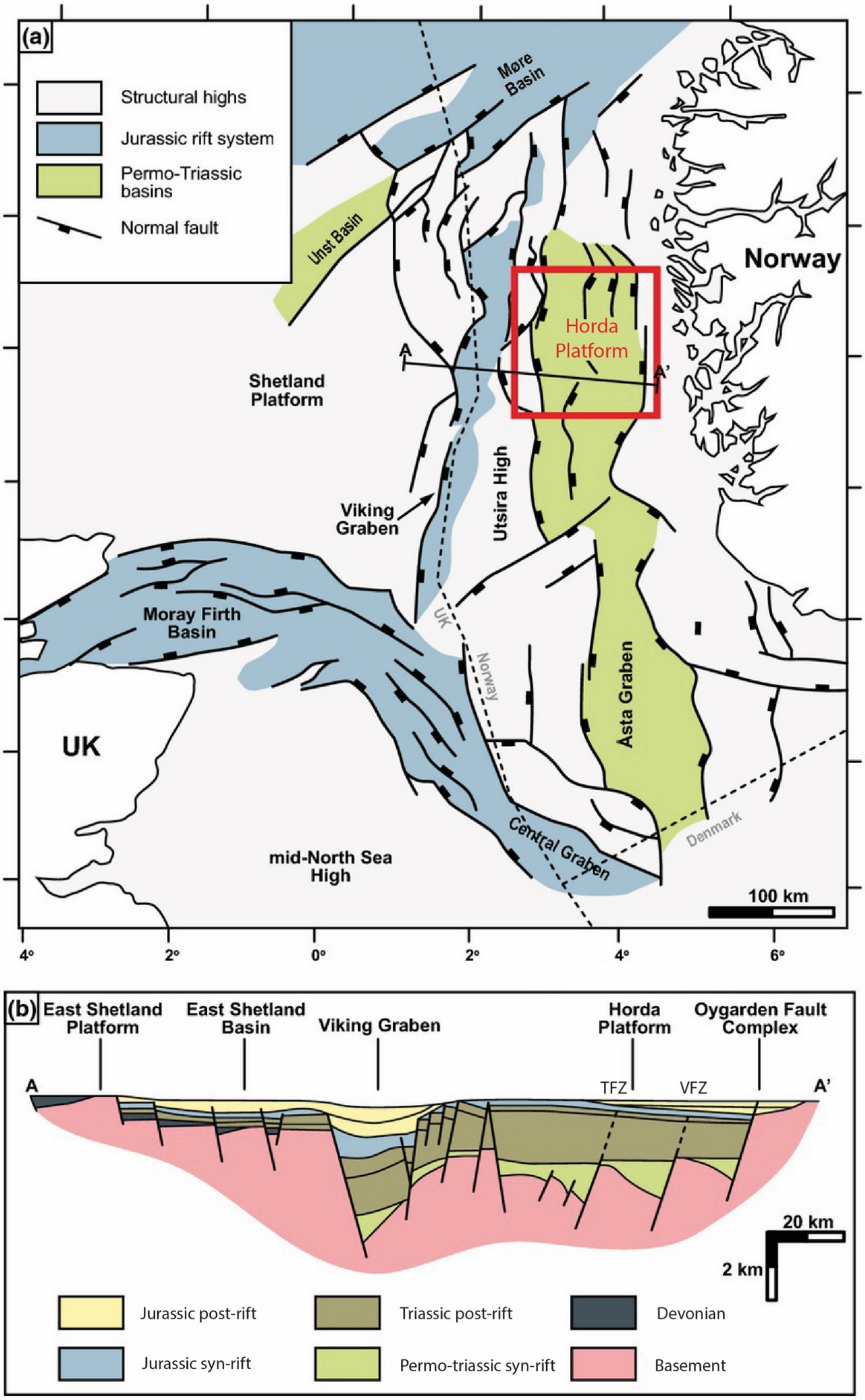

Figure 2.1. Map and cross-section showing the main structural elements of the northern North Sea Rift. The red box indicates the Horda Platform (Whipp et al., 2014).

2.2 Geological evolution

This subchapter outlines the geological evolution of the North Sea in general, from Pre-Permian to Quaternary, with a focus on the Horda Platform. A synthesis of the events described in this subchapter is provided in the stratigraphic chart in Figure 2.2.

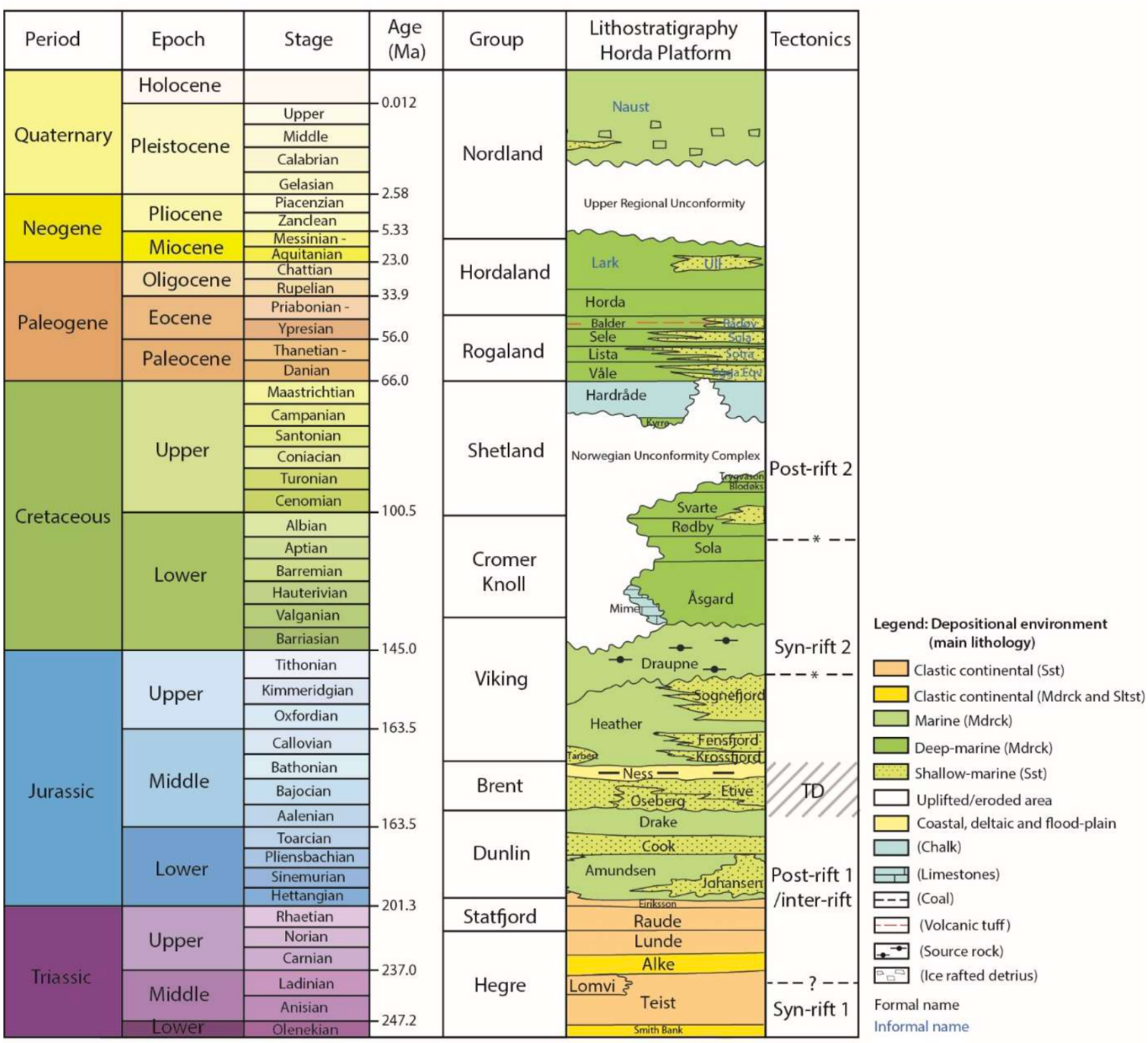

Figure 2.2. Stratigraphic chart of Triassic to Quaternary deposits in the Horda Platform (Holden, 2021). Abbreviations: TD = growth and collapse of the Central North Sea Dome, Sst = Sandstone, Mdst = Mudstone, Sltst = Siltstone.

2.2.1 Pre-Permian

The Caledonian Orogeny was a major tectonic event that led to the uplift and formation of a mountain belt spanning across western Scandinavia and Scotland, East Greenland, and a southern branch into Poland (Bjørlykke, 2010). The orogeny was initiated during the Early Ordovician with subduction along both margins of the Iapetus Ocean. It culminated in the continental collision of Laurentia and Baltica in the mid-Silurian to early Devonian (Scandian Phase) (Gee et al., 2008). The contractional tectonics during the Caledonian orogeny formed a highly heterogenous crust with structural imprints expressed as lithological layering, mylonitic fabrics, shear zones, and thrusts faults that influenced later extensional deformation in the Mesozoic (Fossen et al., 2017). Following the culmination of the Caledonian orogeny during the Devonian, gravitational collapse of Caledonian nappe stacks occurred, and pre-existing Caledonian contractional structures were exploited to form low-angle shear zone-controlled basins (Fossen, 1992; Fossen et al., 2017; Vetti & Fossen, 2012). Today, the basins outcrop in western Norway and dip toward the south, E-SE, and W-NW (Fossen, 1992; Mulrooney et al., 2020). The kilometer-scale shear zones offset the entire Caledonian nappe sequence, and extend deep into the underlying crust beneath the Northern North Sea rift (Fossen, 1992; Phillips et al., 2019). Where they are imaged in seismic reflection data they dip less than 40° and towards the E-SE and W-NW beneath the Horda platform (Fazlikhani et al., 2017). Fazlikhani et al. (2017) suggest that the northern part of VFZ links with one of these shear zones at depth.

Devonian sediments have been penetrated by wells on the Utsira High (Færseth, 1996) and the East Shetland Platform (Lervik et al., 1989), indicating that the Northern North Sea was a basin in the Devonian (Lervik, 2006). Few wells have penetrated Devonian sediments in the Northern North Sea, and thus there is not much information about the depositional environment during this period. Where the strata have been cored, conglomerates or pebbly sandstones have been found, indicating sedimentation at an early stage of basin development (Lervik, 2006).

2.2.2 Permian to Early Triassic (Rift Phase 1)

The rift architecture of the North Sea primarily evolved during the Late Permian to Early Triassic during an E-W oriented phase of extension (Rift Phase 1) (Duffy et al., 2015). Rift

Phase 1 was likely related to the breakup of Pangea, with the majority of strain accommodated by extensional faults at the rift axis centered on the Horda Platform region (130-150 m wide) (Færseth, 1996; Ter Voorde et al., 2000; Whipp et al., 2014). E-W extension occurred over an ~200 km-wide area, from the East Shetland Basin to the Northern Horda Platform and from the South Viking Graben to the Stord Basin (Phillips et al., 2019), which initiated the formation of predominately N-S striking, large displacement (3-5 km) faults that interacts with the basement (e.g., Øygarden Fault Complex, Vette, Tusse, and Svartalv Fault Zones) (Færseth, 1996; Whipp et al., 2014). The location of major depocenters and the basement-involved faults during Rift Phase 1 are suggested to have been influenced by the Devonian shear zones within the basement (Phillips et al., 2019). Estimates of the timing of Rift Phase 1 were derived from the dating of sedimentary rocks, fault rocks, and dykes, and it is suggested that the rift phase started at 261 to 225 Ma and lasted 25-37 Myr (Ter Voorde et al., 2000; Ziegler, 1982). Fault slip rates are estimated at ca. 0.1-1.5 mm/yr (Bell et al., 2014), and the stretching had a mean Beta factor (thinning factor) of 1.55 on the Horda Platform (Fazlikhani et al., 2021).

During the Triassic, the Horda Platform experienced continental conditions where sandstones and mudstones were deposited in large fluvial systems (Lervik, 2006). These sediments form the Triassic Hegre Group, which is subdivided into the Smith Banken, Teist, Alke, Lomvi, and Lunde formations (Deegan & Scull, 1977; Vollset & Doré, 1984). The sediments were deposited syn-rift, i.e., during fault activity, which resulted in wedge-shaped packages of growth strata that thicken into the hanging walls of the major faults, such as the Tusse, Vette, and Øygarden faults (Duffy et al., 2015; Phillips et al., 2019). The syn-rift wedges are estimated to be up to 3 km thick within N-S striking half grabens (Phillips et al., 2019).

2.2.3 Middle Triassic to Early Jurassic (inter-rift period)

Rift Phase 1 was followed by a period of relative tectonic quiescence and post-rift thermal subsidence (Duffy et al., 2015; Færseth, 1996). However, some faults in the North Sea Basin remained active during this period; reactivation of N-S striking Permian-Early Triassic faults and formation of NW-SE striking faults occurred in the Oseberg area in the western part of the Horda Platform (Deng et al., 2017).

During the Middle Triassic to Early Jurassic, fluvio-deltaic, shallow, and clastic marine sediments from the Norwegian and Scottish hinterlands were deposited, comprising the Statfjord, Dunlin, and Brent groups (Steel, 1993). The Late Triassic Statfjord Group consists of the Raude and Eriksson formations. It exhibits a transition from continental to shallow marine sediments, deposited in alluvial plains and later in an open marine environment (Deegan & Scull, 1977). In the Horda Platform, the Statfjord Group overlies the Lunde Formation of the Triassic Hegre Group conformably. It consists of massive, fine to coarse-grained sandstones interbedded with shales, and towards the east of the platform, the frequency of coaly shales increases (Deegan & Scull, 1977). The Early Jurassic Dunlin Group makes overlies the Statfjord Group (Deegan & Scull, 1977). The Dunlin Group is divided into four formations, from base to top: Amundsen, Burton, Cook, and Drake formations (Deegan & Scull, 1977). The group contains marine sediments deposited in prodeltaic and delta front environments, consisting of marine siltstones and shales, intercalated with thin sandstone beds in some places (Vollset & Doré, 1984). The Middle Jurassic Brent Group overlies the Dunlin Group with minor disconformity in the Brent-Statfjord area of the North Sea, but to the west and in the southern parts of the Viking Graben, it cuts down into older strata within the Dunlin Group (Vollset & Doré, 1984). The Brent group is subdivided from base to top into the Broom, Rannoch, Etive, Ness, and Tarbert formations, consisting of sediments deposited in fluviodeltaic and shallow marine environments, displaying a major regressive phase (Deegan & Scull, 1977). The group consists of sandstones, siltstones, and shales with subordinate coal beds and conglomerates (Vollset & Doré, 1984).

2.2.4 Middle Jurassic to Early Cretaceous (Rift Phase 2)

Followed by a 70 Ma period of tectonic quiescence and post-rift thermal subsidence in the North Sea Basin, Rift Phase 2 started. This phase initiated in the Middle Jurassic and continued until the Early Cretaceous (Duffy et al., 2015). Rift Phase 2 is believed to be initiated due to the Early Jurassic rise and Middle-to-Late Jurassic deflation of a thermal dome in the North Sea (Underhill & Partington, 1993). Its collapse applied regional tension, which initiated the development of the trilete North Sea system, comprised of the Viking Graben, Moray Firth, and Central Graben (Davies et al., 2001). The trilete system was further rifted by far-field tensional stresses related to North Atlantic rifting (Davies et al., 2001; Whipp et al., 2014). The initiation of Rift Phase 2 has been dated to the Bajocian (ca. 167-170 Ma) (Davies et al., 2001).

The Horda Platform experienced limited extension during the Middle Jurassic, demonstrated by no syn-rift wedges and no fault reactivation (Phillips et al., 2019), with the rift axis shifting to the adjacent Viking Graben and the Sogn Graben where the majority of the extensional strain was accommodated (Bell et al., 2014). However, in the Late Jurassic to Early Cretaceous, the Horda Platform underwent rifting again; N-S striking Permian-Triassic faults reactivated diachronously, meaning faults closest to the North Viking Graben reactivated up to 30 Myr earlier than faults at the basin margin (Bell et al., 2014). The reactivation resulted in the propagation of faults up-section into younger strata (Deng et al., 2017; Mulrooney et al., 2020). The reactivation of these faults is what characterizes Rift Phase 2. In addition to fault reactivation, a new population of NW-SE striking, 2-10 km long faults were developed. These second-order faults facilitated strain where pre-existing faults were not preferentially orientated (Færseth, 1996; Mulrooney et al., 2020), deviating in strike from Permo-Triassic faults (N-S striking). They are smaller than the Permo-Triassic and basement-involved faults, have a closer spacing (0.5-5 km), and are thin-skinned – meaning they only cut through post-Upper Jurassic sediments and not the basement rocks (Mulrooney et al., 2020). Currently, no consensus exists about the extension direction in Rift Phase 2. Some studies suggest that the strike-deviating faults are consistent with an anticlockwise rotation of the extension axis (from E-W to NE-SW) (Deng et al., 2017). However, NW-SE direction of extension and non-rotation have been postulated by previous authors (Badley et al., 1988; Bartholomew et al., 1993; Færseth, 1996). Rifting was slower and less intense than in Rift Phase 1, with slip rates of 0.01 mm/yr (Bell et al., 2014) and a mean Beta value of 1.08 (Odinsen et al., 2000).

Increased subsidence rates due to fault activity during Rift Phase 2 resulted in the development of fully marine conditions and the deposition of the Viking Group (Dreyer et al., 2005). The Viking Group consists of three stacked, regressive, shallow marine clastic sequences; the Krossfjord, Fensfjord, and Sognefjord formations (Dreyer et al., 2005). The Sognefjord Formation, the storage formation in this thesis, consists of medium to coarse-grained sandstones and sands, grey-brown in color (Vollset & Doré, 1984). The Viking Group ranges from Bathonian to Ryazanian in age (Vollset & Doré, 1984). A later, Late-Kimmeridgian to Late-Berriasian marine flooding of the North Sea basin resulted in the deposition of the Draupne Formation, a deep-marine, organic-rich sequence of mudstones (Mulrooney et al., 2020). The formation consists of dark grey-brown to black mudstone, usually non-calcareous, but carbonaceous or occasionally fissile claystone, and is characterized by very high radioactivity, often above 100 API in gamma-ray logs (Vollset & Doré, 1984). This distinct gamma-ray response marks the lower boundary of the Draupne formation, and in the northern Horda Platform, the Upper Jurassic sandstones of the Sognefjord Formation mark the base of the Draupne Formation (Vollset & Doré, 1984). In Smeaheia, Rift Phase 2 initiated during the deposition of the Draupne Formation and the Cromer Knoll Group (Whipp et al., 2014).

2.2.5 Cretaceous and Cenozoic (post-rift)

In the Early Cretaceous, rifting ceased, and a new period of thermal subsidence occurred, marked by a widespread unconformity across the North Sea basin (Badley et al., 1988). The unconformity is referred to as the northern North Sea Unconformity Complex (Kyrkjebo et al., 2004) or the Base Cretaceous or Late Cimmerian unconformity (Rawson & Riley, 1982; Ziegler, 1975), and generally marks the transition between the syn-rift (Rift Phase 2) and post-rift stages of the Jurassic-Cretaceous in the North Sea. During the Cretaceous, sea-level rise and thermal subsidence of the North Sea basin resulted in accumulations of the deep-water clastics and carbonates of the Cromer Knoll and Shetland groups (Mulrooney et al., 2020). The Cromer Knoll Group consists mainly of fine-grained marine sediments with varying calcareous material contents, including calcareous claystones, siltstones, and marlstones (Tonstad, 1989). The Shetland Group consists of limestones, marlstones, calcareous shales, and mudstones (Tonstad, 1989). The base of the Shetland Group makes the upper boundary to the Cromer Knoll Group. In the Horda Platform, the Shetland Group overlies the Cromer Knoll Group conformably, occasionally unconformably on Jurassic or older rocks (Tonstad, 1989).

In addition to thermal subsidence during the Early Cretaceous, two later episodes of uplift have been documented in the North Sea during the Cenozoic: in the early Paleogene (Late Paleocene-Early Eocene) and the late Neogene (Plio-Pleistocene) (Faleide et al., 2002). The first phase of uplift is related to rifting, magmatism, and the breakup of the North Atlantic Ocean. The second phase is associated with the isostatic response to unloading caused by erosion by glaciers during the widespread Northern Hemisphere glaciations (Faleide et al., 2002). Although, in general, the Cenozoic evolution of the North Sea basin is characterized by regional subsidence centered at the Central and Viking Grabens and infill from the elevated landmasses to the east and west (Anell et al., 2012; Faleide et al., 2002). The North Sea basin developed as an epicontinental basin during this era with up to 3 km of sedimentary fill in the central domains (Anell et al., 2012). In the Horda Platform, these sediments include the Rogaland, Hordaland, and Nordland Groups. The Rogaland Group is dominated by lithologies of sandstones interbedded with shales, deposited in a relatively deep marine environment (Tonstad, 1989). Toward the upper parts of the group, the shales become increasingly tuffaceous due to volcanic activity related to rifting and seafloor spreading between Greenland and Europe (i.e., the break-up of North-Atlantic Ocean) (Knox & Morton, 1988; Tonstad, 1989). The Hordaland Group consists of marine claystones with minor sandstones and thin limestones deposited in an open marine environment (Tonstad, 1989). The Nordland Group, the shallowest succession in the North Sea, consists of primarily marine claystones, locally silty and micaceous, deposited in an open marine environment with glacial deposits in the upper strata (Tonstad, 1989). Polygonal faults have been described in the northern North Sea, affecting a <1000 m succession of upper Eocene-middle Miocene in mudstones of the Hordaland Group (Clausen et al., 1999; Wrona et al., 2017). Their origin and the processes controlling their kinematics are poorly understood. Studies suggest that faulting commenced during the Eocene to early Oligocene, with possible reactivation occurring in the late Oligocene to middle Miocene (Wrona et al., 2017). The exact trigger for the initiation of the polygonal faults remains elusive, and their nucleation and growth have been proved not to be driven by far-field tectonic extension or gravity (Wrona et al., 2017).

3 Theory, data, and methods

In the following subchapters, the theory, methodologies, and data needed to complete a structural analysis for assessing CO_2 containment will be outlined.

3.1 Theory

To assess the feasibility of a storage site, fault evolution, and CO_2 migration pathways within the study area, it is essential to specify the theoretical background on fault geometry and across-fault seal assessment. An overview of what a storage site is and the effects of fault geometry on CO_2 migration is given and finally, fault seal types will be explained.

3.1.1 The CO_2 storage site and fault geometry

Storage of CO_2 in saline aquifers in the subsurface has been demonstrated at an industrial scale in Norway for the past 20 years (Furre et al., 2017; Hansen et al., 2013). These storage sites are often sloping, porous, and permeable reservoir rocks such as sandstones, overlain by impermeable enclosing units such as shales. The impermeable units may have no lateral confinement, meaning that injected CO_2 can migrate up-dip within the reservoir rock along the interface with the caprock, as CO_2 acts buoyant in the subsurface. The interface between caprock and reservoir provides constraints over potential CO_2 migration pathways, accumulation points, and barriers. Accumulation points, or geologic traps, is defined as 'any barrier to the upward movement of oil or gas, allowing either or both to accumulate' (Vrolijk et al., 2011). The simplest geometric form to make a geologic trap is a 4-way closure, shaped like an inverted bowl. In 4-way closures, the most important factor is whether the capillary properties of the caprock remain continuous over the entire trap (Vrolijk et al., 2011). However, geologic traps often contain faults, which adds structural complexity. Mapping these structural features and assessing strikes, dips, and lateral extents is essential in determining possible migration pathways of injected CO_2. For example, faults oriented perpendicular or obliquely to the migration direction may redirect or retard the CO_2 migration (Andersen & Sundal, 2021). The dip direction of the faults determines if the faults will act as a barrier or a conduit for across-fault migration (Miocic et al., 2019). Furthermore, CO_2 can migrate along faults to the overburden. Figure 3.1 illustrates one scenario, where the CO_2 is injected into the footwall of the fault. This fault will likely trap CO_2 until it spills into the hanging wall. Another scenario would be injecting the CO_2 into the hanging wall; the CO_2 would migrate up-dip into the footwall and not get trapped.

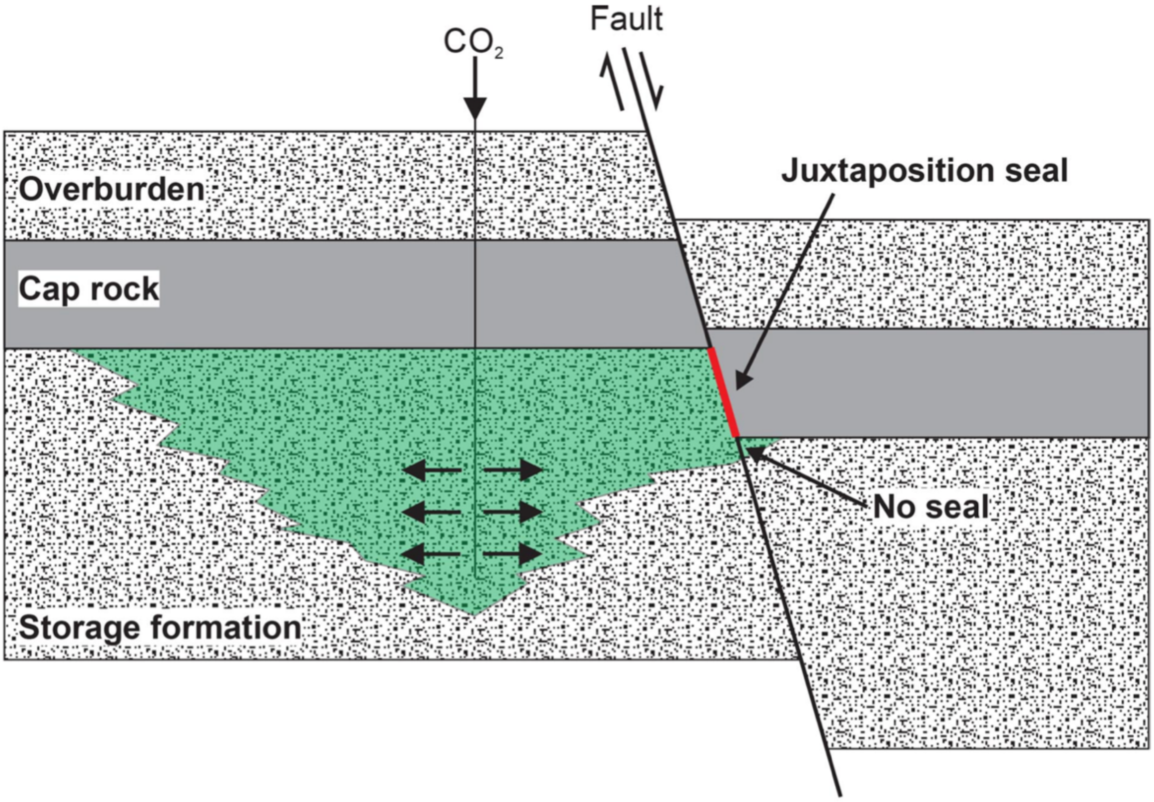

Figure 3.1. Schematic illustration of the impact of fault dip direction in a CO_2 storage site (Miocic et al., 2019). The CO_2 is injected into the footwall, resulting in a juxtaposition seal until the CO_2 reaches the spill point, resulting in further migration into the hanging wall.

3.1.1.1 Fault growth and throw

There are currently two often-used models describing the growth of normal faults, termed ‘propagating’ and ‘constant’ length fault models (Fossen & Rotevatn, 2016; Jackson et al., 2017; Nicol et al., 2005; Walsh et al., 2002). The propagating model (also referred to as the ‘isolated fault model’) suggests fault growth occurs via a synchronous increase in fault length and displacement. The constant length model suggests that faults establish near-linear lengths early in their slip history, after which they grow mainly by accumulation of displacement. It has been suggested that there is a bias in favor of the propagating model despite evidence for the constant length fault model (Rotevatn et al., 2019). Furthermore, Rotevatn et al. (2019) found evidence that most faults are characterized by two stages, where the first is defined by fault lengthening (20-30% of fault lifespan) and the second by displacement accrual (70-80% of fault lifespan).

Determining lateral and vertical variations in fault displacement (throw) can be used to assess interaction styles, timing, and fault growth trends (Peacock & Sanderson, 1991). In the case of CO_2 storage sites, analyzing fault throw is an effective way to assess the position of juxtaposed stratigraphic units and the presence of membrane seals, which impact the sealing or non-sealing potential of faults. While faults are observed as single surfaces in seismic data, they are heterogenous zones of deformed host rock that may not be imaged because of the limits of seismic resolution: This can be challenging in terms of determining the structural complexities of the fault zone, however, it is important to assess this as they may influence across-fault fluid migration (subsection 3.1.2.2).

Faults can be characterized as elliptical-shaped structures. It is widely recognized that fault displacement varies within the fault surface (Barnett et al., 1987; Walsh & Watterson, 1987). The displacement of a fault is at its maximum near the center of the fault surface and usually decreases to zero at the fault tips. In rifts, zones of isolated faults in proximity to each other can begin to interact through fault growth. Three stages of growth and linkage can be identified (Peacock & Sanderson, 1991): Initially, isolated faults (stage 1 in Figure 3.2A) can propagate toward each other and eventually the fault tips interact making a soft-linked structure called a relay ramp. The fault segments may develop with no obvious linkage (stage 2 in Figure 3.2A) or hard link by breaching the relay ramp (stage 3 in Figure 3.2A).

Throw vs. length profiles are a way to visualize the lateral variations in fault throw by plotting the fault throw along-strike with the traced length of the fault. Isolated faults will typically show a close to symmetrical throw vs. length profile with maximum throw at the center of the profile, decreasing to zero at the fault tips (stage 1 in Figure 3.2B). Soft-linked segments of faults may display steep throw gradients near the fault tips in the zone where faults interact, indicating a relay ramp structure (stage 2 in Figure 3.2B). Further, hard-linked segments can be identified by throw minima in the throw vs. length profile (stage 3 in Figure 3.2B).

Maximum throw vs. length plots are often used to assess fault growth trends by plotting the maximum throw against the maximum trace length of a fault. Figure 3.2C shows a maximum throw vs. length plot where two faults are used as examples through the three stages of fault linkage. The first stage represents isolated faults, the second stage individual segments of faults, and the third stage represents interacting faults, either soft-linked or hard-linked. Note that fault lengths abruptly jump at stage 2, where the fault segments interact, and then grow in mainly throw as they get hard linked (stage 3).

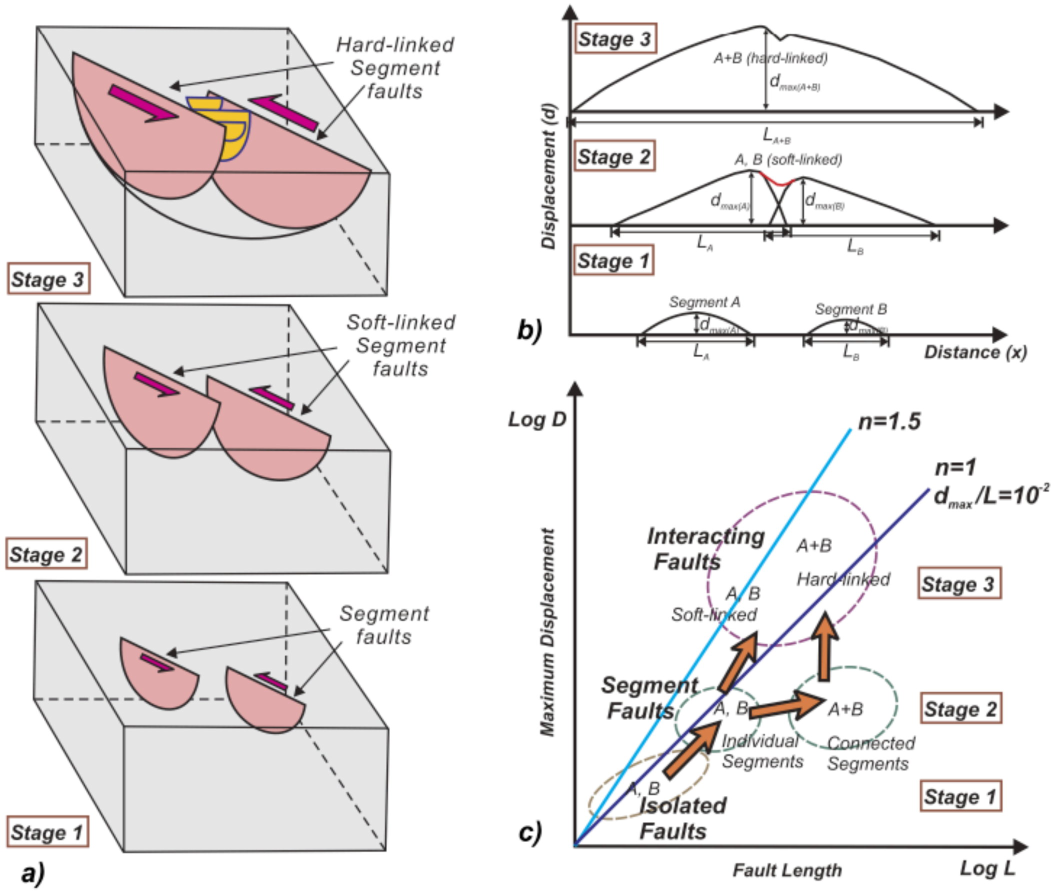

Figure 3.2. Fault segmentation and linkage (Kim & Sanderson, 2005). A) Faults evolve from isolated faults to interacting faults through three stages. B) Throw vs. length profile for the three stages. C) Maximum throw vs. length plot showing the evolution of linkage between to initially isolated faults.

3.1.2 Fault seal types

The sealing or non-sealing behavior of faults within hydrocarbon reservoirs or CO_2 storage sites is an essential aspect in assessing the overall structural integrity of a fault-bounded trap. Faults can behave as conduits, barriers, or combined barrier-conduit structures for hydrocarbon migration (Pei et al., 2015). Faults may also act as “baffles” due to spatial variations in permeability along the fault, which can result in abrupt changes in reservoir pressure during gas injection and/or depletion (Yielding et al., 1999). This is also applicable for the injection and storage of CO_2, and in order to assess if a proposed CO_2-storage is geologically stable over sufficient time periods, fault seal analysis is essential (Bretan et al., 2011). Two types of seals have been recognized in siliciclastic rocks, which are fault rock seals (membrane seals) and juxtaposition seals (Pei et al., 2015). In the following subsections, the theory behind these seals is provided.

3.1.2.1 Juxtaposition seals

When a sequence of sedimentary beds is cut by faulting, three main movements occur, or a combination of them occur: The hanging-wall moves upward for normal faults, downward for thrust faults, and laterally for strike-slip faults, relative to the footwall. The relative movement between the hanging wall and footwall results in the juxtaposition between rocks with different petrophysical properties (e.g. different porosities, permeabilities, and capillary entry pressures) at each side of the fault-plane (Pei et al., 2015). For example, a juxtaposition seal occurs when a bed of mudstone is juxtaposed against a bed of sandstone, due to the significant permeability gradient between the different lithologies (Pei et al., 2015). It is important to note that several factors are known to influence the fault seal capacity, not only the type of lithology. For example, the architecture of fault zones can be highly variable, both along the damage zones around individual faults and between faults (Færseth et al., 2007). In an attempt to quantify the risk associated with seals for fault-bounded prospects, Færseth et al. (2007), suggest that juxtaposition seals, containing a single fault plane, have the highest probability of sealing (70 – 100%). Self-juxtaposed units, with a clean sandstone, have a lower probability (0 – 30%), and finally, membrane seals, with clay-shale smear, have an intermediate probability (50 – 70%). Membrane seals will be discussed in subsection 3.1.2.2. Commonly, two methods have been used when addressing juxtaposition seals in seismic data: The Allan technique by Allan (1989), and the triangle diagram by Knipe (1997).

In 1989, Allan introduced a model to relate faults to hydrocarbon migration and entrapment. The model states that the influence of faults on hydrocarbon migration and entrapment is determined by the lithology of juxtaposed stratigraphic units on different sides of the fault and the fault throws between the hanging wall and the footwall cut-offs (Allan, 1989). The Allan technique produces a 2D model of the 3D fault plane in seismic (Figure 2). The model displays the relationship of the lithological cut-off lines across the fault plane for a given stage. The Allan technique has been used in several studies for assessing across-fault seals in a CO_2 storage context (Bretan et al., 2011; Karolyte et al., 2020; Mulrooney et al., 2020).

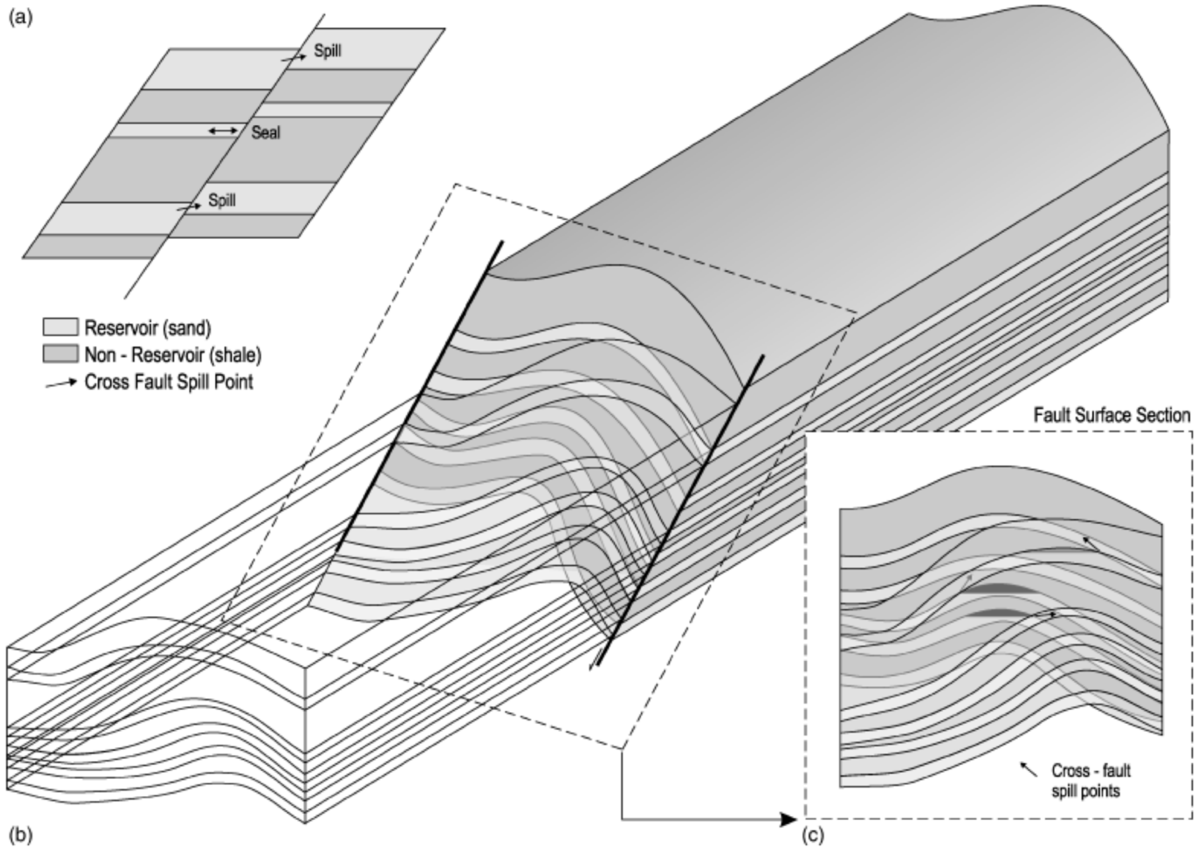

Figure 3.3. The basis of an Allan diagram. A) The displacement of a fault can provide a seal by juxtaposing impermeable units (shale) against permeable units (sandstone). B) The fault in 3D, displaying the intersections of the stratigraphic units in the hanging wall and footwall. C) Allan diagram showing the fault plane in 2D with footwall and hanging wall cut-offs. Traps and spill points can be assessed from the juxtaposition of the stratigraphic units. Figure from (Clarke et al., 2005)

Knipe (1997) presented an effective technique to assess fault juxtaposition, named the triangle juxtaposition diagram. It can be used to quickly judge what types of fault seals can be formed based on the stratigraphic juxtapositions between the hanging wall and footwall. The triangle juxtaposition diagrams are based on the interaction of rock lithologies, and the fault throw to control fault seal types and type of juxtaposition. The diagrams can also be used to contour host rock characteristics such as permeability, porosity, and percentage of phyllosilicates (Knipe, 1997). The advantage of using the triangle diagrams compared to Allan diagrams is that they can be constructed without detailed 3D-mapping of stratigraphic horizons and fault planes in seismic.

3.1.2.2 Fault rock seals, processes, and algorithms

Different faulted rocks are created when different types of host rocks are entrained into the fault zone during faulting (Fisher & Knipe, 1998; Knipe, 1997; Pei et al., 2015). The composition of the sediments in the host rock and the depth at the time of faulting determine the deformation mechanisms, microstructures, and petrophysical properties of the fault rocks (Figure 3.5).

Several fault processes have been observed where the fault itself becomes sealing due to reduced permeability: disaggregation, cataclasis, cementation, and clay smearing (Fisher & Knipe, 1998; Fossen et al., 2007). Disaggregation zones and cataclasites are the main type of fault rock in host rocks (clean sandstones) that are low in clay and phyllosilicate content (>15%) (Ottesen Ellevset et al., 1998). Disaggregation zones form by faulting at shallow depths (<1 km) by disaggregation and mixing of grains by means of grain rolling and sliding (Fisher & Knipe, 1998; Pei et al., 2015). The permeability of fault rocks formed by disaggregation and mixing varies, depending on the clay and phyllosilicate content of the host rocks. For example, in clean sandstones, the grain size and sorting of the fault rock do not change considerably during disaggregation, resulting in no significant change in permeability and porosity (Pei et al., 2015). Although Fisher & Knipe (2001) observed a permeability reduction in phyllosilicate bearing disaggregation zones by one order of magnitude, these fault rocks have a limited effect on the permeability of sandstone reservoirs as the permeability contrast is relatively low (Fossen et al., 2007). Cataclasites form in higher confining pressures. As cataclasites are made in host rocks that have a low clay and phyllosilicate content (<15%) at the time of deformation, the main mechanisms of porosity and permeability reduction are grain size reduction by fracturing and frictional grain rolling (Fisher & Knipe, 2001). The permeability of cataclasites varies over a large range, as it depends on the lithification state of the host rock (Knipe, 1997). Cement seals happen in fault zones where dissolution-reprecipitation processes of minerals occur in the fault plane (Ottesen Ellevset et al., 1998). In most cases, the cementation is not extensive enough to make the fault adequately sealing (Ottesen Ellevset et al., 1998).

Fault tocks with clay and phyllosilicate contents of >40% are defined as clay smears. Clay smearing occurs in host rocks with >40% clay and phyllosilicate content during faulting (Jolley et al., 2007; Ottesen Ellevset et al., 1998). During faulting in clay- and phyllosilicate-rich host rocks, continuous, low permeability clay material zone along the fault plane can be produced.

The most important factors that control the continuity of the clay smear are the content and distribution of the clay and phyllosilicates, the fault throw (Bouvier et al., 1989; Lindsay et al., 1993; Yielding et al., 1997), and the lithification of the host rocks (Egholm et al., 2008). An intermediate fault rock, phyllosilicate-framework fault rocks (PFFRs), can develop in host rocks with a 15 – 40% clay and phyllosilicate content (Fisher & Knipe, 1998). As continuous clay and phyllosilicate smears have very low porosity and permeability, these fault rocks act as very effective fluid flow barriers (Pei et al., 2015), and therefore, they are considered to have a sealing potential within CO_2 storage sites (Bretan et al., 2011).

The largest controlling factor in the development of fault rock seals is thus the host rock-properties, especially the clay or phyllosilicate content, the porosity, and the permeability characteristics (Knipe, 1997; Pei et al., 2015). For example, if reservoir rocks self-juxtapose or juxtapose against other high-permeable rocks, it has been observed that the fault zone can provide a membrane seal where the capillary threshold pressure is significantly larger than the reservoir rock (Færseth et al., 2007; Fisher & Knipe, 2001; Yielding et al., 1997). Even though membrane seals have lower probabilities of sealing compared to juxtaposition seals (Færseth et al., 2007), they have been shown to be sealing in hydrocarbon settings (Færseth et al., 2007; Yielding et al., 1997).

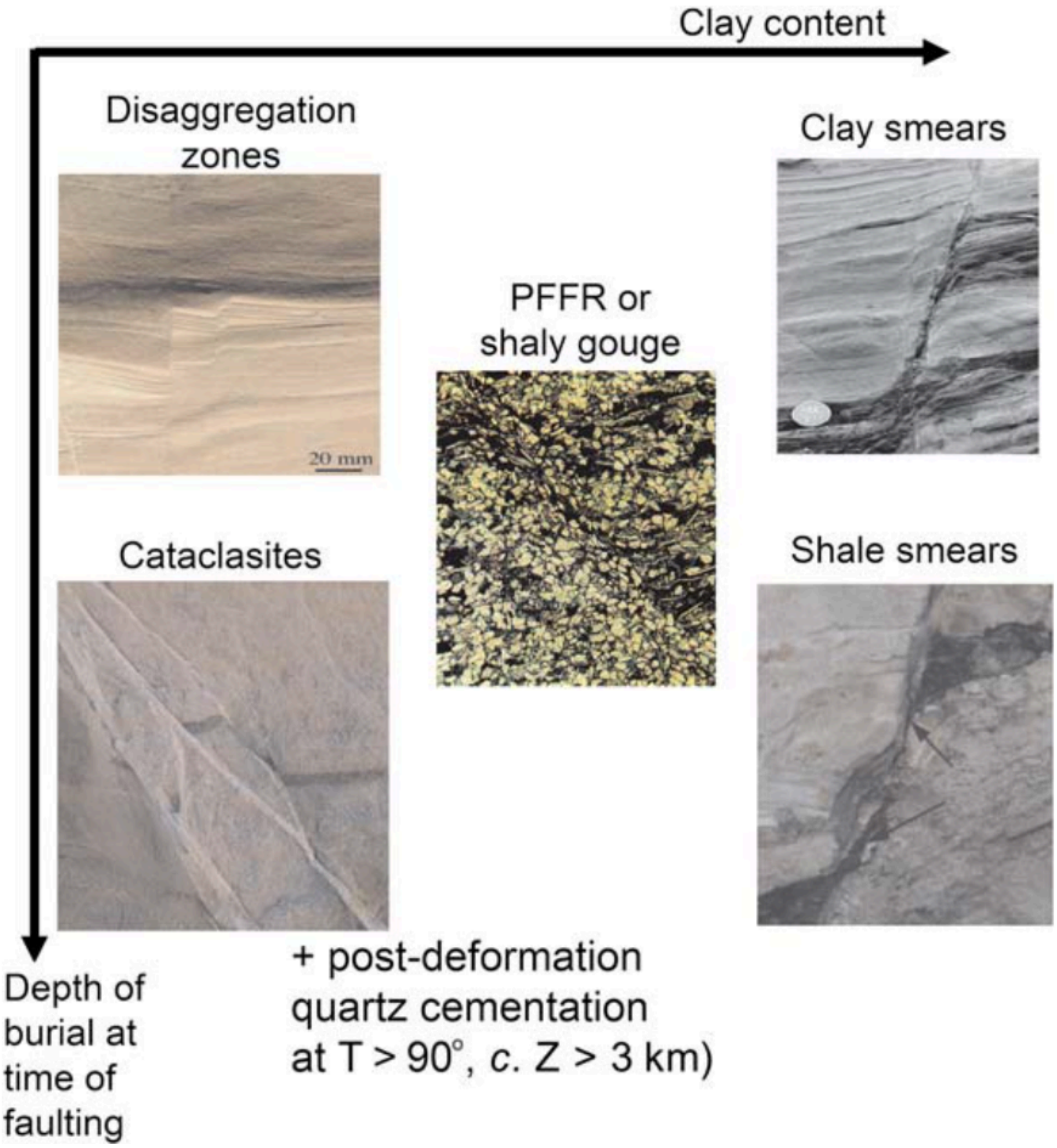

Figure 3.4. Schematic plot illustrating the main fault rock types that are generated in siliciclastic rocks. The axes represent two of the main controls to make a particular fault rock (depth of burial at the time of faulting and clay content). Figure from Yielding et al. (2010).

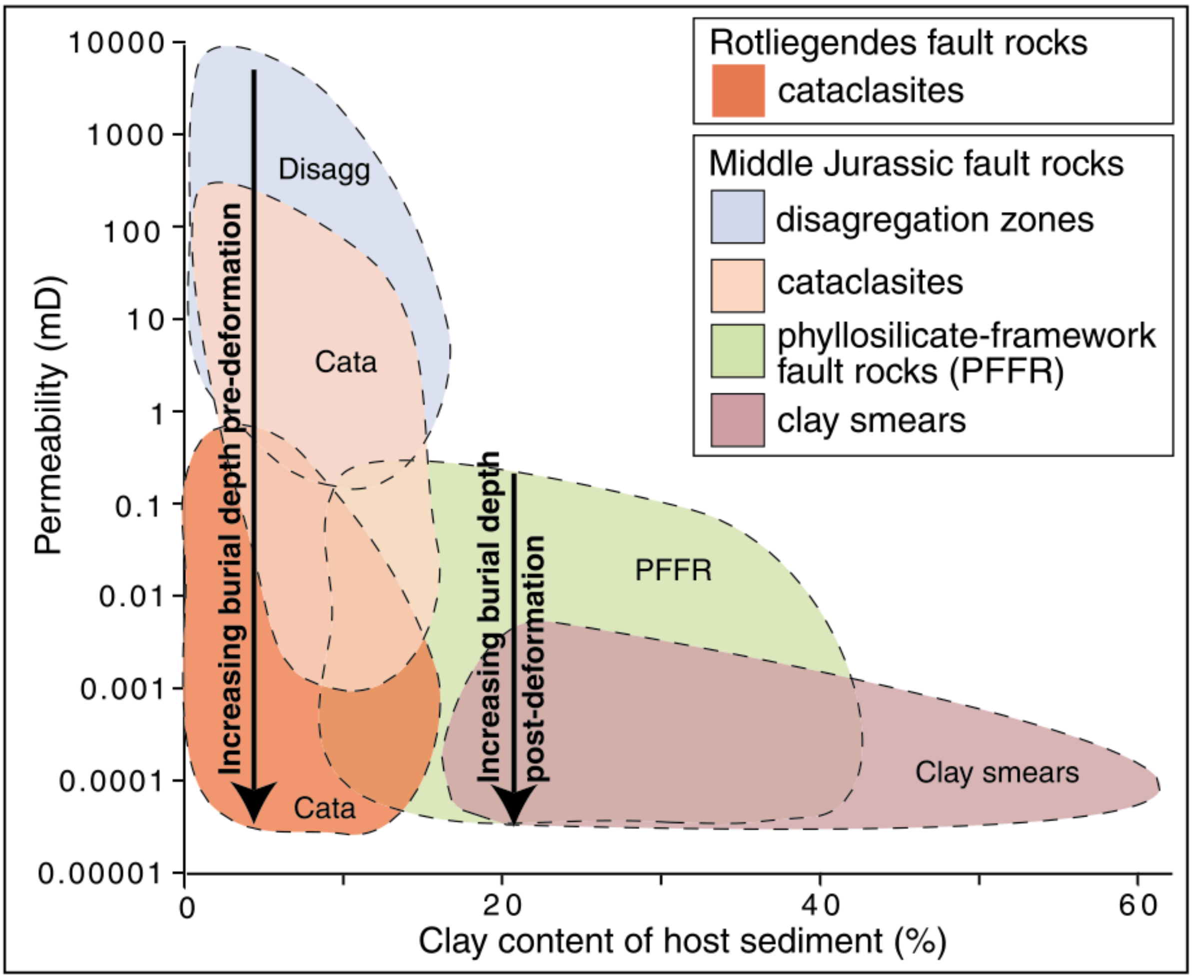

Figure 3.5. Summary of the fault rock permeability from the North Sea and Norwegian Continental shelf (Fisher & Knipe, 2001). The permeability of different fault rocks is plotted against the clay content of the host rocks. Depending on the permeability, the clay content of the host rock, and the burial depth pre- and post-faulting, different kinds of fault rocks develop: Disaggregation zones, cataclasites, phyllosilicate-framework fault rocks, and clay smears. Lower permeabilities are favorable for sealing.

When a fluid is lighter than the pore-filling brine, such as CO_2, is introduced into a reservoir rock in the subsurface, it will always migrate upwards due to the buoyancy effect. This migration will take place until the fluid reaches a flow barrier such as a fault or a caprock and the buoyancy of the CO_2 creates a difference in pressure (ΔP) at the interface of the fault or the caprock-reservoir. ΔP is proportional to the CO_2 column height (h) and the difference in mass density between the pore-filling brine (P_w) and CO_2 (P_{CO2}) (Miocic et al., 2019):

$$\Delta P = (P_w - P_{CO2})gh$$

Where g is the gravitational constant. Further, membrane seals are controlled by the fluid buoyancy pressure of the CO_2 and the threshold capillary pressure (P_c). The threshold capillary pressure is expressed as:

$$P_c = \frac{2IFT \ \cdot \cos(\theta)}{r}$$

Where *IFT* is the interfacial tension between the CO_2 and the brine, θ is the wettability of the rock mineral surface (contact angle) with respect to the CO_2, and r is the pore-throat size. Membrane seals fail when the buoyancy pressure exceeds the threshold capillary pressure, and leakage across the fault can occur. Thus, the ability of a membrane seal to retain specific column heights depends on the fault rock composition which controls the pore-throat size and the wettability parameters:

$$h = \frac{2IFTcos(\theta)}{r} \cdot \frac{1}{(P_w - P_{co2})g}$$

As seen in the previous equation, the maximum column height a membrane seal can confine is dependent on the host-rock properties, such as the wettability parameters (*IFT, θ*), the pore-throat size (r), and the densities of the pore-filling brine (Pw) and the CO_2 (P_{CO2}). In contrast to hydrocarbons, there are uncertainties associated with the wettability parameters for CO_2, which can influence the column heights of CO_2 a membrane seal can hold (Karolyte et al., 2020; Miocic et al., 2019). For example, contrary to hydrocarbon systems, higher phyllosilicate entrainment into the fault rock may lessen the amount of CO_2 that can be retained due to different wettability properties (Miocic et al., 2019).

Several algorithms have been developed to predict the clay content within fault rocks. These algorithms include the clay smear potential (CSP) (Bouvier et al., 1989) , the shale smear factor (SSF) (Lindsay et al., 1993), and the shale gouge ratio (SGR) (Freeman et al., 1998; Yielding et al., 1997) (Figure 5).

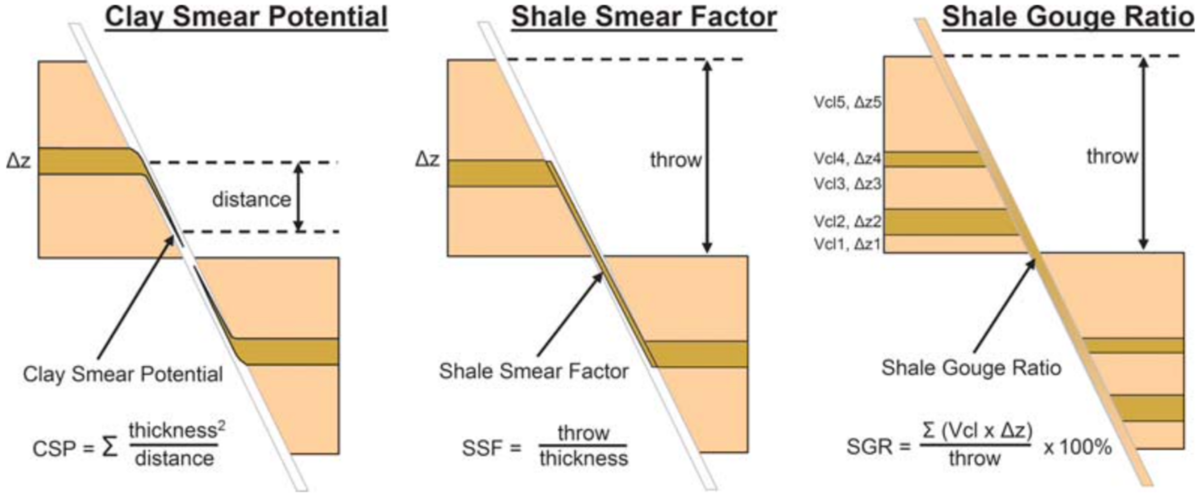

Figure 3.6. Schematic diagrams of the main fault-seal algorithms (Yielding et al., 2010). From left to right: Clay smear potential, shale smear factor, and shale gouge ratio.

The CSP algorithm represents the relative amount of clay that has been smeared from individual shale units at a certain point along a fault plane (Bouvier et al., 1989). The algorithm is given by the square of source bed thickness divided by smear distance. CSP increases with shale source bed thickness, the number of source beds displaced at a given point along a fault plane and decreases with increased fault throw.

The SSF algorithm predicts the likelihood of shale smear continuity, given by fault throw divided by source bed thickness. Therefore, low SSF values correspond to a higher likelihood of continuous smear. Lindsey et. al (1993) based their algorithm on observations of abrasion smears in a lithified sequence.

The SGR algorithm predicts the likelihood of clay entrainment in the fault gouge zone and gives the percentage of shale or clay in the slipped interval (Yielding et al., 1997). In this algorithm, it is assumed that sand and shale material in the wall rock are integrated into the fault gouge in the same proportions, as they occur in the slipped interval, hence SGR is considered to be a predictor of the fault rock composition (Bretan et al., 2011). The amount of shale material in the wall rock, the volumetric clay fraction (Vclay), is often derived from well data such as gamma-ray and neutron-density logs. A high SGR value reflects more phyllosilicates and clay in the fault zone (e.g. clay smear) and therefore predicts higher capillary threshold pressures and lower permeability (Bretan et al., 2011).

An important aspect of using fault seal algorithms (CSP, SSF, and SGR) to determine the presence of clay smear, is that the calculated values need to be calibrated to provide meaningful estimates (Yielding et al., 2010). For example, Yielding et al. (2010) proposes that SSF values of >4-5 represent a high chance of a continuous smear in the fault zone, and therefore a seal at the fault, while CSP values of >30 represent a sealing value (Jev et al., 1993). In many basins and in particular the Brent Province (Yielding, 2002), it is observed that SGR values of >15–20% correspond to faults that are sealing to hydrocarbons. From a study by Fossen et al. (2007), they found that in the faulted Jurassic reservoirs of the northern North Sea, SGR values of <15–20% correspond to fault rocks dominated by disaggregation zones, with negligible sealing capacity.

Two fundamentally different approaches have been favored to predict the capacity of fault seals, that is, the 'deterministic' and 'empirical' approach (Yielding et al., 2010). The deterministic approach is based on capillary threshold pressure and clay content measurements from cored wells nearby the fault. It is necessary to perform an SGR analysis of the fault to extrapolate the measurements to the target fault in the subsurface (Yielding et al., 2010). The empirical approach involves using SGR analysis on known sealing faults compared with measured pressure differences and column heights trapped by the fault (Figure 6). Then, the resulting SGR and column height relationship is used on adjacent prospects to predict the fault seal capacity (Yielding et al., 2010). The plot in Figure 6 shows an empirical approach and summarizes when faults are leaking and sealing. Note the seal-failure envelope for shallow depths (<3 km, blue) exhibits no seal at SGR values of <15 – 20%, corresponding to the sealing threshold SGR values in the Brent Province.

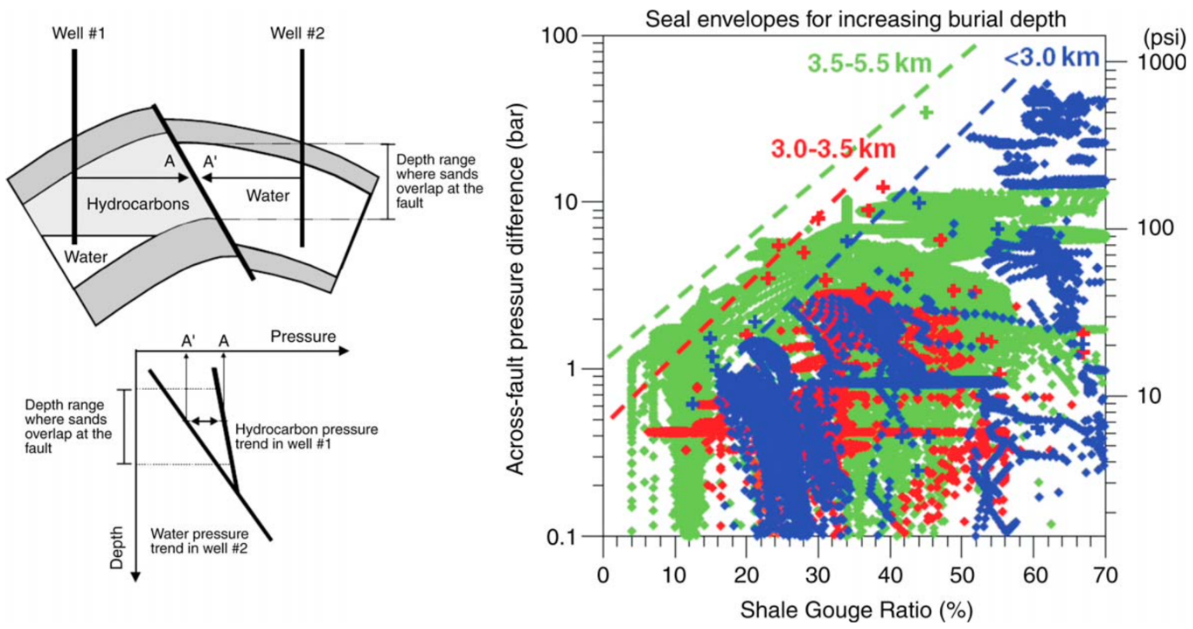

Figure 3.7. The empirical approach to fault seal calibration (Bretan et al., 2003; Yielding et al., 2010). Figure to the left: Data from adjacent wells are used to assess across-fault pressure in the fault where reservoir rocks self-juxtapose. Figure to the right: A plot showing a global compilation of across-fault pressure differences plotted against SGR, at the same point on the fault surface. The data are compiled from several faults in nine different extensional basins. The points are color-coded by maximum burial depth, blue <3 km, red 3 – 3.5 km, green >3.5 km. The dashed lines are suggested fault-seal-failure envelopes for different depths, that is, maximum across-fault pressure that can be supported at a specific SGR value, for maximum burial depths. Figure from Yielding et al. (2010).

3.2 Data

This section outlines the data used in this study. The fundament of this study is the interpretation of 3D seismic data (section 3.2.1). In addition to 3D seismic data, 2D seismic data (section 3.2.2) and well data (section 3.2.3) were used. Together, these data have been used to create a high-resolution 3D geomodel of the Gamma prospect and the study area and do fault analysis and modeling.

3.2.1 3D seismic data

A typical marine 3D seismic survey is carried out by emitting sound pulses into the subsurface in closely spaced parallel lines. The shooting direction, or the boat track, is called the inline direction, whereas the perpendicular direction to the inlines is called the crossline direction.

3D Seismic reflection data provides a three-dimensional image of the subsurface by measuring the time (ms) it takes for a P-wave to propagate down to an interface and reflect up to a receiver, measured in two-way-time (TWT). These interfaces are displayed as reflectors in the seismic image and represent where the acoustic properties of the rocks change. Acoustic impedance (AI) is the product of the density (ρ) and the velocity (v) of a rock layer.

A subset of the 3D seismic survey CGG NVG was utilized in this thesis. The 3D seismic data was acquired in 2016 and is pre-stack depth migrated (P-SDM). For this study, the CGG NVG survey was cropped to cover the study area, named herein NVG-HORDA-TAMPE. NVG-HORDA-TAMPE partially covers quadrants 31, 32, 35, and 36, covering a 2.5 km^2 area in the northern Horda Platform and the Smeaheia Fault Block (Figure 3.8). The Troll East field is in the western part of the cropped survey, whereas the Gamma license is in the southern part (Figure 3.8). The NVG-HORDA-TAMPE seismic volume images 20 km below sea level. It is characterized by an SEG normal polarity (an increase in AI is displayed as a reflection peak). Inline and crossline spacings are 18.75 m and 12.50 m, respectively. Inlines are oriented north-south, and crosslines are oriented east-west, with crosslines approximately perpendicular to thick-skinned faults (e.g., Øygarden Fault Complex, Vette Fault Zone, and Tusse Fault Zone (TFZ)). The survey was provided by CGG in both TWT and TVD. For seismic interpretations in this study, the TVD cube was utilized because it images structural features in the subsurface more accurately than in time-domain, making the assessments of fault geometries such as throw more accurate (Lyon et al., 2004). In addition, calculation of bulk volumes of structural closures (section 3.3.6) must be done in depth-domain. The vertical resolution is roughly 5 – 10 m within the Jurassic intervals (Osmond et al., 2021).

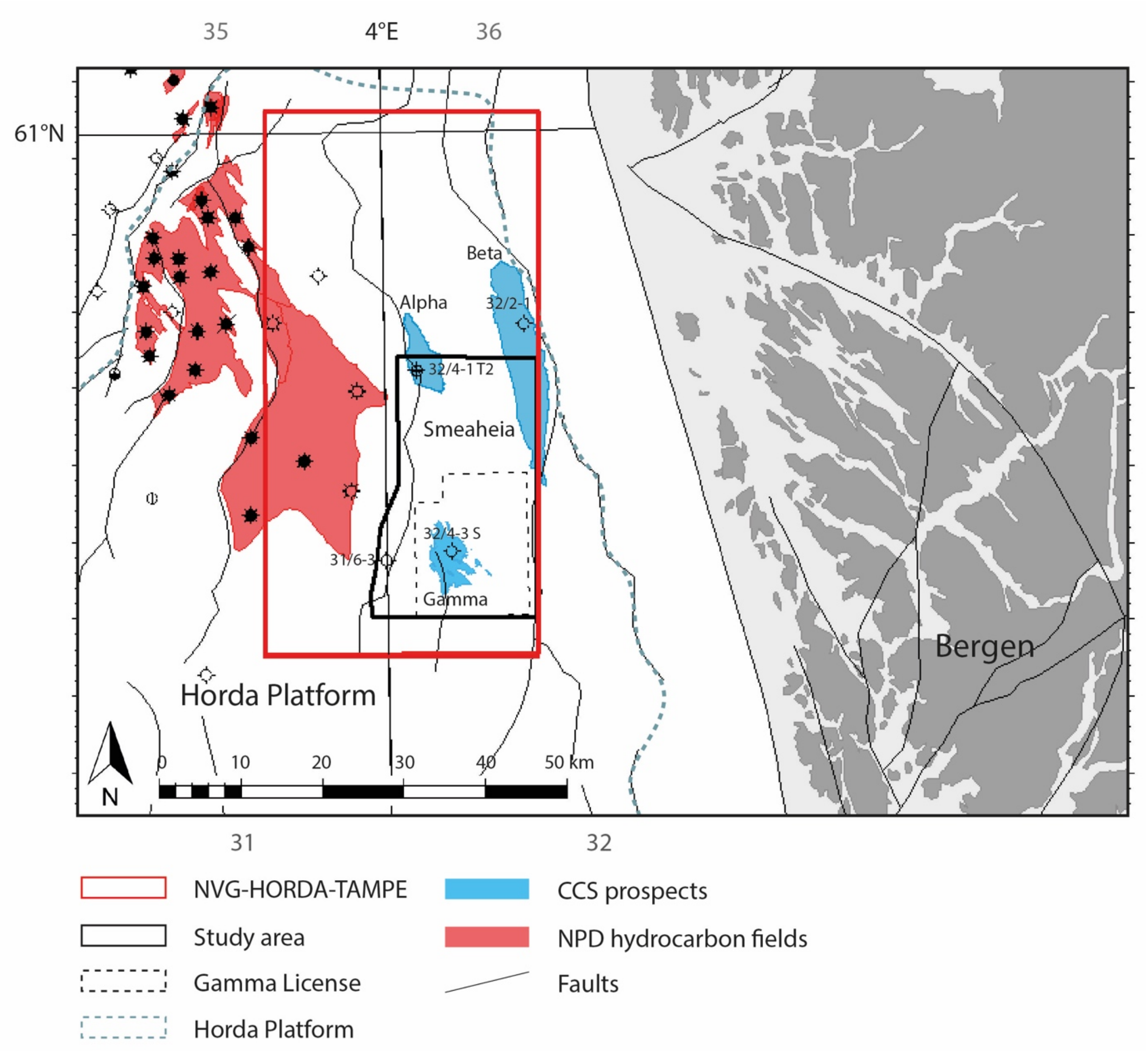

Figure 3.8. Map illustrating the subset NVG-HORDA-TAMPE of the 3D seismic survey CGG NVG, outlines of the study area, Gamma license, and the Gamma prospect. Note that not all wells are displayed in the map.

3.2.2 2D seismic data

Whereas 3D seismic data provides a three-dimensional image of the subsurface, 2D seismic data displays an image of the subsurface along lines. In this study, 2D seismic data covered larger areas than the NVG-HORDA-TAMPE survey and was therefore used to provide a regional context for the structural and stratigraphical tendencies outside this seismic volume. The seismic survey used for this purpose is SG8043-REP91, a dataset covering the entire Horda Platform, provided in TWT by the NPD Diskos repository. The survey was acquired in 1980 and is characterized by an SEG normal polarity, imaging 7000 TWT below sea level. The survey contains 65 lines with a spacing of 4 – 10 km. Figure 2 shows one of these lines, SG8043-104E.

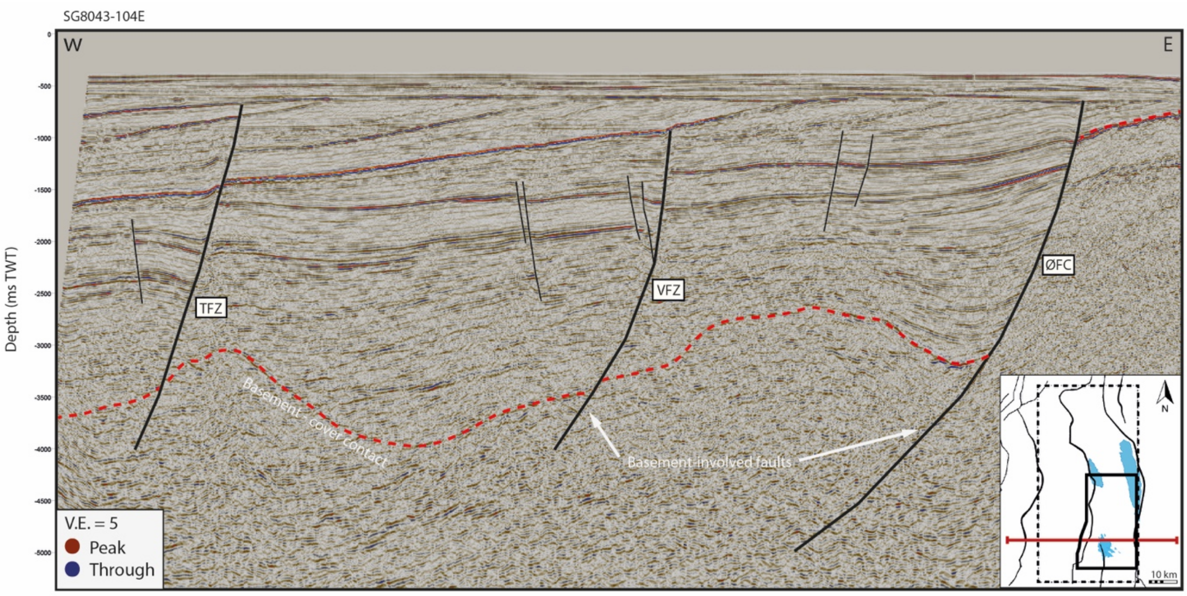

Figure 3.9. A seismic 2D line from the SG8043-REP91 survey displaying a profile through the Gamma prospect and the study area. The basement contact and the basement-involved Øygarden Fault Complex (ØFC), Vette (VFZ), and Tusse (TFZ) Fault Zones are shown.

3.2.3 Well data

Ninety-nine wells were available for analysis in this study. Three wells are present within the study area, 31/6-3, 32/4-1 T2, and 32/4-3 (Figure 3.8). Well 32/4-3 S is the only one within the storage prospect, located in the footwall of the VFZ. Well 31/6-3 is approximately 8.5 km to the east from 32/4-3 S, in the hanging wall of the VFZ. Well 32/4-1 T2 is within the Alpha prospect, approximately 24 km to the north from 32/4-3 S in the footwall of the VFZ. An additional well, 32/2-1, just outside the study area, was used for analysis. 32/2-1 is within the Beta prospect, 31 km northwest from 32/4-3 S (Figure 3.8). Table 3.1 summarizes the wells and the well tops used in this study. Figure 3.10 shows correlation of the four wells with gamma-ray logs and well tops to show candidates for horizon interpretation.

As mentioned in chapter 1, the exploration target for drilling well 32/4-3 S was to detect petroleum in the Late Jurassic reservoir rocks (Sognefjord Formation) and evaluate the sealing capacity of the Draupne Formation and the storage potential for CO_2 in the reservoir rocks. The well was found to be dry and confirmed 155 meters of massive sandstones with good to very good reservoir quality in the Sognefjord Formation (NPD, 2019). In addition, the well penetrated Early Jurassic to Late Triassic sandstones: 60 meters in the Fensfjord Formation, 35 meters in the Krossfjord Formation, 40 meters in the Ness Formation, 45 meters in the Johansen Formation, 7 meters in the Statfjord Group, and 95 meters in the Lunde Formation. The reservoir quality of these sandstones alternates between moderate to very good (NPD, 2019). Thus, the Sognefjord Formation and the lower Jurassic sandstones makes candidates for CO_2 containment, which will be discussed further in section 4.1.1.

Table 3.1. Table showing the depth of the well tops for the wells in the study area. Well tops are acquired from the NPD factpages.

Well name **Well top (m Measured Depth)**	**32/4-3 S**	**31/6-3**	**32/4-1 T2**	**32/2-1**
Cromer Knoll Gp	744	998	954	620
Sola Fm	-	1058	-	620
Draupne Fm	1101	1370	1108	823
Sognefjord Fm	1248	1511	1237	902
Drake Fm	1669	1827	1680	-
Johansen Fm	1746	2042	1785	1187
Statfjord Gp	1823	2143	1816	1228

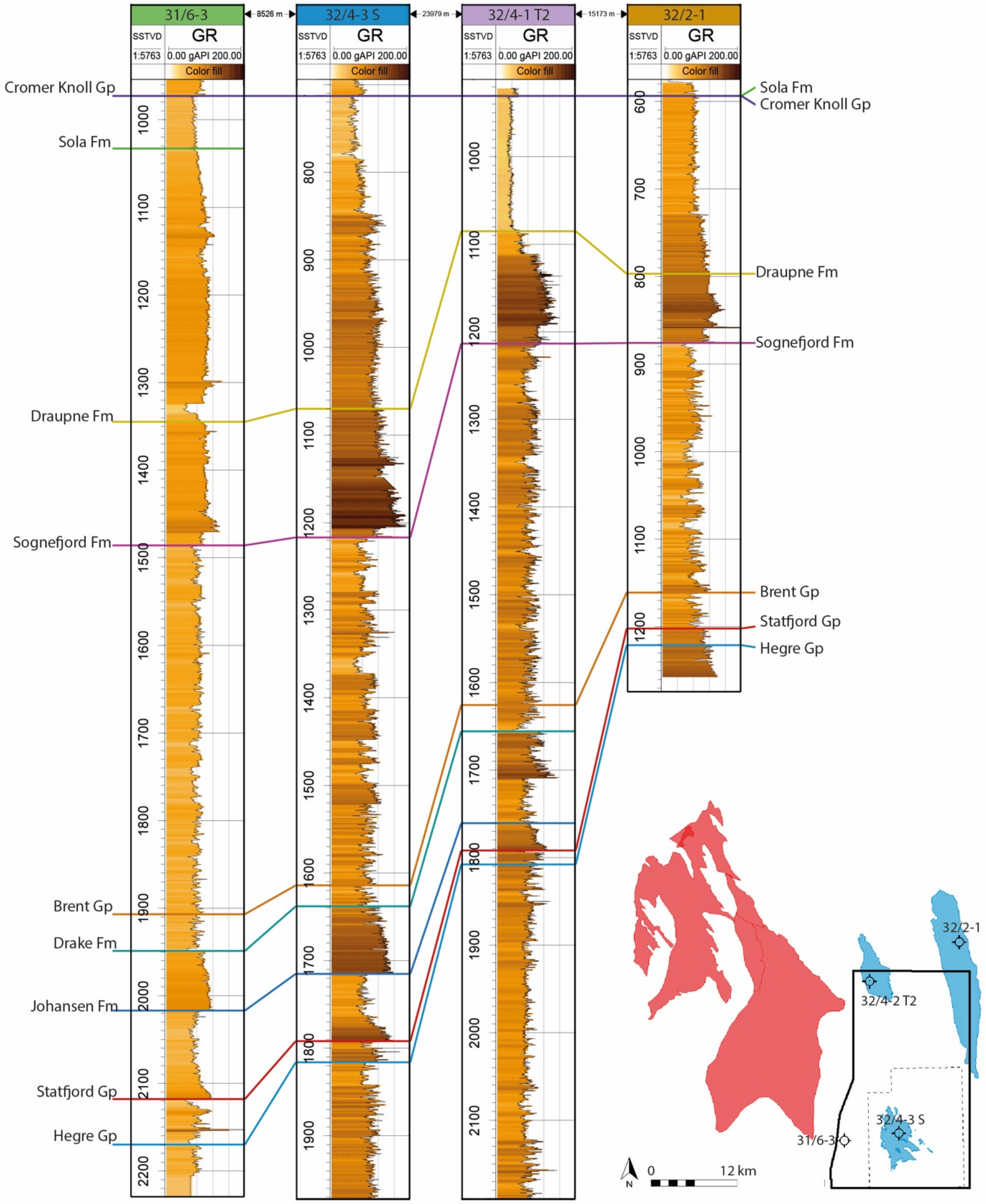

Figure 3.10. Well correlations for wells 31/6-3, 32/4-3 S, 32/4-1 T2, and 32/2-1, correlating gamma-ray logs and well tops across the study area. The well correlations are flattened on Top Cromer Knoll Group and display the thickness variations of the formations and groups within the study area. CCS prospects are shaded in blue and hydrocarbon fields are shaded in red. Well tops are extracted from NPD factpages.

3.2.4 Data limitations

One of the most important questions that drive basin research is how deformation is accommodated because it is highly heterogeneously distributed spatially and over time and over a wide range of scales (Gauthier & Lake, 1993). Large-scale subsurface faulting is typically identified by interpretation of 2D or 3D seismic data (Gauthier & Lake, 1993; Yielding et al., 1996). Faulting at a medium scale, i.e., displacements between approximately 30 m and a few decimeters, may rarely be recognized in seismic data due to limitations of the seismic resolution (Lohr et al., 2008; Yielding et al., 1996). However, faulting at a medium scale is an extensive factor in reservoirs, for example, medium displacements along faults can change the juxtaposition between units of sandstone or shale, which can lead to clay smearing on fault surfaces, which may result in a reduction of fluid flow (Stewart, 2001). Furthermore, fracture networks may act as conduits for fluids or even as reservoirs (Cosgrove, 2001). These examples show that faulting and fracturing below the limit of seismic resolution (herein referred to as subseismic) can control fluid migration and therefore has a significant role in hydrocarbon reservoirs (Lohr et al., 2008) and also in CO_2 storage. Therefore, when creating a structural geomodel and performing structural analysis, considering the resolution of the seismic data is important.

The vertical resolution of seismic data is the minimum distance, both vertically and horizontally, between two, say, different stratigraphic units that are controlled by the wavelength of the seismic signal. The wavelength can be determined by measuring the distance between two peaks within the seismic image, then dividing the seismic velocity by the dominant frequency of the seismic data. The vertical resolution of seismic data has a range between 1/4 and 1/8 of the dominant wavelength of the seismic pulse. Osmond et al. (2012) estimates that the vertical resolution for the CGG NVG survey is roughly 5 – 10 m within the Jurassic intervals, which is the depth of interest in this thesis. Therefore, subseismic structures and displacements close to 5 – 10 m will not be imaged in the CGG NVG survey.

3.3 Methods

A high-resolution geomodel of the study area and the Gamma closure was interpreted from the NVG-HORDA-TAMPE 3D seismic survey. This chapter outlines the workflow and methods used in this study to create the geomodel. As a reminder, the main objectives in this study are to: i) generate a high-resolution 3D geomodel of the Gamma structure from seismic interpretation, ii) to discern if trapping structures and continuous caprock are present in the Jurassic intervals, iii) to discern the volumetric capacity of the proposed storage formation, iv), and v), discuss possible CO_2 injection points and migration pathways. The workflow in this study comprises six main stages: Literature study, software training, seismic and well log interpretation (section 3.3.1), fault modeling and analysis (section 3.3.2), volumetric analysis and storage capacity assessment (section 3.3.3), and finally analysis of migration pathways (section 3.3.4). The software used for seismic interpretations and volume calculations was Petrel E&P Software Platform (v. 2021.1). The software used for fault modeling and analysis was performed in Petroleum Experts (PETEX) Move suite (v. 2020.1).

3.3.1 Horizon and lithological interpretation

The first step in the method is to interpret horizons of interest within the seismic volume and assess lithologies with associated horizons. Before performing horizon interpretations, wellbore data is used to correlate well tops and logs to the reflectors of interest in the seismic data. In this study, four wells were used to assess the seismic horizon picks in the study area: 32/4-3 S, 32/4-1 T2, 32/2-1, and 31/6-3 (Figure 3.10).

Furthermore, to aid horizon interpretations and determining lithology, simple seismic facies analyses were conducted. A seismic facies unit can be defined as a sedimentary unit of which the seismic signatures differ from those of the adjacent units (Xu & Haq, 2022). In this study, seismic parameters such as external form, internal configuration, amplitude, and continuity are determined for horizons and formations of interest, as these parameters are most commonly used in determining seismic lithofacies (Xu & Haq, 2022). The external form of a seismic facies' unit refers to the shape of the unit of interest and are divided roughly into seven different forms, i.e., sheet, wedge, bank, lens, mound, fan, and concave (Xu & Haq, 2022). In this study, seismic profiles (Figure 3.11, Figure 4.3 & Figure 4.4) and observation of depth-structure maps

(Figure 3.13D) in 3D were used to determine the external form of units of interest (Table 4.1). Internal configuration refers to the permutation and combination mode of reflection events within a seismic facies unit of interest and it reflects the stratigraphic structure of the unit (Xu & Haq, 2022). In this study, the internal configuration between two horizon picks in a seismic profile, for example, the Top Draupne Formation and the top Sognefjord Formation (Figure 3.11) were determined (Table 4.1). The amplitude of a seismic reflection wave mainly reflects the contrast in acoustic impedance at the interface of a different lithology and depends on the porosity, density, pore-filling media, the thickness of a unit, and the spacing between two thin layers (Xu & Haq, 2022). The reflection amplitudes of conventional seismic sections are relative and are usually separated into three levels, i.e., high, medium, and small. In this study, the amplitudes are distinguished into large, medium, and small (Table 4.1). Continuity of a seismic event refers to how continuous a reflection appears in the seismic image and it reflects the stability of the distribution of a unit in the horizontal direction (Roksandic, 1978). In this study, reflections were divided into continuous, semi-continuous, and discontinuous (Table 4.1).

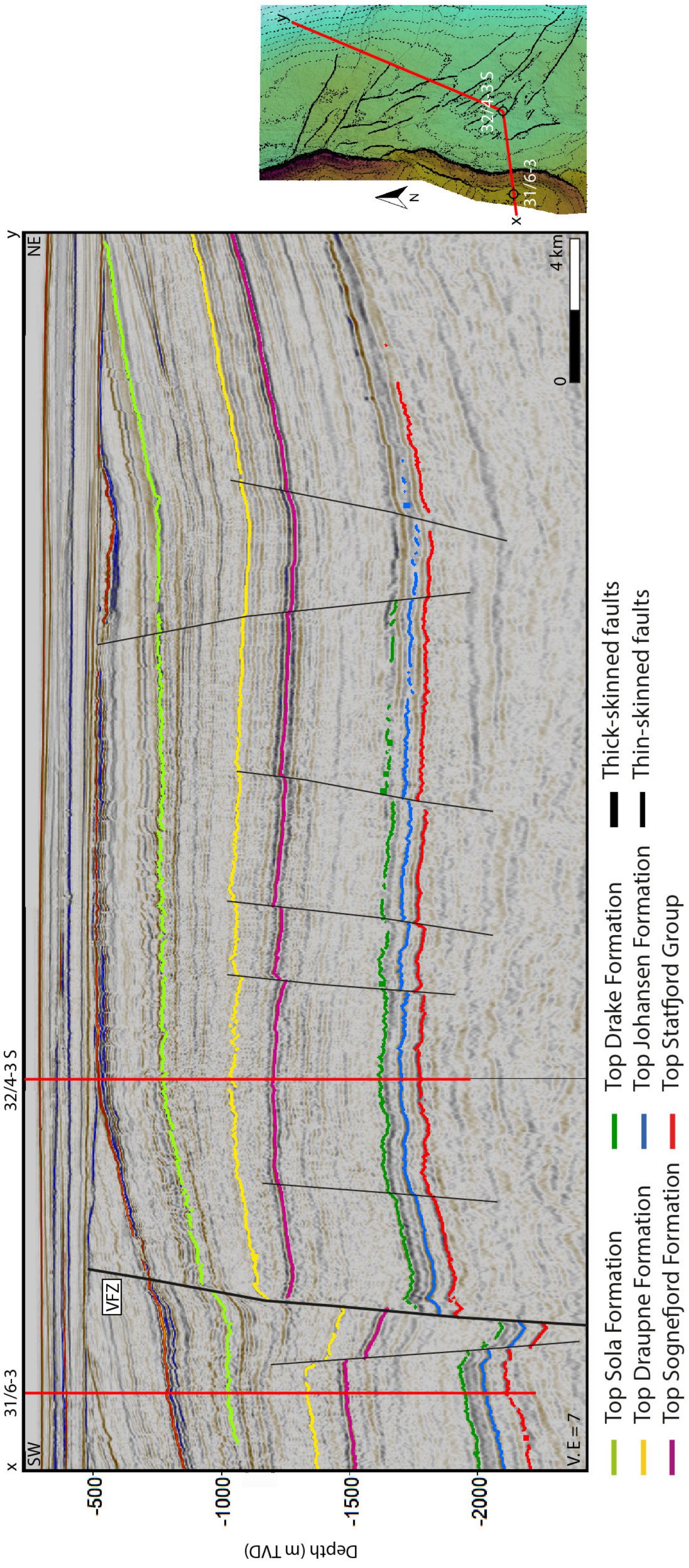
x
SW
31/6-3
32/4-3 S
y
NE
VFZ
V.E = 7
0
4 km
-500
-1000
-1500
-2000
Depth (m TVD)
Top Sola Formation
Top Draupne Formation
Top Sognefjord Formation
Top Drake Formation
Top Johansen Formation
Top Statfjord Group
Thick-skinned faults
Thin-skinned faults
y
32/4-3S
31/6-3
x
N

Figure 3.11. Seismic composite line through wells 31/6-3 and 32/4-3 S with horizon interpretations for formations/groups of interest in this study. Depth-structure map of the top Sognefjord Fm is used to show the location of the seismic composite line in the study area.

Lithological determination from well logs is often done by basic quick-look interpretation, where interpretation of logs can be made by visual inspection of appropriate well logs (Hancock, 1992). The best logs for quick-look lithological interpretation are gamma-ray, caliper, formation density, and neutron porosity (Hancock, 1992), which will be used to assess formations appropriate for CO_2 containment and entrapment, together with the 32/4-3 S drilling results from 2019, and formation descriptions from Vollset & Doré (1984).

In light of these considerations, the well-tops of the following formations and groups have been interpreted as seismic horizons: the top Statfjord Group, the top Johansen Formation, the top Drake Formation, the top Sognefjord Formation, the top Draupne Formation, and the top Sola Formation. Together, the six interpreted horizons make five successions, divided into two storage complexes, named herein the ‘primary storage complex’ and the ‘satellite storage complex’, overlain by the ‘secondary seal’ (Sola Formation). The primary storage complex is the upper storage complex within the Gamma structure, consisting of the Drake Formation and Sognefjord Formation, making the ‘primary storage, and the Draupne Formation, the ‘primary seal’. The satellite storage complex is a deeper storage complex within the Gamma structure, consisting of the Statfjord Group and the Johansen Formation, the ‘satellite storage’, and the Drake Formation, the ‘satellite seal’. Figure 3.11 shows a seismic composite line through wells 32/4-3 S and 31/6-3 with interpreted horizons associated with formation tops chosen herein. Figure 3.12 correlates the chronostratigraphy of the Horda Platform, target formations for CO_2 storage, seismic stratigraphy with interpreted horizons, and well tops.

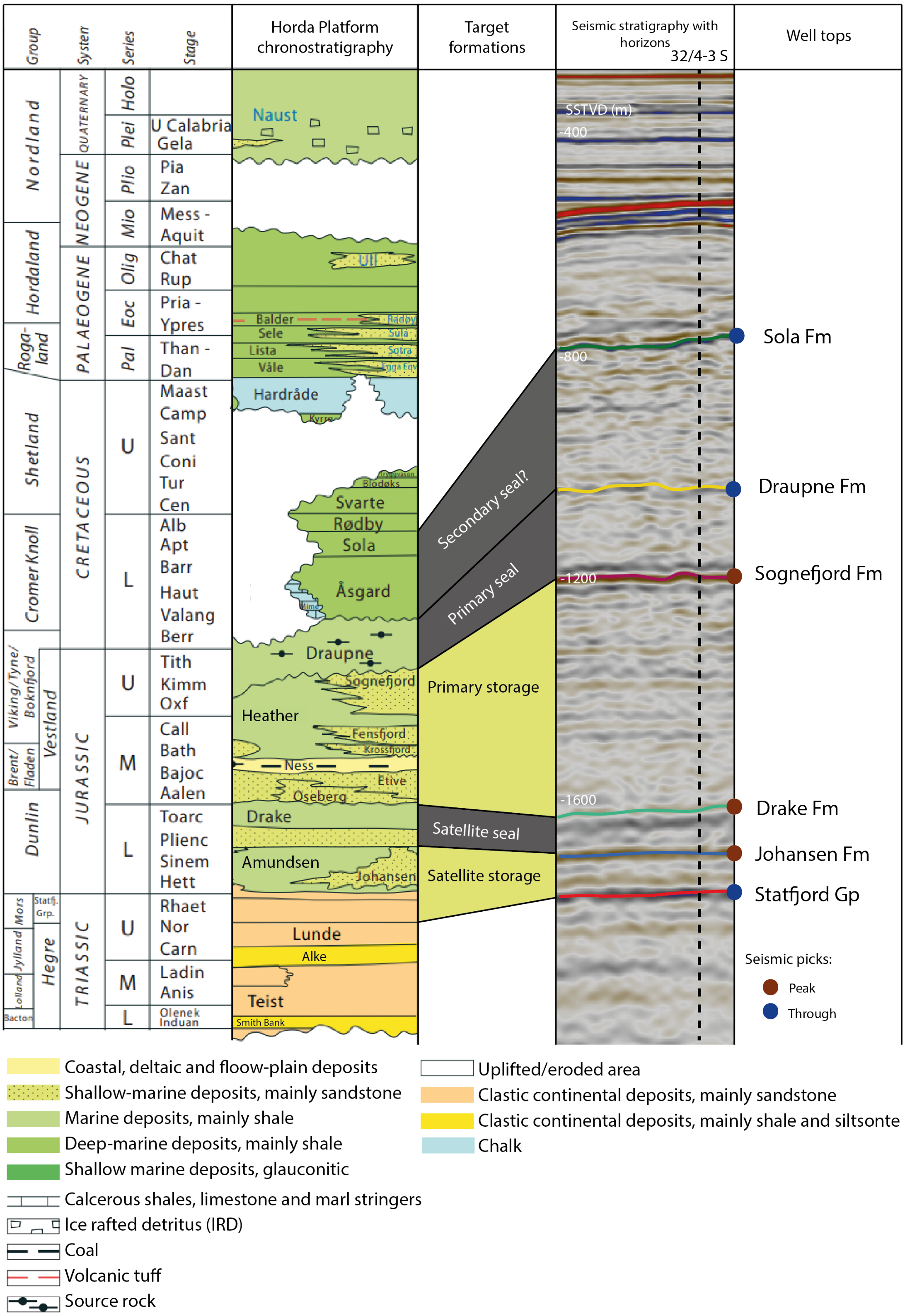

Figure 3.12. Chronostratigraphic chart of the study area within the Horda Platform sourced from NPD (https://www.npd.no/en/facts/geology/lithostratigraphy/). The potential storage complexes for CO_2 containment in the study area are highlighted. A seismic composite line through well 32/4-3 S from the NVG-HORDA-TAMPE 3D seismic survey is presented, displaying stratigraphic correlation to the chronostratigraphic chart, and interpreted seismic horizons. Inspired by Figure 3 in Mulrooney et. al (2020).

3.3.1.1 Horizon interpretation

A workflow that comprises horizon interpretation, surface modeling, and analysis is divided into seven stages in this study (Figure 3.13). The first stage involves a detailed interpretation of target horizons with inline and crossline increments that satisfy a high-resolution geomodel (Figure 3.13B): Horizon interpretation of the Drake, Draupne, and Sola formations were performed with inline and crossline increments of 4 and 25 respectively, resulting in a horizon grid with 50 x 467 m resolution. This method was chosen because one of the main objectives of this study is to discern if continuous caprock is present in the study area. Horizon interpretation of the Sognefjord Formation was conducted with inline and crossline increments of 100, making a grid of 1875 x 1250 m. Horizon interpretation of the Statfjord Group and Johansen Formation were done with inline and crossline increments of 25, making grids of 312 x 467 m. Due to the good quality of the Sognefjord Formation, Johansen Formation, and the Statfjord Group reflectors, and no structural complexity, greater inline and crossline increments were used. The horizons were further seeded 3D autotracked to fill in the gaps in the grid and make a continuous surface (Figure 3.13C), with a confidence of no less than 80%. If the 3D autotracked horizons displayed signs of interpretation errors, the gridded horizons were revised and reinterpreted, or the increments were decreased to maintain a geologically valid interpretation (i.e., quality control). This was often needed close to the VFZ, due to chaotic reflectors in the fault zone. When the autotracked horizon interpretations made geological sense and were of satisfactory quality, they were made into gridded surfaces and depth-structure maps (Figure 3.13D). All surfaces in this study were gridded with a 25 x 25 increment spacing. It is important to note that poor seismic quality can result in surface irregularities. When this was observed, an operation called ‘smoothing’ was used to reduce the irregularities in the surfaces (Figure 3.13E). Smoothing surfaces should be used with caution since the operation can result in inaccuracies and errors. In this study, the smoothing operation was applied on the surfaces of the Draupne, Johansen, and Drake formations, and the Statfjord Group, with a filter width of two. Smoothed surfaces were revised if they displayed errors that were not geological feasible.

The final step in the horizon interpretation workflow is to create isochore thickness and dip azimuth maps. Dip azimuth is a seismic horizon attribute, commonly used to address structural detail in the subsurface. The dip azimuth attribute displays the deviation of a seismic reflector from a horizontal plane. The attribute shows the direction (relative to north) that a plane is dipping, where values range from 0 – 360 degrees. Dip azimuth is a surface operation in Petrel, and the resulting map can be used to ‘roughness’ of the surface or highlight migration pathways. Dip azimuth maps were made from the Johansen and Sognefjord surfaces (top storage units); CO_2 migrates up-dip in contact with the interface between the storage unit and the seal, i.e., the storage surfaces. Isochore thickness maps show the true vertical thickness of a unit in the subsurface (Figure 3.13G). They are made by measuring the thickness between two depth-structure surfaces. In this study, thickness maps were made to assess thickness variations in the seals and the storage units and to interpret sediment accumulations to assess fault history.

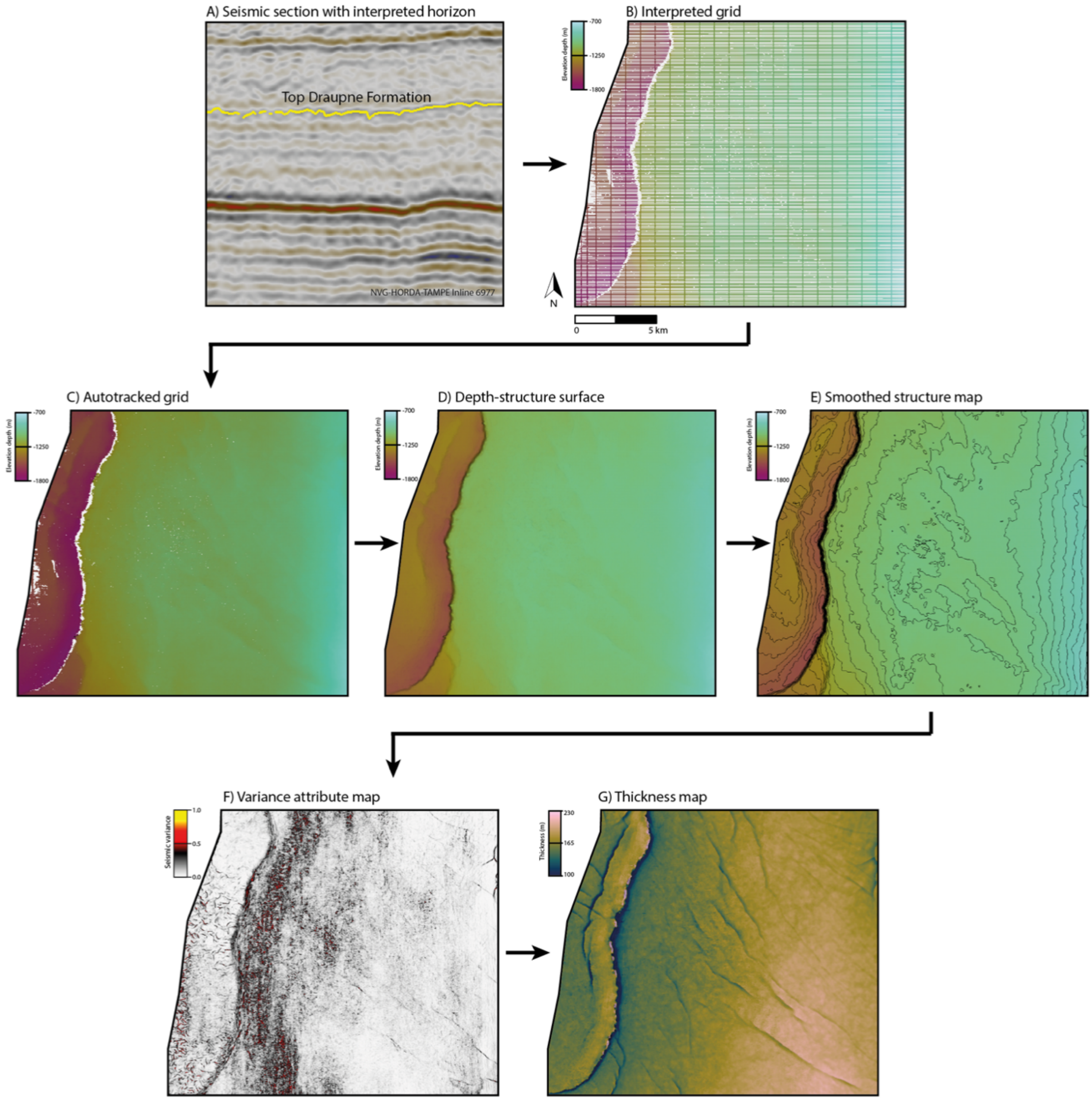

Figure 3.13. Diagram illustrating the stages of horizon interpretation using top Draupne Formation as an example: A) Interpretation of the Draupne Formation in NVG-HORDA-TAMPE inline 6977, B) interpreted grid, C) seeded

3D autotracked grid, D) depth-structure map, E) smoothed structure map, F) variance attribute map, and G) thickness map of the primary caprock. Maps in Figure B-E are made using the 'Hawaii' color scale, Figure G is made using the 'batlow' color scale from Crameri et al. (2020).

3.3.2 Fault interpretation, modeling, and analysis

This subsection outlines the workflow regarding fault interpretation, modeling, and analysis. Fault interpretations were done in the NVG-HORDA-TAMPE 3D seismic survey utilizing the Petrel E&P Software Platform. Fault modeling and analysis were performed in Petroleum Experts (PETEX) Move suite.

3.3.2.1 Fault interpretation

Fault interpretations were divided into three main steps. Firstly, a variance volume using the NVG-HORDA-TAMPE seismic cube was created in Petrel to display structural features such as faults (Figure 3.13F). The variance attribute measures the similarity of waveforms or traces adjacent over a vertical or lateral window. As such, the variance attribute can be used to image the discontinuity of reflectors in seismic data, highlighting faults in particular (Koson et al., 2014; Pigott et al., 2013). In this study, the variance attribute was generated for the entire 3D seismic cube and extracted on the interpreted surfaces. In addition, a time slice intersection was inserted in the variance volume. The time slices were used to view the lateral and vertical extent of faults and their interaction style to assist fault interpretation.

The second step is to interpret 2D fault sticks in seismic cross-sections. In seismic cross-sections, the fault itself is rarely imaged by seismic data: Faults are more often expressed as reflection terminations and offsets, which are dependent on seismic resolution. To best visualize the faults during interpretation, composite lines were oriented perpendicular to the fault strikes. A crossline and composite line spacing of 8 (100 and 113 m, respectively) were used. This is close to the optimal spacing of 100 m suggested by Michie et al. (2021). The 2D fault sticks were guided by the fault traces derived from the variance cube.

The final step is to visualize the faults as 3D fault planes and not as 2D fault sticks to quality check interpretations. Petrel creates 3D fault planes by interpolating between fault sticks. To quality check the interpreted faults, they were viewed in a 3D window to detect irregularities such as jogs and sharp spikes. Corrections were done in the seismic cross-section to ensure that the faults made geological sense. Finally, the faults were imported into Move.

3.3.2.2 Fault modeling

To determine juxtaposition seals, throw distributions, and segmentation history, a fault model must be set up. As such, fault modeling is the next step in the workflow. In total, 35 faults and 5 autotracked horizons were imported into Move. Both fault interpretations and autotracked horizons were imported as points. Fault modeling is divided into three steps in this study.

The first step is to make 3D fault surfaces of the imported points, as this is necessary to perform fault analysis. 3D fault surfaces were created by Delaunay triangulation using the imported fault points. To ensure that the resulting 3D fault surfaces were similar to the interpreted 3D fault surfaces in Petrel, they were compared and corrected if necessary. Often, when creating 3D fault surfaces by using Delaunay triangulation in Move, artifacts occur. The artifacts are inaccurate geometry in fault tips and must be corrected to make a geological valid model. Corrections were done by displaying the triangular faces on the fault surface and deleting erroneous triangles in the fault tips. When all corrections were done, branch lines (the line where two faults intersect) were created where faults were hard linked.

The second step is to assign the age, lithology, and thickness of the stratigraphic units to the horizons. The data for each horizon was taken from well 32/4-3 S, the well penetrating the Gamma structure. When performing fault modeling in Move, it is important to keep in mind that the thickness and properties of the formations are oversimplified as the data is extracted from only one well, which is only limited to a small area within the Gamma structure. Furthermore, Move provides a limited range of lithologies, for example shale, shaly sand, and sandstone. In this study, the lithologies chosen for units in Move were determined from Vollset and Doré (1984) and NPD factpages (Table 3.3).

Table 3.2. Table showing units, rock type, age, thickness, and information about lithology. Ages and lithology are from Vollset and Doré (1984) and NPD fact pages.

Stratigraphic unit	Rock type in PETEX Move	Age (Ma)	Thickness (m)	Information about unit
Draupne Fm	Shale	163.5 – 140.2	147 m	Carbonaceous, occasionally fissile claystone
Sognefjord Fm	Sandstone	163.5 – 152.1	397 m	Medium to coarse-grained sandstones
Drake Fm	Shale	182.7 – 168.3	77 m	Slight sandy, calcareous claystone. The upper part is fissile, micaceous shale containing calcareous nodules
Johansen Fm	Sandstone	199.3 – 182.7	48 m	Sandstone with thin calcite cemented streaks. The lower part is silty and micaceous claystone
Statfjord Gp	Shaly sand	208.5 – 190.8	-	Coarse-grained sandstones interbedded with silty micaceous, lignitic shales

The last step is to create cut-off lines in Move. The cut-off line method is often used in fault analysis (Bretan et al., 2011; Mulrooney et al., 2020), as it is an easy way to assess variations in fault throw and create Allan diagrams for fault juxtaposition. A cut-off line is the intersection of a given stratigraphic surface on a fault plane; the intersection is shown as a line where the hanging wall and footwall intersect the fault plane. On a normal fault, the cut-off line for the hanging wall is placed below the footwall cut-off line. For reverse faults the opposite is true. In an attempt to ensure a satisfactory quality of the cut-off lines, the raw autrotracked grid was converted to points in Petrel and imported as meshes into Move. The resulting surface maintains a high level of detail in the faulted areas. Then the 'Fault Analysis' tool was used to automatically create the cut-off lines. In the Fault Analysis tool, faults, branch lines – if two or more faults are hard-linked, and horizons are assigned as inputs for fault cut-off line calculation. In addition to the input data, trim distance (part of the horizon from the top of the fault plane that will be excluded when creating cut-offs), and an inclusion distance (a part of the horizon from the top of the fault plane that will be included when creating cut-offs) must be estimated, and these distances where found by measuring the length of areas around the fault that the footwall transected though the fault plane. Finally, it is important to quality control the automatically created cut-off lines. This was necessary for areas where the fault throw was close to the vertical resolution, or where the seismic resolution was poor.

3.3.2.3 Fault analysis

Fault analysis is the final step in the workflow and was used to assess the spatial and temporal evolution of faults, the presence of across-fault seals, and their influence on CO_2 migration. In this study, the fault analysis included creating throw profiles, fault throw diagrams, maximum throw vs. length plots, and Allan diagrams.

To determine fault propagation and interaction styles, throw vs. length profiles were created (subsection 4.1.3.4). The throw vs. length profiles were created in the software Move by measuring the vertical distance between the footwall and hanging-wall cut-off lines in the geomodel. Maximum throw vs. length plots were made to get a quantitative overview of the maximum throws for several faults within the study area. Maximum vs. length plots were made in Move by making footwall and hanging-wall cut-off lines for each interpreted horizon for 22 faults within the study area, and then determining the maximum vertical distance between the cut-off lines.

Juxtaposition analyses were done by using Allan diagrams generated in the software Move. The Allan diagrams were made using the modeled cut-off lines by displaying areas where permeable and non-permeable units juxtapose in the fault plane (subsection 3.1.2.1). Each interpreted unit was assigned a lithology (sandstone, shale, silt), and each mode of juxtaposition was assigned a color (yellow for sandstone on sandstone, brown for shale on sandstone, and black for shale on shale).

3.3.3 Volumetric analysis and estimation of storage capacity

The next step in the workflow is to map geological traps (i.e., closures) and estimate bulk volumes and storage capacities of mapped closures. Closures were identified by inspecting the mapped depth-structure surfaces with contour lines (Figure 3.13E).

For saline aquifers in the subsurface, the amount of CO_2 to be stored can be calculated using the following formula (Halland et al., 2011):

$$M_{CO_2} = V_b \cdot \Phi \cdot \frac{n}{g} \cdot \rho_{CO_2} \cdot S_{eff}$$

Where

M_{CO2} = gravimetric storage capacity = kg;
V_b = bulk volume of the potential formation = m^3;
Φ = porosity = %;
n/g = proportion of sediment with porosity and permeability suitable for absorbing CO_2 (net-to-gross ratio) = %
P_{CO2} = density of CO_2 at storage unit depth = kg/m^3
S_{eff} = storage efficiency factor, fraction of stored CO_2 relative to pore volume = %.

The bulk volume (V_b) inside a closure is calculated in Petrel by using an assigned surface and an assigned spill point. The assigned surfaces are the storage units, the top Sognefjord and Johansen formations. The base level is the depth of the spill point of the structural closure. A polygon outlining the prospect is used as a boundary to calculate the volume accurately. The values for porosity (Φ) and net-to-gross ratio (n/g) are derived from neutron and gamma-ray well logs from well 32/4-3 S. Density of CO_2 at storage unit depth (P_{CO2}) and storage efficiency (S_{eff}) values are derived from the CO_2 storage atlas for the Norwegian Continental Shelf (i.e., Halland et al. (2011).

The parameters used to determine the bulk volume and storage capacity of the structural closure are summarized in Table 3.4.

Table 3.3. Table summarizing parameters used to estimate storage capacity of the Gamma prospect. Bulk volumes are shown in chapter 4.

Storage unit	V_b **(m^3)**	Φ **(%)**	n/g **(%)**	P_{CO2} **(kg/m^3) from Halland et al. (2011)**	S_{eff} **(%) from Halland et al. (2011)**
Primary storage unit	Shown in chapter 4	0.33	1	670	0.05
Satellite storage unit	Shown in chapter 4	0.30	1	710	0.03

3.3.4 Migration pathway analysis

The final step in the workflow is to determine CO_2 injection points and migration pathways to the Gamma prospect.

Hydrocarbons and CO_2 of lighter density will always travel up dip in the direction of maximum gradient in the subsurface, due to buoyancy forces. The only requirement for identifying migration pathways is the topography of the top seal in a storage complex, which can be interpreted from seismic data (Weibull et al., 2010). Permeability barriers such as sealing faults or starata-pinch outs may baffle or interrupt fluid migration, in which the fluid might accumulate downdip of the seal. Furthermore, fluids may migrate up dip until it reaches a structural trap (closure). If the supply of fluid exceeds any eventual leakage, the fluid will eventually fill this closure. Excessive fluid could then spill and migrate up dip by using other permeable paths along the strata until fluids may arrive at other traps (fill and spill migration) (Weibull et al., 2010).

This study will use 3D seismic data, more specifically depth-structure maps (3.13E) of the top storage units, as these surfaces represent the topography of the seal, to determine migration pathways and injection points. In addition to depth-structure maps, dip azimuth maps of the same surfaces will be used to aid the interpretation of migration pathways, as these maps show dip directions in the interface between storage unit and seal. Furthermore, fault analysis is completed on faults of interest to determine the presence of across-fault seals (subsection 3.3.2.3) to assess possible baffles, conduits, or barriers for fluid migration.

4 Results

As a reminder, the main objective of this study is to determine the structural framework of the Gamma storage site, estimate the storage capacity of the closures, assess the presence of across fault seals, and finally discuss possible CO_2 migration pathways. In this chapter, results are presented to inform the stratigraphic architecture (section 4.1.1 – 4.1.2), the structural architecture (section 4.1.3), across-fault juxtapositions (subchapter 4.2), and finally storage capacities of closures (subchapter 4.3) in Gamma and the study area.

4.1 Stratigraphic and structural characterization

Cross-sections, well-logs, depth-structure maps, dip azimuth maps, variance maps, and isochore maps were interpreted to investigate the tectonostratigraphic architecture of the study area, particularly the Gamma structure, and to determine how this will affect the migration of CO_2.

4.1.1 The Gamma storage site

The study area is in the Smeaheia fault block and is bordered by two large, N–S trending fault zones, the Vette Fault Zone and the Øygarden Fault Complex (Figure 1.1). Regionally, these fault zones are in the northern Horda Platform, creating an N-S striking fault block containing wedge- and sheet-shaped sedimentary units (Figure 3.9), deposited during phases of rifting and tectonic quiescence in the North Sea (Duffy et al., 2015; Phillips et al., 2019).

The Gamma prospect, a suggested storage site for CO_2 (Lothe et al., 2019), is in the south of the study area, approximately 3.8 km east of the VFZ (Figure 4.1). In addition to Gamma, two other prospects have been mapped and studied in previous publications in Smeaheia, the alpha and beta prospects (Mulrooney et al., 2020; Wu et al., 2021) (Figure 4.1). In these publications, the Viking Group sandstones, mainly the Sognefjord Formation, were established as potential storage aquifers for CO_2. In addition to the Viking Group sandstones, deeper sandstones within the Dunlin Group have also been suggested as potential storage aquifers (Mulrooney et al., 2020; Wu et al., 2021). In this study, the same aquifers are considered for CO_2 storage, as the alpha and beta prospects are in proximity to the Gamma prospect (Figure 4.1). Logs from well

32/4-3 S (Figure 4.2), seismic composite lines intersecting wells 31/6-3, 32/4-3 S, 32/4-1 T2, and 32/2-1 (Figure 4.3 and 4.4), depth-structure maps for all interpreted horizons (Figure 4.5), and dip azimuth maps (Figure 4.6) are presented to provide an overview of the gross stratigraphic and structural architecture in the study area and Gamma. All maps and seismic cross-sections are presented in depth-domain.

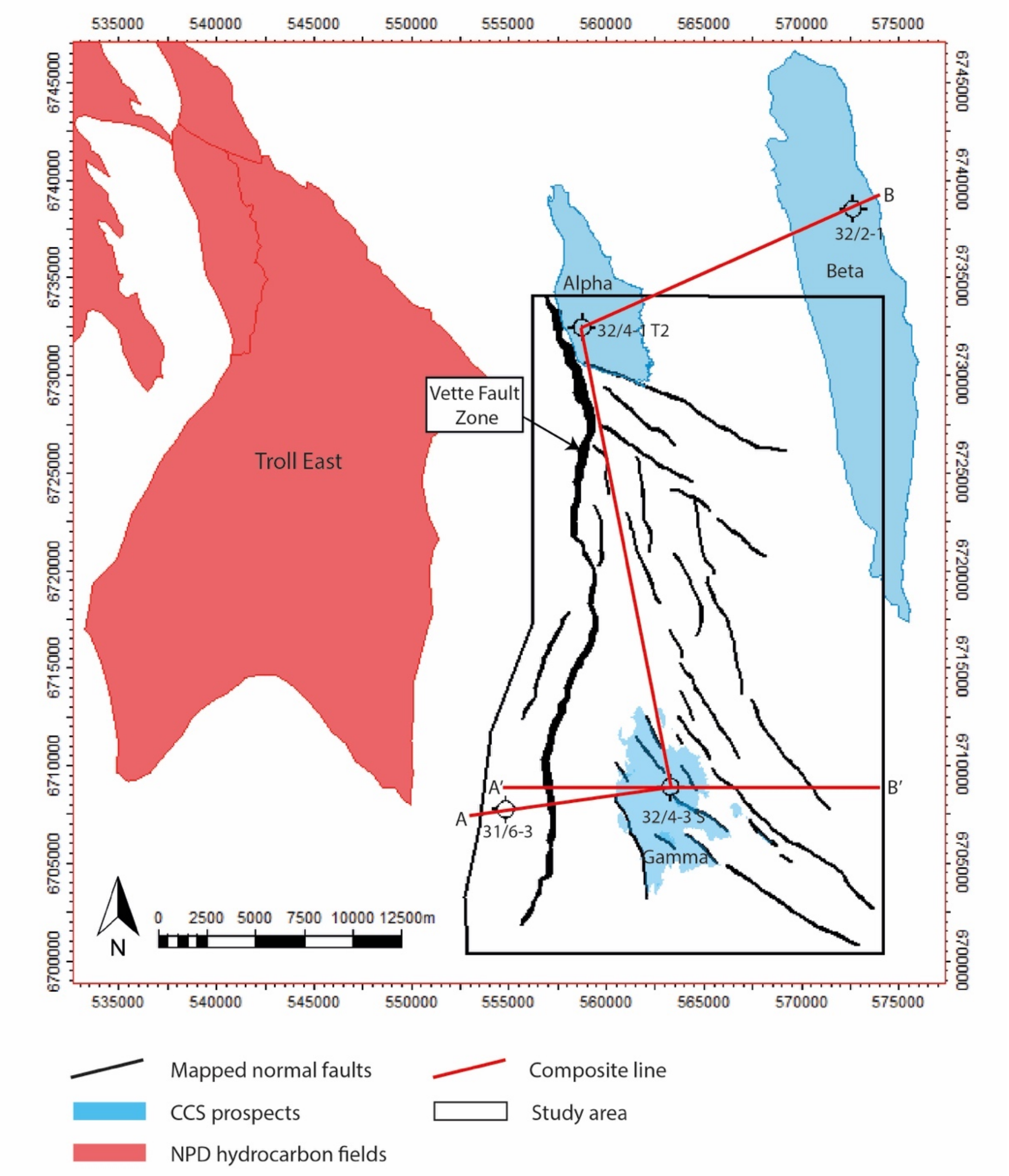

Figure 4.1. Map showing the structural elements, storage prospects within the study area, and a seismic composite line shown in Figure 4.3 and Figure 4.4. Mapped faults are displayed as heave polygons derived from the top Sognefjord Formation (i.e., the primary storage unit). Wells used in this study are included in the figure.

Gamma-ray, caliper, neutron, and density logs from well 32/4-3 S were used to assess the stratigraphy in Gamma (Figure 4.2). The well penetrates the Upper Triassic top Statfjord Group at the deepest (Figure 4.3) and the total vertical depth is 2 km (NPD, 2019). The gamma-ray, caliper, neutron, and density logs show an abrupt change in rock properties at the formation boundary between the Sognefjord and Draupne formation well tops, and Johansen and Drake formation well tops (Figure 4.2). The abrupt changes in rock properties can be interpreted as an increase in shale content, as the gamma-ray, caliper, and density log show higher values up-section in the logs (Figure 4.2). The opposite is observed in the logs down-section from the Sognefjord and Johansen formation well tops, as the logs overall decrease in gamma-ray, caliper, and density values, indicating a more porous rock, interpreted as a sandstone herein (Figure 4.2). Note that the neutron porosity log exhibits higher porosity values in the Draupne and Drake formations (Figure 4.2), which are herein interpreted as mudstones. This may be an indication of high water content in the mudstone; high neutron porosity readings are known to occur for mudstones with high water content, as water molecules can chemically bind to clay minerals (Hancock, 1992).

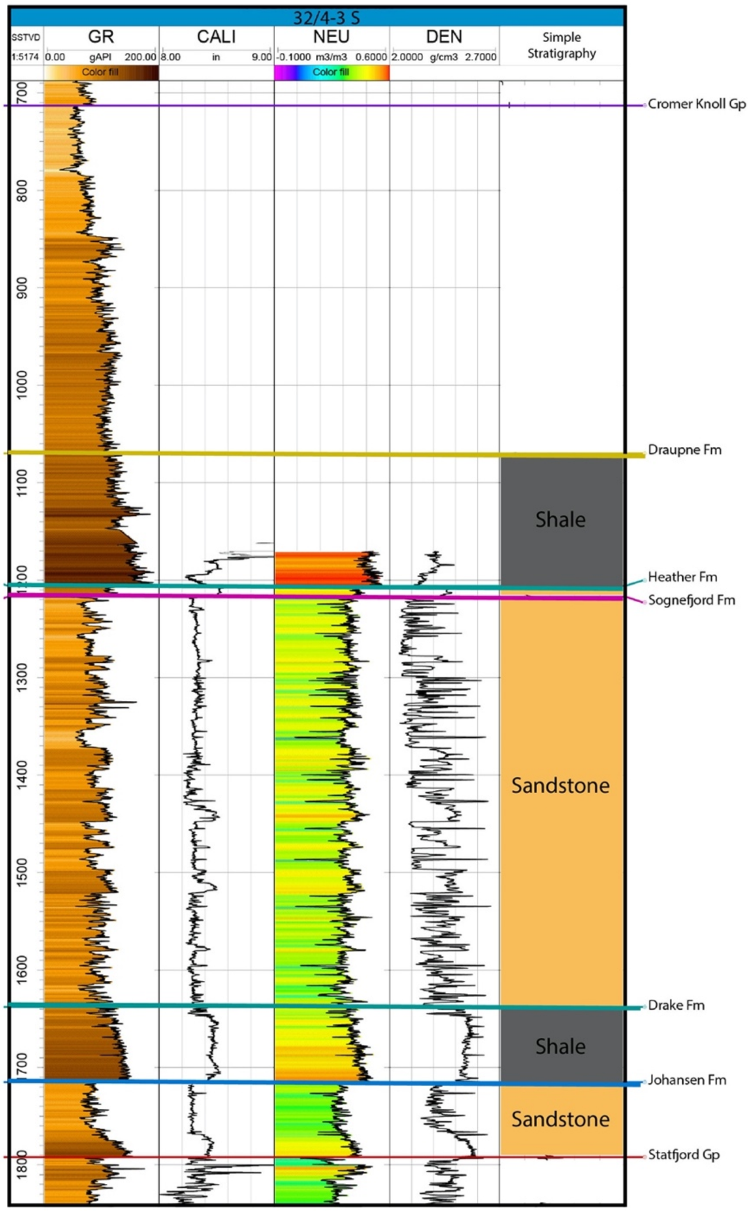

Figure 4.2. Well logs from well 32/4-3 S. Gamma-ray, caliper, neutron, and density logs are shown with well tops for the Cromer Knoll Group, Draupne, Heather, Sognefjord, Drake, and Johansen formations, and Statfjord Group.

A composite seismic line through wells 31/6-3, 32/4-3 S, 32/4-1 T, and 32/2-1 is presented to give an overview of the structural and stratigraphic architecture in the Gamma structure and the study area (Figure 4.3). In addition, a seismic section through well 32/4-3 S is presented to give an overview of the study area from west to east (Figure 4.4). In the seismic section and composite line, the units making the primary storage complex, satellite complex, and the overburden/secondary seal (i.e., Sola Formation) have been interpreted (Figure 4.2 & 4.4). A summary of seismic facies parameters used in this study is shown in Table 4.1.

Table 4.1. List of horizons associated units, and seismic facies parameters, used for the horizon interpretation within the NVG-HORDA-TAMPE 3D seismic volume in this study. Note that the external form and the internal configuration are not included for the Statfjord Gp, as this is beyond the scope of this study.

Unit/seismic facies	External form	Internal configuration	Unit top	Reflector pick	Amplitude	Continuity
Secondary seal	Wedge	Divergent	**Top Sola Fm**	Through	Large	Continuous
Primary seal	Sheet	Subparallel	**Top Draupne Fm**	Through	Small	Continuous
Primary storage	Sheet	Subparallel	**Top Sognefjord Fm**	Peak	Large	Continuous
Satellite seal	Wedge	Convergent	**Top Drake Fm**	Peak	Medium	Semi-continuous
Satellite storage	Wedge	Convergent	**Top Johansen Fm**	Peak	Large	Semi-continuous
-	-	-	**Top Statfjord Gp**	Through	Medium	Semi-continuous

Furthermore, the interpreted surfaces associated with the storage complexes are presented in map-view in depth-domain to determine the structural framework and the spatial distribution of formations and groups within the study area and the Gamma structure (Figure 4.5). The depth-structure maps include the top Statfjord Group, top Johansen, top Drake, top Sognefjord, top Draupne, and top Sola formations (Figure 4.5A-F). Note that the top Sola Formation was only interpreted in the southern half of the study area where the Gamma structure is located (Figure 4.5F). The maps show that all interpreted surfaces have similar geometries and are offset by the Vette Fault to the west of the study area (Figure 4.5). Overall, the horizons shallow towards the east, being the shallowest in the northeast for the Sognefjord and Draupne formations (Figure 4.5D-E) and in the southeast for the Statfjord Group, Johansen, and Drake formations (Figure 4.5A-C). However, the geometry of the top Sola Formation (Figure 4.5F) differs from the others in terms of faulting (Figure 4.5A-E), as the faults observed in the top Sola Formation seem to be polygonal. Faults within the study area will be discussed in more detail in section 4.1.3.

The deepest surfaces, the top Statfjord Group, top Johansen, and top Drake formations have no data in the northeast, due to the reflections associated with said formations/groups disappearing in the seismic data (Figure 4.5A-C). Both Johansen and Drake formations are observed to pinch-out, thinning towards the northeast (Figure 4.3). The reflectors associated with the Johansen and Drake formations have a convergent internal configuration (Table 4.1), indicating syn-sedimentary thinning by a decrease in sediment supply.

The reflection associated with the top Statfjord Group is absent in the northeast (Figure 4.5A-C). The top Sola Formation has no reflection in the southeast, as it is truncated by Cenozoic sediments, creating an angular unconformity with overlying strata (Figure 4.4). The reflectors associated with the Sola Formation have a divergent internal configuration (Table 4.1), indicating syn-sedimentary thickening caused by an increase in accommodation space. The internal configurations of the Draupne and Sognefjord Formations have been interpreted to be subparallel (Table 4.1), as the reflectors in the formations are observed to be mostly parallel with a small degree of reflector thinning and thickening (Figure 4.3 & Figure 4.4), indicating close to uniform depositional rates on a uniformly subsiding surface.

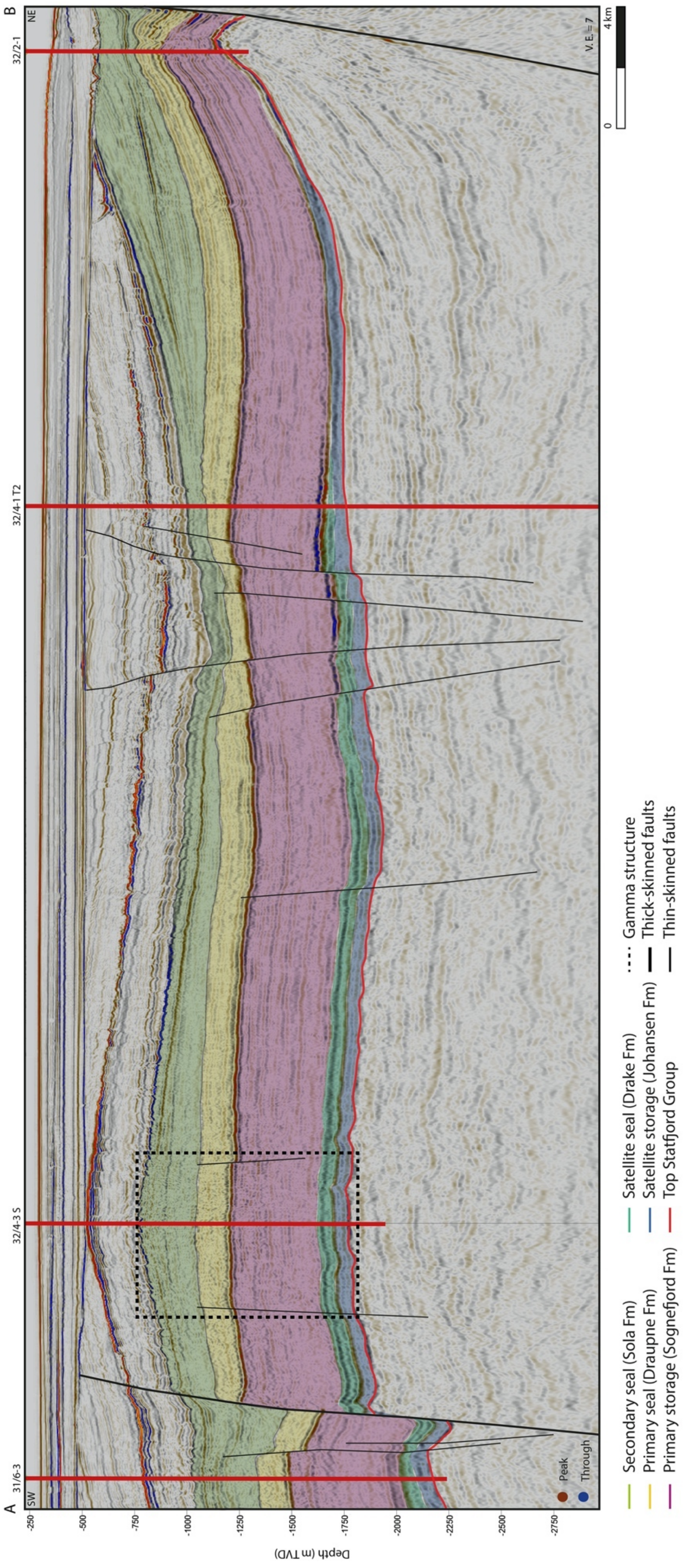
A
B
SW
NE
31/6-3
32/4-3 S
32/4-1 T2
32/2-1
Depth (m TVD)
-250
-500
-750
-1000
-1250
-1500
-1750
-2000
-2250
-2500
-2750
Peak
Through
V.E. = 7
0
4 km
Secondary seal (Sola Fm)
Primary seal (Draupne Fm)
Primary storage (Sognefjord Fm)
Satellite seal (Drake Fm)
Satellite storage (Johansen Fm)
Top Statfjord Group
Gamma structure
Thick-skinned faults
Thin-skinned faults

Figure 4.3. Seismic composite line A-B through wells 31/6-3, 32/4-3 S, 32/4-1 T2, and 32/2-1 shown in Figure 4.1.). The Gamma structure and storage and seal units are highlighted in the seismic image. Thick-skinned and thin-skinned faults are interpreted, VFZ furthest to the southwest, and ØFC furthest to the northeast.

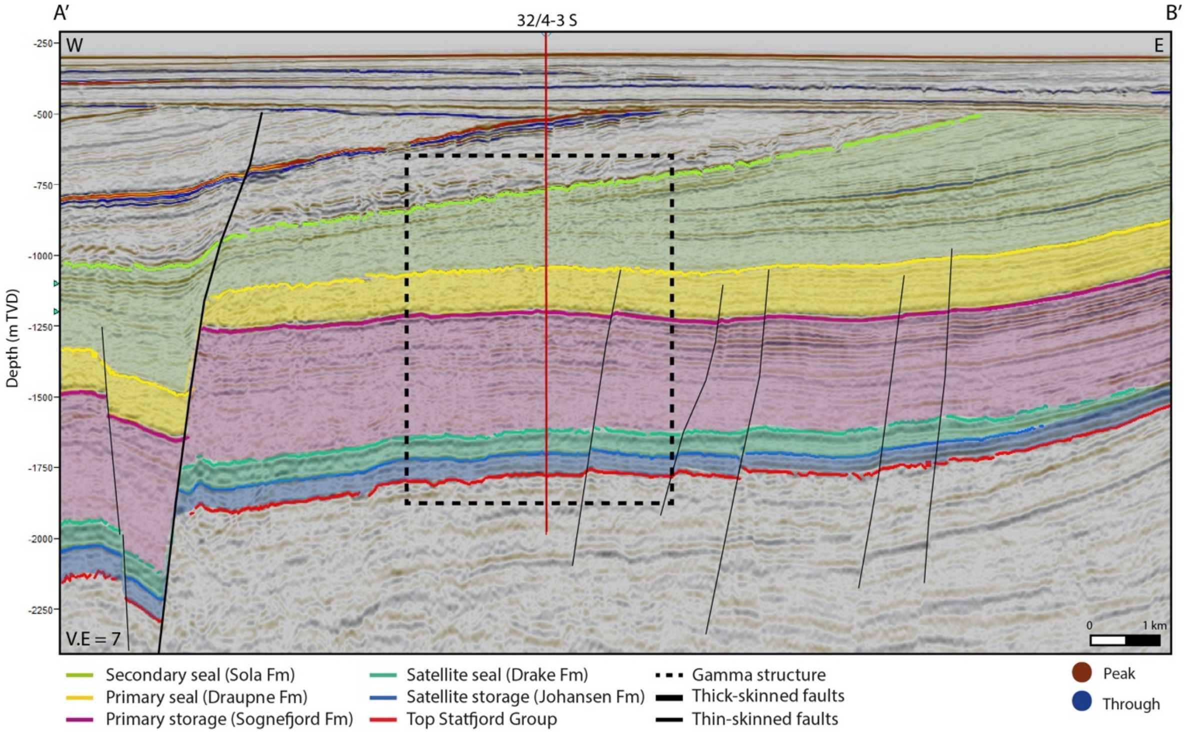

Figure 4.4. Seismic composite line A'-B' through well 32/4-3 S shown in Figure 4.1. The Gamma structure and storage and seal units are highlighted in the seismic image. Thick-skinned and thin-skinned faults are interpreted.

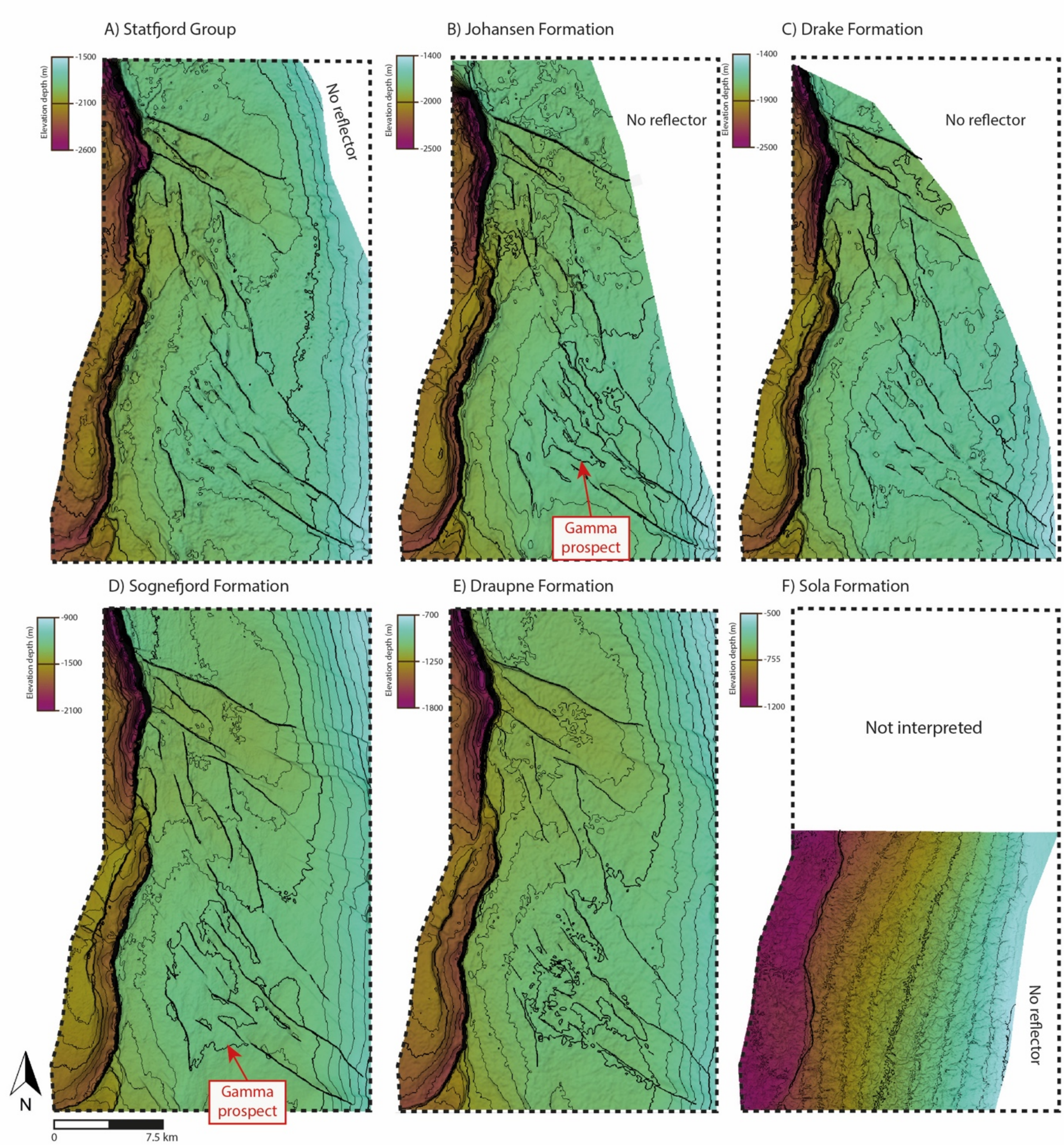

Figure 4.5. Depth-structure maps of the six interpreted horizons in the study area. Faults are shown as heave polygons. A) Top Statfjord Group. 35 m contour spacing. B) Top Johansen Formation. 31 m contour spacing. Note the closure marked as Gamma prospect. C) Top Drake Formation. 35 m contour spacing. D) Top Sognefjord Formation. 25 m contour spacing. Note the closure marked as Gamma prospect. E) Top Draupne Formation. 30 m contour spacing. D) Top Sola Formation. 50 m contour spacing. Note the polygonal faults showing in the surface.

Dip azimuth maps are presented to highlight the roughness and dip directions for the top Johansen and Sognefjord surfaces (Figure 4.5B & D) with closures highlighted (Figure 4.6). Both surfaces show similar geometries: In the south, along the eastern side of the Vette Fault Zone, the surface dips to the west, whereas in the northwest it dips to the east (Figure 4.6). In the southeast and south, both surfaces dip predominately to the west and south, respectively (Figure 4.6). However, in the top Sognefjord Formation, within the Gamma closure and along the middle of the study area, the surface dips predominately to the east and northeast (Figure 4.6A). The same trend can be observed in the top Johansen Formation (Figure 4.6B). Furthermore, the Top Sognefjord Formation shows dip directions predominately to the west in the northeast (Figure 4.6A).

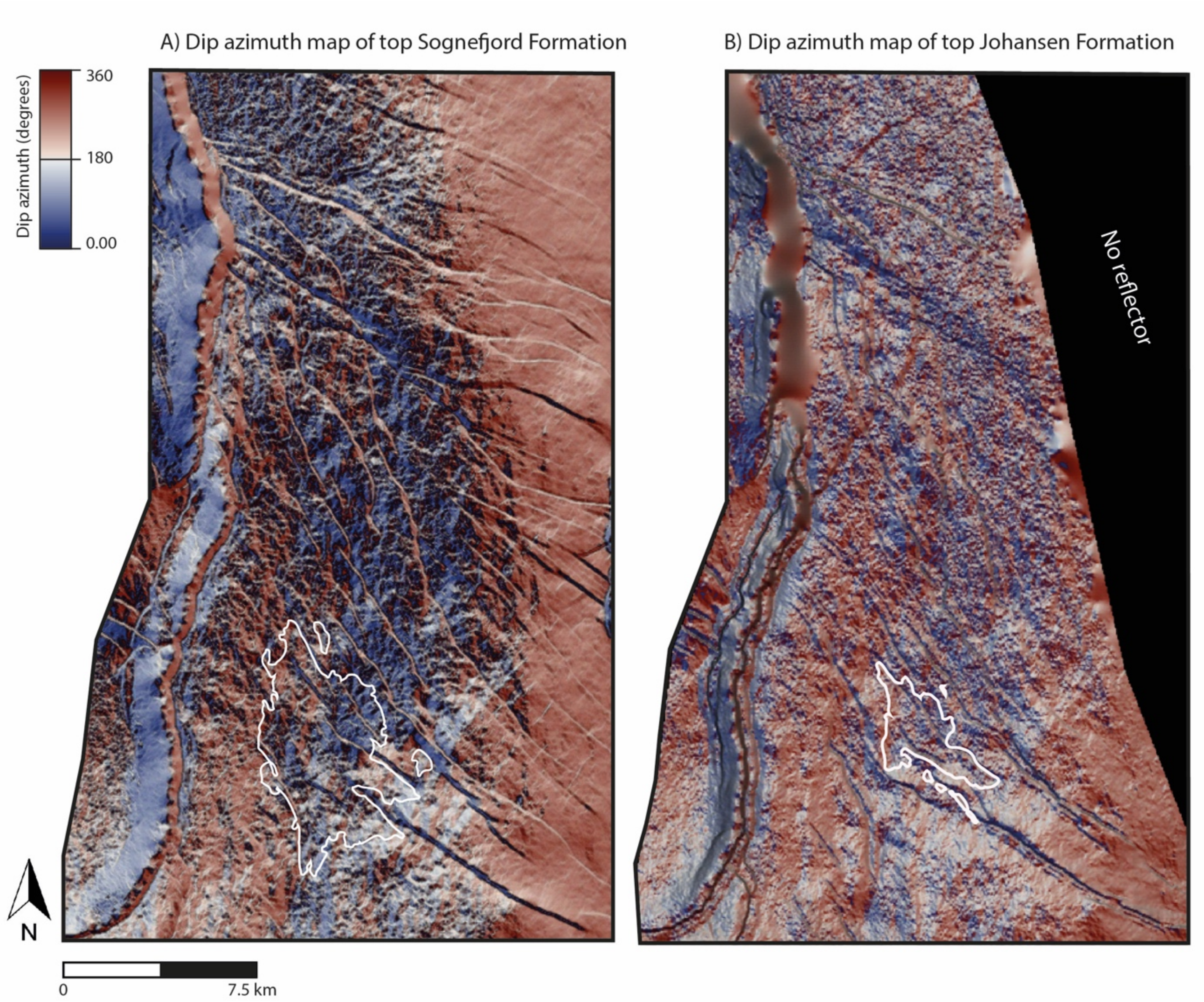

Figure 4.6. Dip azimuth maps of the storage units in the study area. Blue and red represent opposite dip directions. Closures for each formation top within the Gamma structure are highlighted in white. A) Top Sognefjord Formation. B) Top Johansen Formation. Note that there is no reflector in the northeast due to the Johansen Formation is pinching out.

4.1.2 Target successions

Thickness variations can be observed in the seismic composite line in Figure 4.3, the seismic section in Figure 4.4, and thickness maps (Figures 4.7, 4.8, & 4.9). The thickness maps are represented with seismic cross-sections approximately perpendicular to the faults in the Gamma structure, to aid the assessment of storage and seal thicknesses (Figures 4.7, 4.8, & 4.9). The thickness maps are shown with different color ranges, to best visualize the thickness variations in respective maps.

The Jurassic Sognefjord Formation (i.e., the target formation for CO_2 storage) and the Jurassic-Cretaceous Draupne Formation (i.e., the primary seal) show little thickness variations in the Gamma structure, but also throughout the seismic profiles (Figure 4.3 & 4.4). However, one exception is southwest to well 32/4-1 T2, where the formations are faulted and thinner (Figure 4.3). Minor thickness variations are observed for the Jurassic Johansen and Drake formations across the Gamma structure, but they are interpreted to thin and disappear to the northeast within the seismic composite line (Figure 4.3). Furthermore, the well-tops associated with the Johansen and Drake formations are not observed in the northeast (Figure 3.10). The secondary seal displays large thickness variations throughout the seismic composite line, being at its thickest at the Gamma structure, making a dome structure in profile view (Figure 4.3). The secondary seal thickens also to the southwest and towards the thick-skinned Øygarden Fault Zone (not mapped herein), however, the formation has an angular unconformity with overlying strata (Figure 4.4).

4.1.2.1 The primary storage unit

The primary storage unit consists of the Sognefjord formations and the Fensjord, Krossfjord, and Etive formations – as the top Drake Formation is established as the lower boundary of the primary storage unit (Figure 3.11). The thickness map of the primary storage unit shows that the northeast part is not mapped in the study area, as the Drake Formation pinches out, which is defined as the lower boundary for the primary storage unit, is missing in the northeast (Figure 4.7B).

The primary storage unit is the thickest in the west, around the Vette Fault Zone, where it reaches 500 m (Figure 4.7B). At the Gamma structure, it reaches approximately 430 m and thins to 400 m around the faults within the structure (Figure 4.7B). The thinnest parts of the primary storage unit are in the southeast, where it is 320 m (Figure 4.7B). The mean thickness of the primary storage unit is 416 m. The primary storage unit appears to have the same thickness in the footwall and in the hanging wall of the Vette Fault Zone, close to the fault (Figure 4.7B), but as the thickness variations further to the west are not mapped herein, however, by examining the seismic cross-section in Figure 3.9, the unit seems to be uniform in said area.

A seismic composite line is presented in Figure 4.7C to show the thickness variations in Gamma in profile view.

4.1.2.2 The primary seal unit

The primary seal unit consists of the Draupne Formation. The top Sognefjord Formation represents the base of the primary seal unit. The thickness map of the primary seal unit shows that it covers the entire study area (Figure 4.7A).

The primary seal has a mean thickness of 167 m. Across the Gamma closure, the primary seal is approximately 160 m (Figure 4.7A). The primary seal is the thickest in the southeast of the study area, where it reaches approximately 200 meters (Figure 4.7A). Along the Vette Fault Zone, it thins to approximately 120 m into the fault (Figure 4.7A). This trend is the opposite of what is observed in the underlying primary storage unit.

The seismic composite line in Figure 4.7C shows that the primary seal is faulted within the Gamma structure, but the thickness of the seal is close to uniform except close to the Vette Fault Zone (Figure 4.7A).

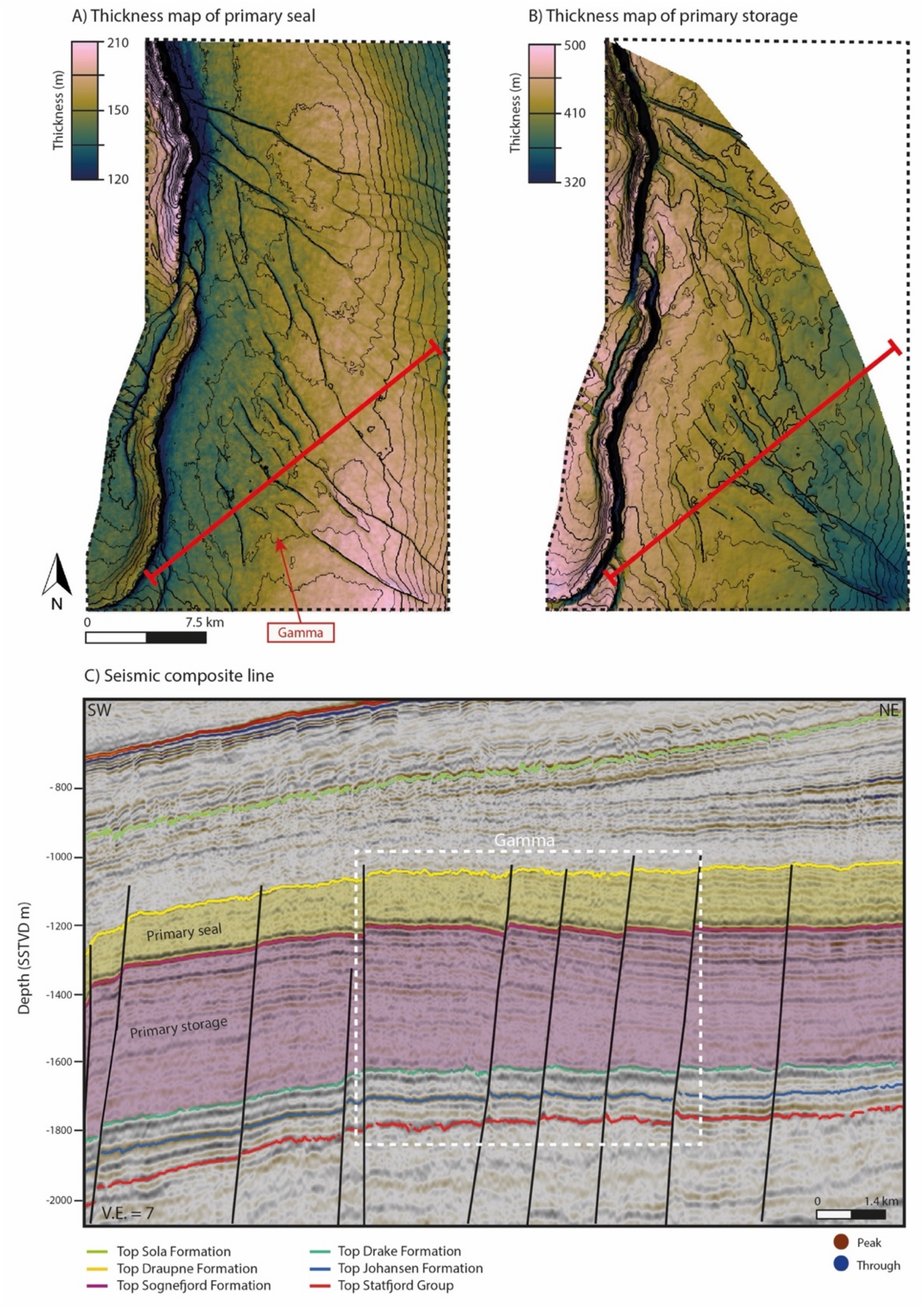

Figure 4.7. A) Thickness map of the primary seal unit with 25-meter contour line spacing. Faults are shown as heave polygons. B) Thickness map of the primary storage unit with 25-meter contour line spacing. Faults are shown as heave polygons. C) Seismic composite line highlighting Gamma structure and the primary storage and seal units.

4.1.2.3 The satellite storage unit

The satellite storage unit consists of the Johansen and Amundsen formations (Figure 3.11). The top Statfjord Group represents the base of the satellite storage unit. The thickness map of the satellite storage unit shows that the northeast part is missing in the study area, as the reflection for the top Statfjord Group disappears here, and the Johansen Formation pinch out (Figure 4.8B).

The thickness of the satellite storage unit is close to uniform in the study area, having a mean thickness of 75 m, except in the southwest (Figure 4.8B). Here, the satellite storage unit is the thickest in the hanging wall of the Vette Fault Zone, measuring 140 m (Figure 4.8B). The satellite storage unit is thinnest where the unit pinch-out, measuring 40 – 65 m.

The seismic composite line in Figure 4.8C shows that the satellite storage unit is faulted but have a close to uniform thickness within the Gamma structure, with a thickness of approximately 70 m.

4.1.2.4 The satellite seal unit

The satellite seal unit consists of the Drake Formation. The top Johansen Formation represents the base of the unit. The thickness map of the satellite seal unit shows that the northeast part is missing in the study area, as the reflection for the top Johansen Formation disappears and the top Drake Formation pinch out (Figure 4.8A).

The secondary seal is the thickest in the southwest of the study area, with a thickness of approximately 80 – 90 m (Figure 4.8A). The secondary seal thins toward the northwest, where it reaches 40 – 70 m (Figure 4.8A). The mean thickness for the satellite seal is 75 m.

Within the Gamma prospect, the seal is approximately 80 m (Figure 4.8A). The satellite seal unit is faulted but close to uniform within the Gamma structure (Figure 4.8C).

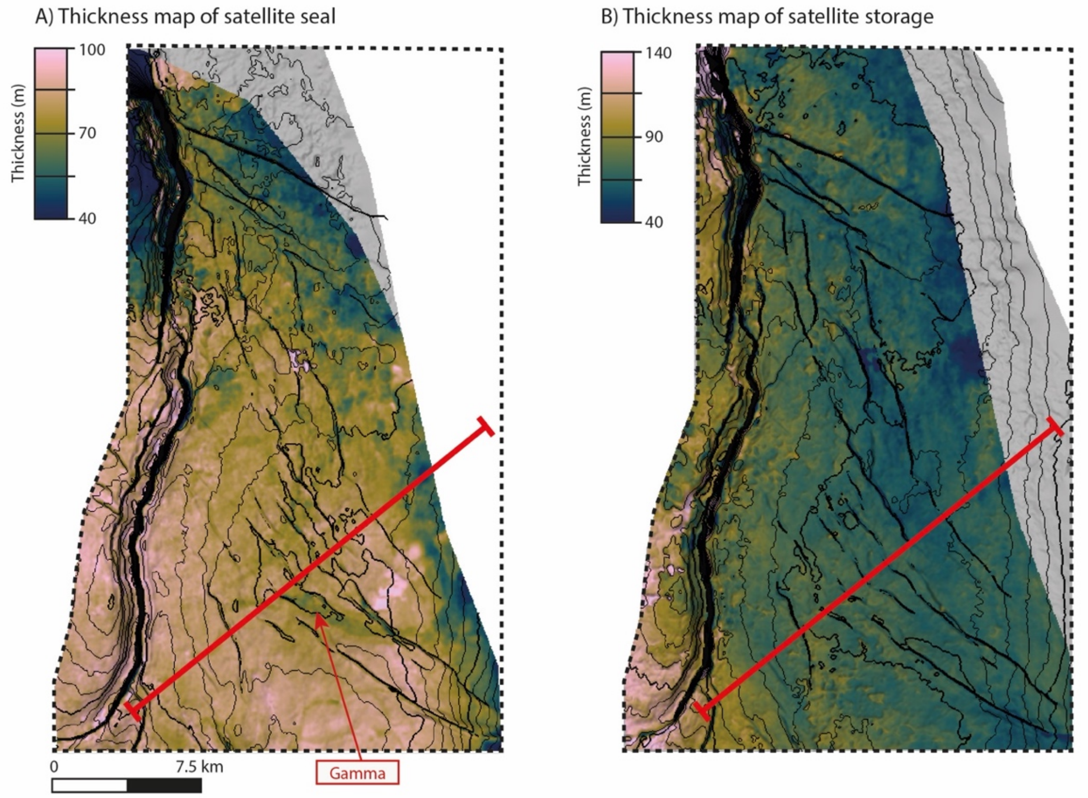

A) Thickness map of satellite seal

B) Thickness map of satellite storage

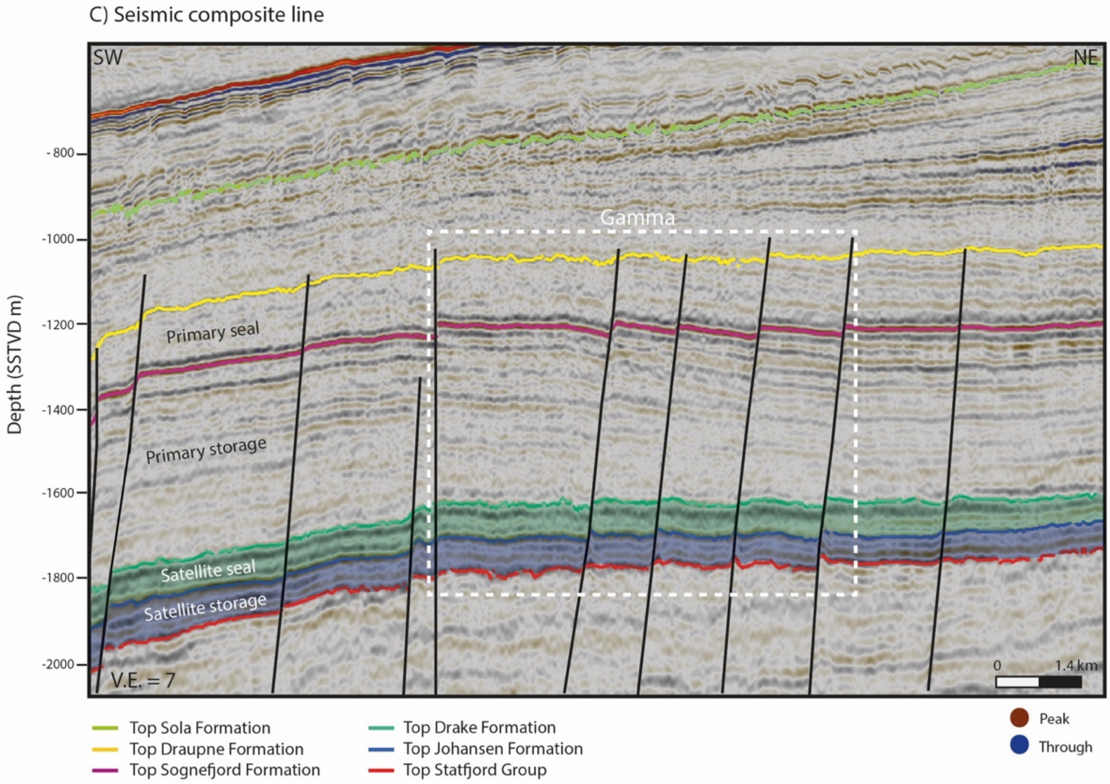

C) Seismic composite line

Figure 4.8. A) Thickness map of the satellite seal unit with 35-m contour line spacing. Faults are shown as heave polygons. B) Thickness map of the satellite storage unit with 35-m contour line spacing. Faults are shown as heave polygons. C) Seismic composite line highlighting the Gamma structure and the satellite storage and seal units.

4.1.2.5 Secondary seal unit

The secondary seal unit consists of the Sola and Åsgard formations (Figure 3.11). The top Draupne Formation is assigned as the lower boundary of the unit. As a reminder, only the southern parts of the Sola formation were mapped in the study area, around the Gamma structure (Figure 4.9A). The thickness map shows that there is no reflector in the southeast (Figure 4.9A), as the Sola Formation is truncated by an creating an angular unconformity (Figure 4.4).

The secondary seal unit thins from east to the west until it reaches the Vette Fault Zone, where it reaches 100 meters in thickness (Figure 4.9A). The secondary seal is thickest in the eastern parts and west of the Vette Fault Zone, reaching 600 meters (Figure 4.9A). The thickness is approximately 200 meters over the Gamma structure (Figure 4.9A). The mean thickness of the secondary seal unit is 494 meters. The thickness variations indicate syn-sedimentary deposition of the Sola Formation caused by an increase in accommodation space, as the formation is thickening from west to east toward the thick-skinned Øygarden Fault Zone.

Figure 4.9B is a seismic composite line showing the secondary seal unit in profile view; the thickness of the unit increases to the northeast and thins to the southwest.

A) Thickness map of secondary seal

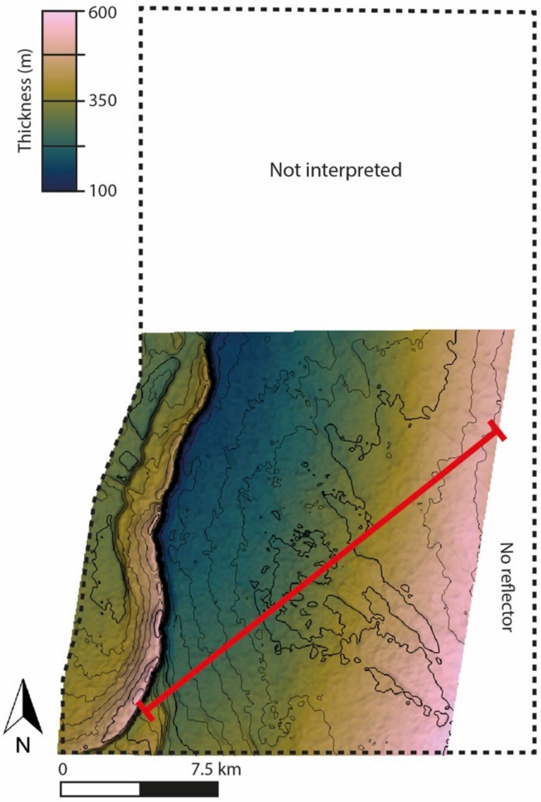

B) Seismic composite line

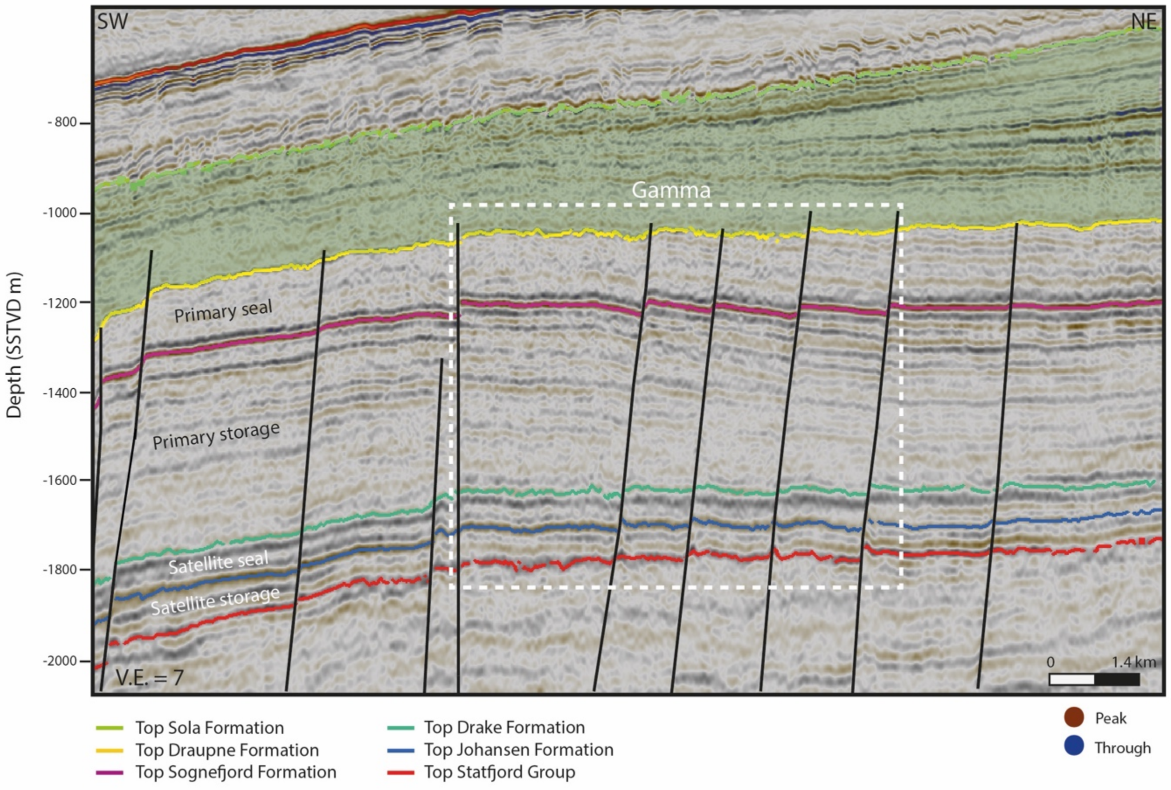

Figure 4.9. A) Thickness map of the secondary seal unit with 25-contour line spacing. B) Seismic composite line highlighting the Gamma structure and the secondary seal unit.

4.1.3 Structural description and fault populations

This subsection aims to give a structural characterization of the study area and the Gamma structure. First, interpretations of a seismic cross-section and variance attribute maps are presented to give a structural description, then descriptions of faults in the study area and within Gamma, and finally fault analysis.

Two groups of faults have been defined within the study area, inspired by Gabrielsen et al., (1984): 1) First-order faults that are basement involved, that is, faults that cut through basement rocks (i.e., thick-skinned faults), and 2) second-order faults which have no basement involvement (i.e., thin-skinned faults).

4.1.3.1 Structural description

Several normal faults are visible within the seismic composite line in Figure 4.3. The composite line intersects the Vette Fault Zone to the southwest and a segment of the Øygarden Fault Complex to the northeast marked as thick-skinned faults (Figure 4.3). Smaller faults are also interpreted in the composite line, which offset the Late Jurassic-Early Cretaceous Draupne Formation, the Late Jurassic Sognefjord Formation, and the Early Jurassic Drake and Johansen formations. Some faults are interpreted to cut through the Cretaceous Sola Formation and up to Paleogene and Neogene strata. These faults are not observed to penetrate the basement, making them thin-skinned faults (i.e., Gabrielsen et al., (1984)). The thin-skinned faults are also observed within the Gamma structure (Figure 4.3), offsetting the primary and satellite storage complexes. The faults appear to terminate within the underlying primary storage unit or just above the primary seal unit, showing small displacements (Figure 4.6C). The depth-structure maps (Figure 4.5A-E) show that the majority of faults within the study area have small displacements (no considerable variations in depth across the faults), the Vette Fault Zone which has a significant larger offset (Figure 4.5).

Variance attribute maps are presented in Figure 4.9 to aid the assessment of the structural framework and the spatial distribution of faults within the study area and the Gamma structure. The variance maps include the top Statfjord Group, Johansen, Drake, Sognefjord, Draupne, and Sola formations (Figure 4.10). The top Sola Formation was only interpreted in the southern half of the study area where the Gamma structure is located (Figure 4.10F). The surfaces are intersected by the Vette Fault Zone and several thin-skinned faults which are spread throughout the study area: The top Statfjord Group, Johansen, Drake, and Sognefjord formations exhibit similar geometries both in the entire study area and in Gamma (Figure 4.10A-D): As observed in the depth structure maps, the faults have a WNW strike in the northern and southeast, whereas the faults in the southwest have an N-W strike (Figure 5.10A-E).

In Gamma, the faults have predominately a N-W strike and extend vertically in the top Statfjord Group, Johansen, Drake, Sognefjord formations (Figure 4.10A-D). In the top Draupne Formation, faults are concentrated in the northwest, with strikes of WNW, and most of the faults observed in the underlying surfaces are not present in Gamma and the southern part of the study area (Figure 4.10E). In the western part of the study area, faults appear to form a relay ramp in the Vette Fault Zone (Figure 4.10D). The relay ramp is observed to extend vertically in the Statfjord Group, Johansen, Drake, Sognefjord, and Draupne formations (Figure 4.10A-E). The relay ramp appears to connect to segments of the Vette Fault Zone, making it a breached relay (i.e., subsection 3.1.1.1). This relay ramp has been researched in a previous publication (i.e., Mulrooney et al., 2020), which suggested that two segments of the VFZ became hard linked by this structure during Rift Phase 2, making it a breached relay.

The top Sola Formation is the only surface that is not intersected by the thin-skinned faults described herein: The surface appears to have densely spaced faults that make a polygonal pattern in map-view, and they are observed in both the hanging wall and footwall of the Vette Fault Zone (Figure 4.10F). These faults have been described in the northern Horda Platform in previous publications (e.g., Clausen et al., 1999, Mulrooney et al., 2020, and Wrona et al., 2017), named polygonal faults, suggested to be developed during the Eocene to middle Miocene.

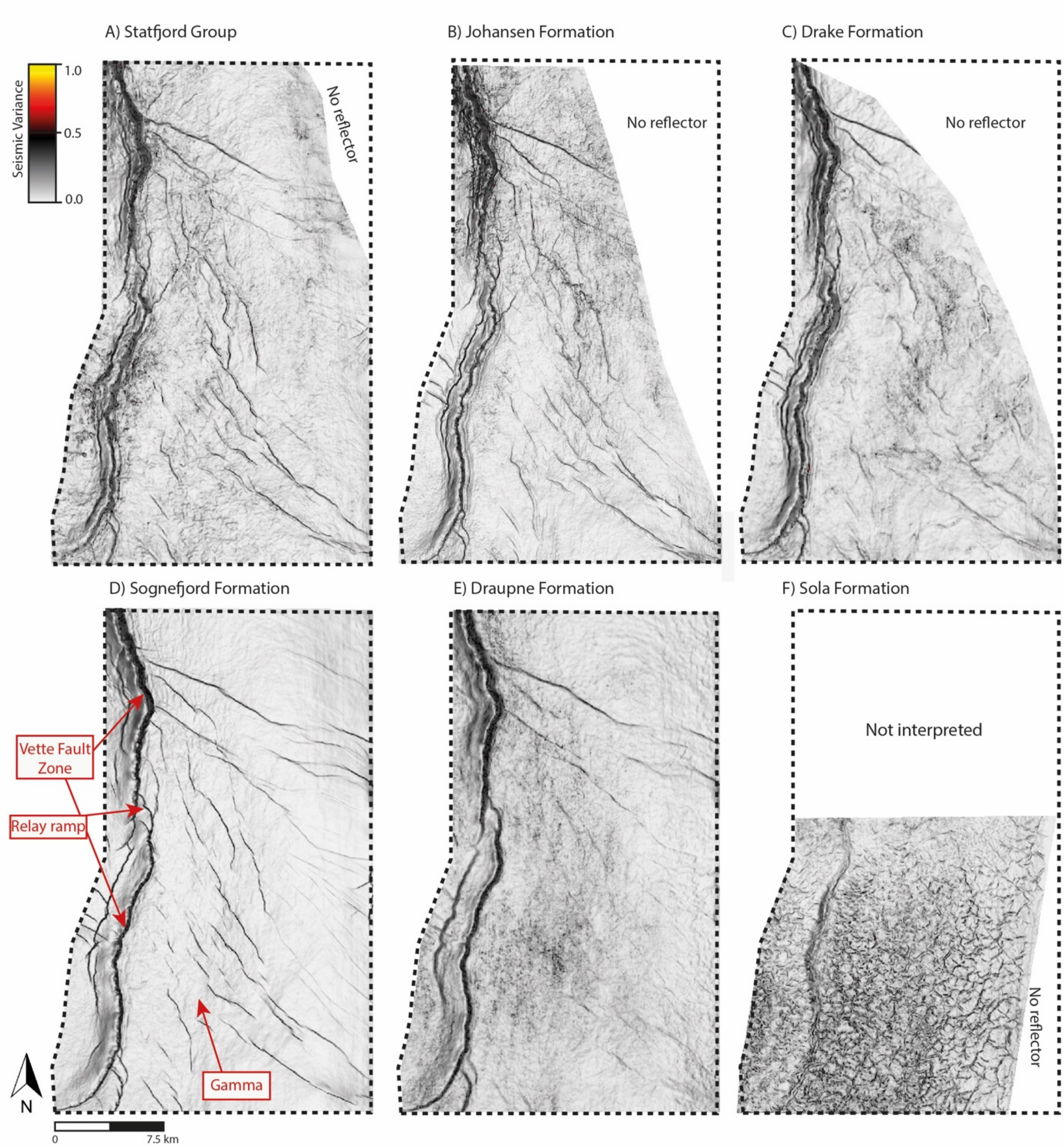

Figure 4.10. Seismic variance attribute maps for six of the horizons in the study area. All variance maps are flattened on the six interpreted surfaces in Figure… and are displayed from eldest to youngest. A) Statfjord Group. B) Johansen Formation top of (satellite storage). C) Drake Formation (top of satellite seal). D) Sognefjord Formation (top of primary storage). Gamma, VFZ, and the relay ramp within the VFZ are highlighted. E) Draupne Formation (top of primary seal). F) Sola Formation (top of secondary seal).

In total 35 faults were mapped in the study area (Figure 4.11). Figure 4.11 shows the study area in 3D, to give an overview of the structural framework around the Gamma closure in the top Sognefjord Formation.

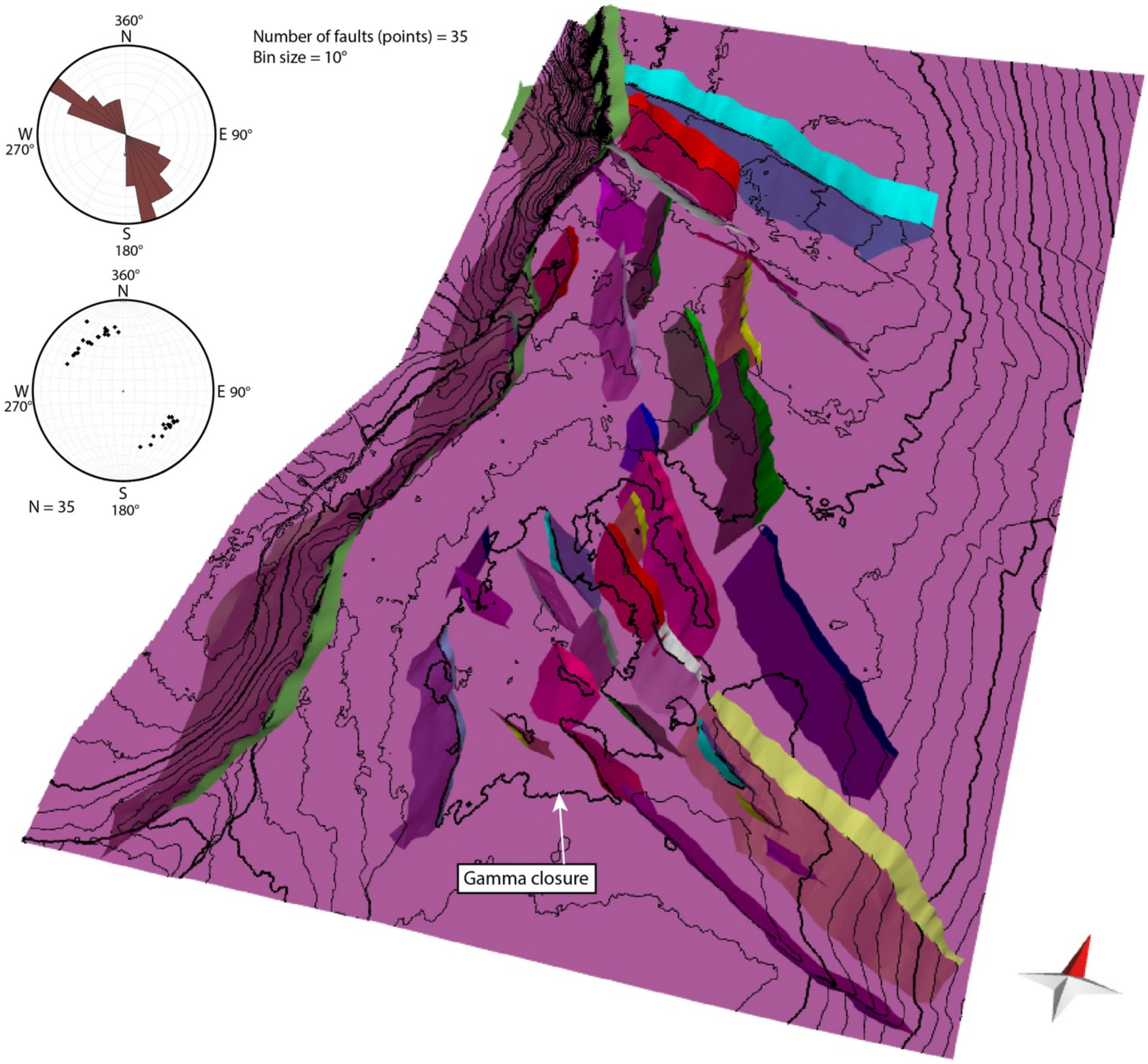

Figure 4.11. Overview of the study area with all mapped faults cutting through the top Sognefjord Formation (purple surface). V.E = 1.

4.1.3.2 First-order faults

In total, one fault within the study area is considered a first-order fault, the Vette Fault Zone, due to its influence on the basement (Figure 3.9). A second first-order fault is just outside the eastern edge of the seismic cube, the Øygarden Fault Complex, and because of this, this fault is not mapped in this study. The Vette Fault dips to the west and crosses in the entire study area and out of it to the north and south. The Vette Fault offsets Jurassic sediments by approximately 300 meters and is observed to terminate in the Cenozoic Hordaland Group in the study area. The mean strike of the Vette Fault is N-S (180°) and has a trace length of 32 km in the study area.

4.1.3.3 Second-order faults

34 faults within the study area are classified as second-order faults as they display no basement involvement. They are located between the Øygarden Fault Complex and the Vette Fault Zone, whereas 10 faults offset the crest of the Gamma closure (Figure 4.11 & 4.13). The second-order faults exhibit a maximum trace length of 8.6 km, with a mean strike of NW-SE (148°), which is oblique to the Vette Fault Zone. However, as discussed in subsection 4.1.3.1, variations of strikes can be observed in the study area. In contrast to regional thick-skinned faults such as the Vette Fault Zone, the second-order faults have no preferred dip direction: 14 antithetic faults dip to the northeast, and 20 synthetic faults dip to the southwest. The mean dip of the second-order faults is 56°.

The mean orientation of the faults within the Gamma structure is NW-SE (288°) and the mean dip of the faults within Gamma is 55° (Figure 4.13), consistent with the general trend across the entire study area. Similarly, the faults within Gamma have no preferred dip direction: 6 faults have a dip direction to the northeast, whereas 4 have a dip direction to the southwest (Figure 4.13).

Figure 4.12 shows the mapped faults with interpreted vertical extents together with inferred interaction styles. Time slice intersections in the variance volume were interpreted to assess the lateral and vertical extent of faults and their interaction style. Down-section, the second-order faults terminate in the Triassic successions while up-section the faults terminate within the Jurassic to Cretaceous successions. In Gamma, 9 faults are interpreted to intersect the Jurassic up-section, whereas 1 fault intersects the Cretaceous up-section (Figure 4.12B). The first-order Vette Fault Zone extent from the basement to the Cenozoic (Figure 4.12).

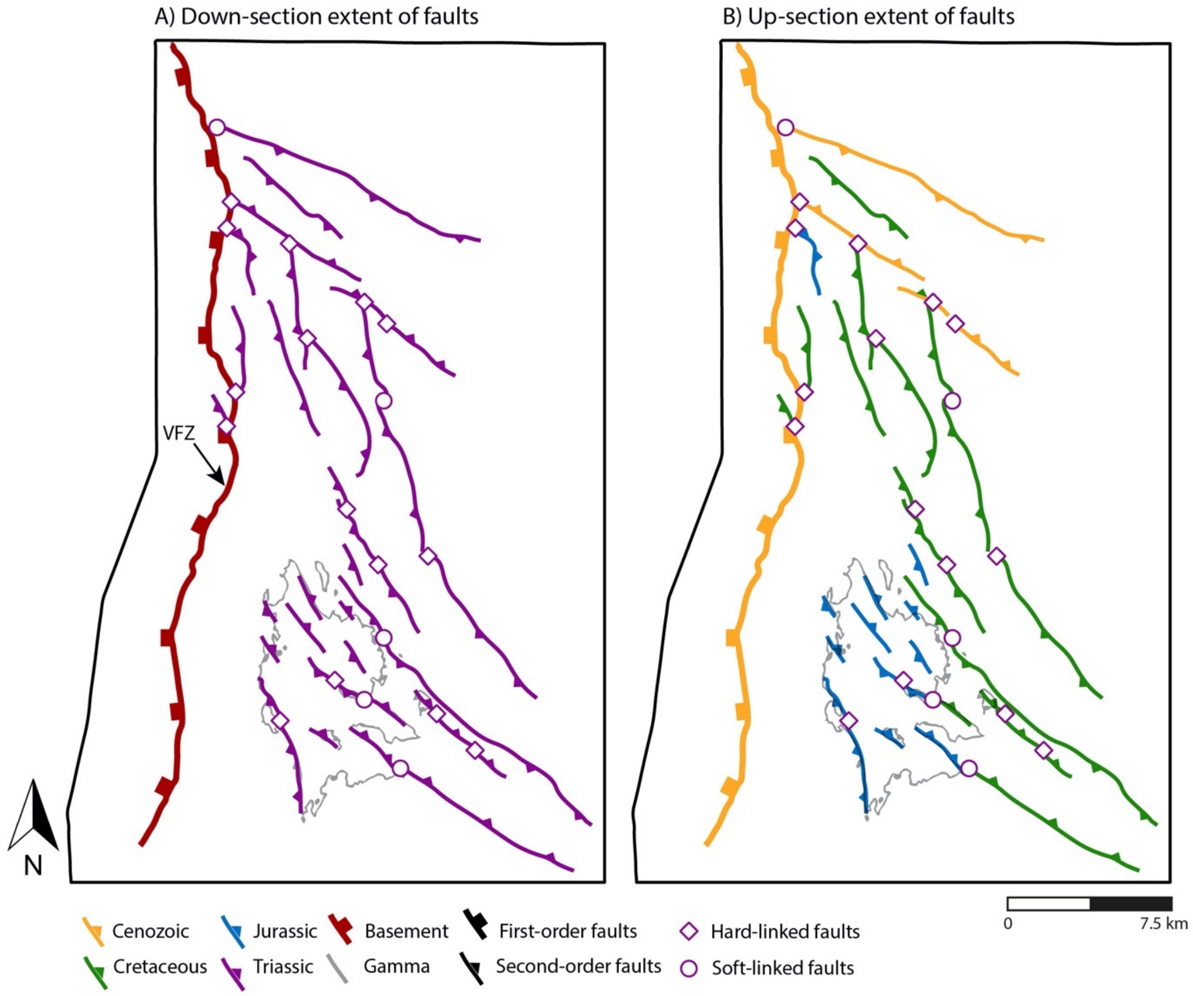

Figure 4.12. Maps of the study area showing mapped faults that intersect the top Sognefjord Formation. Color represents age of strata within which fault terminates; A) The down-section extent of faults with inferred fault interactions from the variance volume. B) The up-section extent of faults with the Gamma closure outlined.

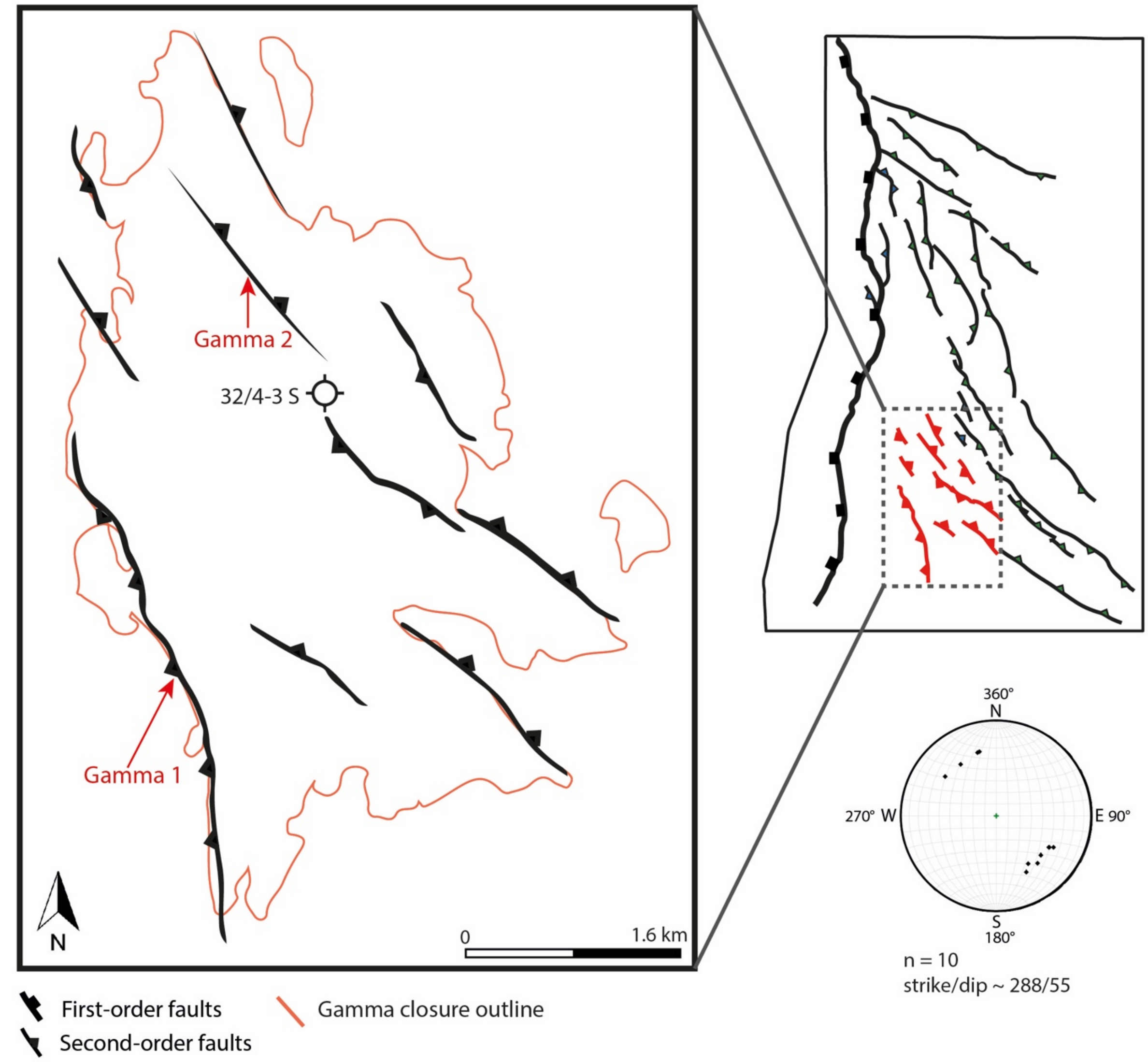

Figure 4.13. Map showing the faults within the Gamma structure. Faults are shown as heave polygons in the top Sognefjord Formation. The Gamma closure outline is a polygon from topographic contour lines in the top Sognefjord Formation.

4.1.4 Fault throw

Analyzing lateral variation of throw of a fault can give a more confident interpretation of fault interaction styles (Duffy et al., 2015). In addition, understanding fault evolution is important when addressing the implications for fluid migration, as lateral throw variations can be used to identify linkage points that may represent an increased risk of leakage, and assess what kind of fault seals may have developed. Furthermore, understanding fault evolution helps predict what kind of subseismic fracturing can be expected (Lohr et al., 2008). In the following subchapter, fault throw diagrams, maximum throw vs. length, and throw vs. length profiles are presented for two faults within the study area to assess spatial and temporal development. These faults are selected to represent several faults within the study area because they are within Gamma and have different dip directions: Gamma 1, which dips west-southwest, and Gamma 2 which dips northeast. In addition, all faults in the area have similar displacements: Observing the depth-structure maps (Figure 4.5A-E) together with the throw maxima plot in Figure 4.13, they give a proxy of the range of displacements of the faults within the study area and the Gamma structure. The displacements are low and lower than the thickness of all storage and seal units (Figure 4.7).

Of the mapped 34 faults, the highest throw value that can be observed is 58 m and most of the faults fall within the range of 14 – 50 m in maximum throw (Figure 4.14). The trace lengths of the faults are within the range of 1.2 – 8.6 km (Figure 4.14). In contrast to the expected linear relationship between maximum throw and fault length, that is, longer faults are expected to have a greater throws (i.e., propagating model) (Kim & Sanderson, 2005), the faults within the study area display a different relationship: The trace lengths vary, but no considerable change in throws are observed. For example, 5 of the faults have trace lengths of 2.4 – 8.6 km and have throws in the range of 46 – 58 m (Figure 4.14). An interpretation of this could be that the faults within the study area may have grown predominately in length in an early stage of their evolution before they died. This will be discussed further in subsection 5.2.2.1.

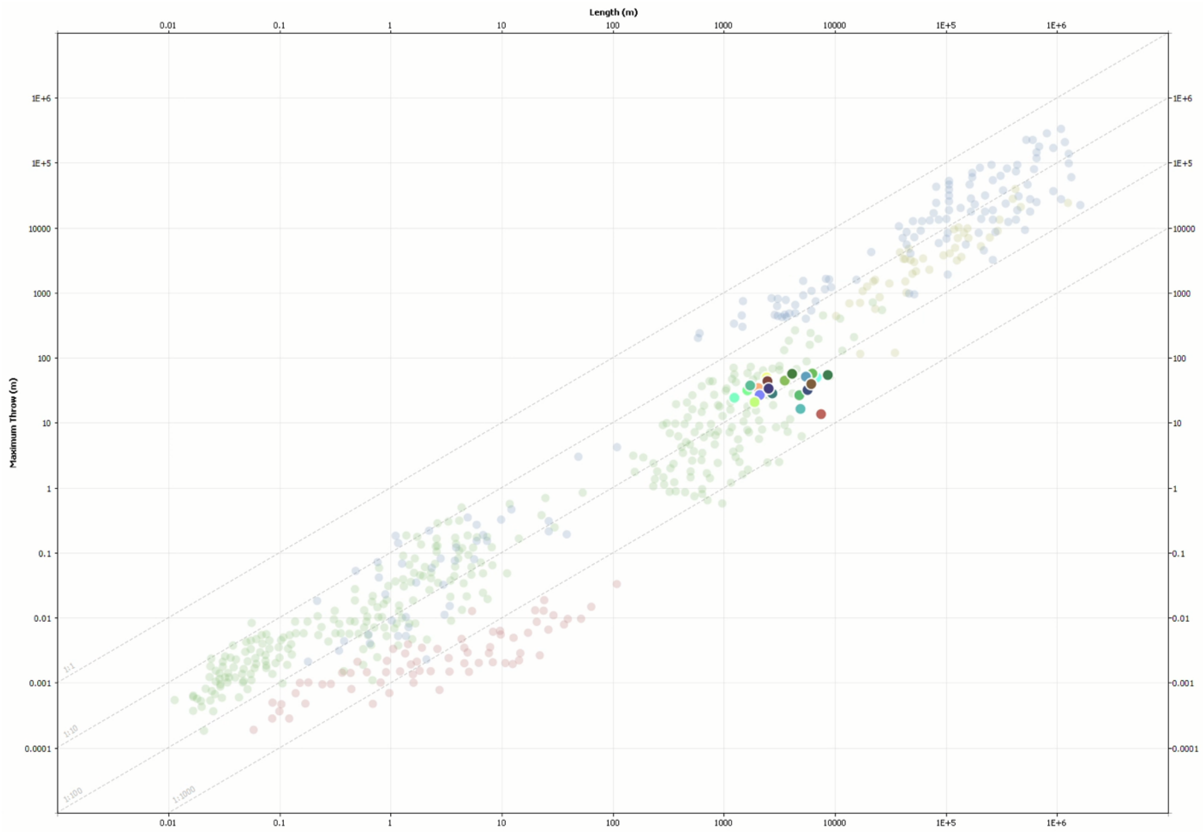

Figure 4.14. Maximum throw vs. length plot of 22 of the 36 faults within the study area. Global measurements of normal, thrust, strike-slip faults, and deformation bands are obtained from PETEX Move. Green plots are expected values for normal faults, yellow are thrust faults, blue a strike-slip faults, and red is deformation bands.

4.1.4.1 Lateral throw variations

Lateral variations in throw are shown in throw vs. length profiles together with a fault throw diagram for each fault in this subsection. As mentioned in subchapter 4.1.4, two faults were chosen to represent several faults in the study area, and as such, these faults are selected to perform fault throw analysis.

A fault throw diagram with cut-offs and a throw vs. length profile is presented in Figure 4.15 for the second-order fault Gamma 1. Gamma 1 is NW-SE striking (165°) and is approximately 6 km long laterally. The fault is isolated and does not interact with other faults in Gamma. In the fault throw diagram (Figure 4.15A), three throw maxima can be observed in the Sognefjord Formation, whereas six throw maxima can be observed in the Statfjord Group and Johansen Formation.

The throw vs. length profile in Figure 4.15B shows that the throws for each formation and group top decrease until they reach 0 meters at the fault tips. The overall lowest throw values can be observed in the Draupne and Drake formations, where the Draupne Formation has slightly higher values. The Johansen Formation displays higher throw values than the Draupne and Drake formations, with three throw maximums: One furthest to the NNW, and two in the middle of the fault. The Sognefjord Formation and Statfjord Group display the highest throw values, with the Sognefjord Formation having the overall highest throw values. The throw extrema correspond to the Sognefjord Formation (40 m), seen approximately 1.5 km from the north-northwestern part of the fault. For the Sognefjord Formation, four throw maximums can be observed in the profile, whereas six throw maximums can be observed for the Statfjord Group. The highest throw value in the Statfjord Group (39 m) is close to the throw peak observed in the Sognefjord Formation. It is important to note that the throw vs. length profile is erroneous for throws under or close to the vertical resolution (roughly 10 m) as throws will of this magnitude cannot be accurately resolved.

In summary, two ‘lines’ of throw maxima can be observed on Gamma 1 laterally, one line in the Late Jurassic Sognefjord Formation and one along the Late Triassic Statfjord Group to the Early Jurassic Johansen Formation (Figure 4.15A). This may indicate that two separate faults have nucleated vertically, making one fault, as areas of throw maxima can be interpreted as former individual fault segments (Kin & Sanderson, 2005). This will be discussed in section 5.1.2. Furthermore, four throw maxima can be observed in the Sognefjord Formation, indicating that several fault segments nucleated and linked laterally. The nature of linkage corresponds to the interpretation of hard-linkage of Gamma 1 (Figure 4.12), approximately 2.1 km from the north-northwestern part of the fault, where a throw minimum can be observed in the same area of the fault (Figure 4.14B). However, as mentioned, the vertical resolution of the seismic data provides uncertainty, and should be considered when assessing the evolution of Gamma 1.

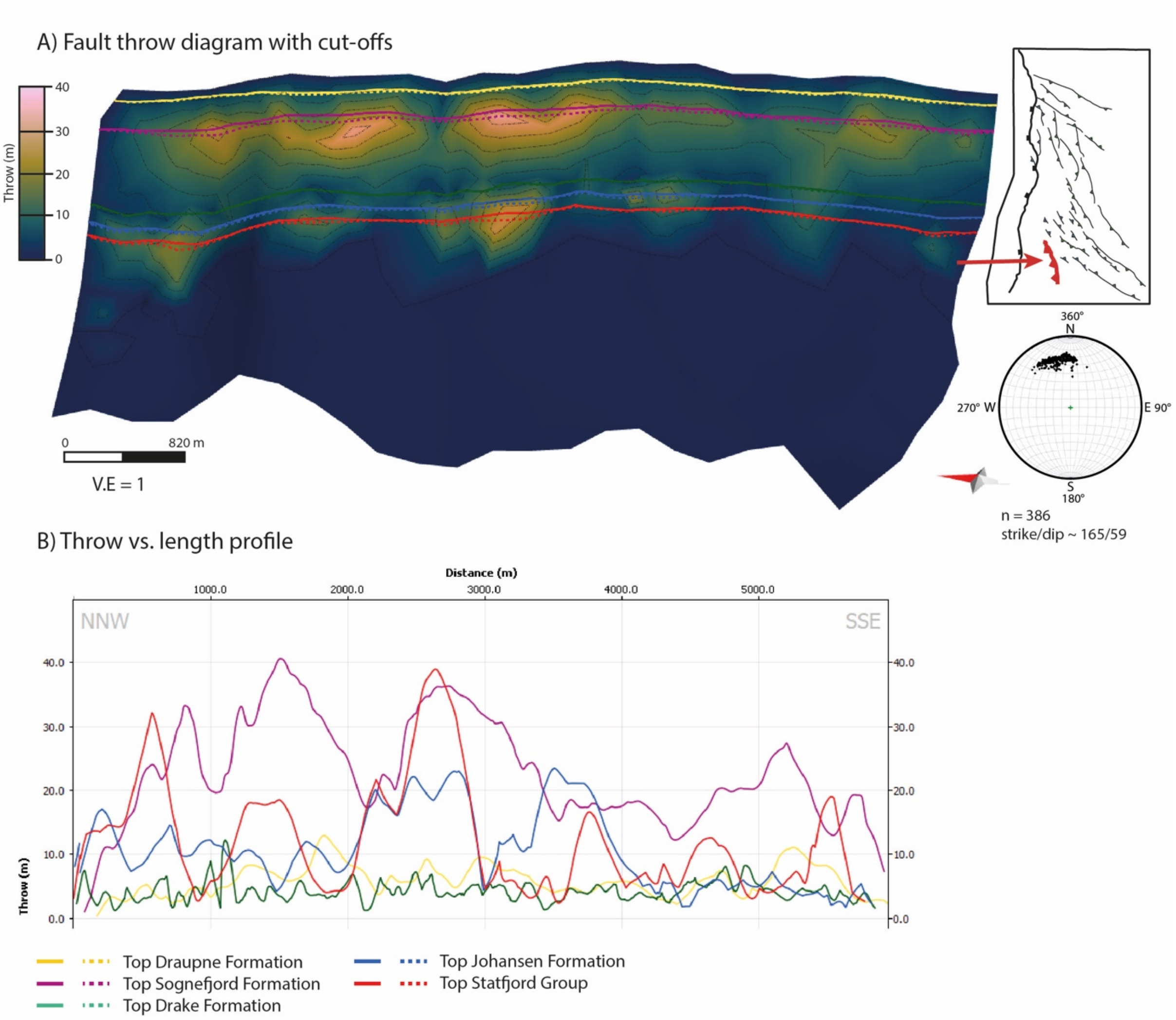

Figure 4.15. A) Gamma 1 fault throw diagram displaying cut-off lines and a 5-meter throw contour spacing. The stereonet shows the strike and dip variations for Gamma 1, with the fault surface being made of Delaunay triangles. The map shows the location of the fault within the study area, highlighted in red. B) Throw vs. length profile for Gamma 1. Note that a considerable portion of throws fall under the vertical resolution of the seismic data (8.75 – 17.5 m), making the cut-off lines not representative for vertical throw variations.

A fault throw diagram with cut-offs and a throw vs. length profile is presented in Figure 4.15 for the second-order fault Gamma 2. Gamma 2 is NW-SE striking (321°) and is approximately 3 km long laterally. In the fault throw diagram (Figure 4.15A), two throw maxima can be observed: One within the Sognefjord Formation and one within the Johansen and Statfjord formations. The throw vs. length profile in Figure 4.15B shows that the throws for each formation and group top decrease until they reach 0 meters at the fault tips. The overall lowest throws can be observed in the Draupne Formation, whereas the overall highest throws can be observed in the Sognefjord Formation, which has a throw maximum of 29 m, observed approximately 1 km from the southeastern part of the fault. Another throw maximum (17 m) can be observed in the Statfjord Group, approximately in the middle of the fault (Figure 4.15B).

In summary, the same throw distribution observed on Gamma 1 can be observed on Gamma 2: Two 'lines' of throw can be observed laterally at different depths: One within the Sognefjord Formation and one within the Johansen and Statfjord formations (Figure 4.15A). The throw distribution indicates that two faults nucleated vertically. As in the case with Gamma 1, the throw vs. length profile for Gamma 2 might have the same errors due to the throws falling under or near the vertical resolution of the seismic data (roughly 10 m). In the case of Gamma 2, this applies for all formations, as most of their throws falls under 10 m (Figure 4.15B).

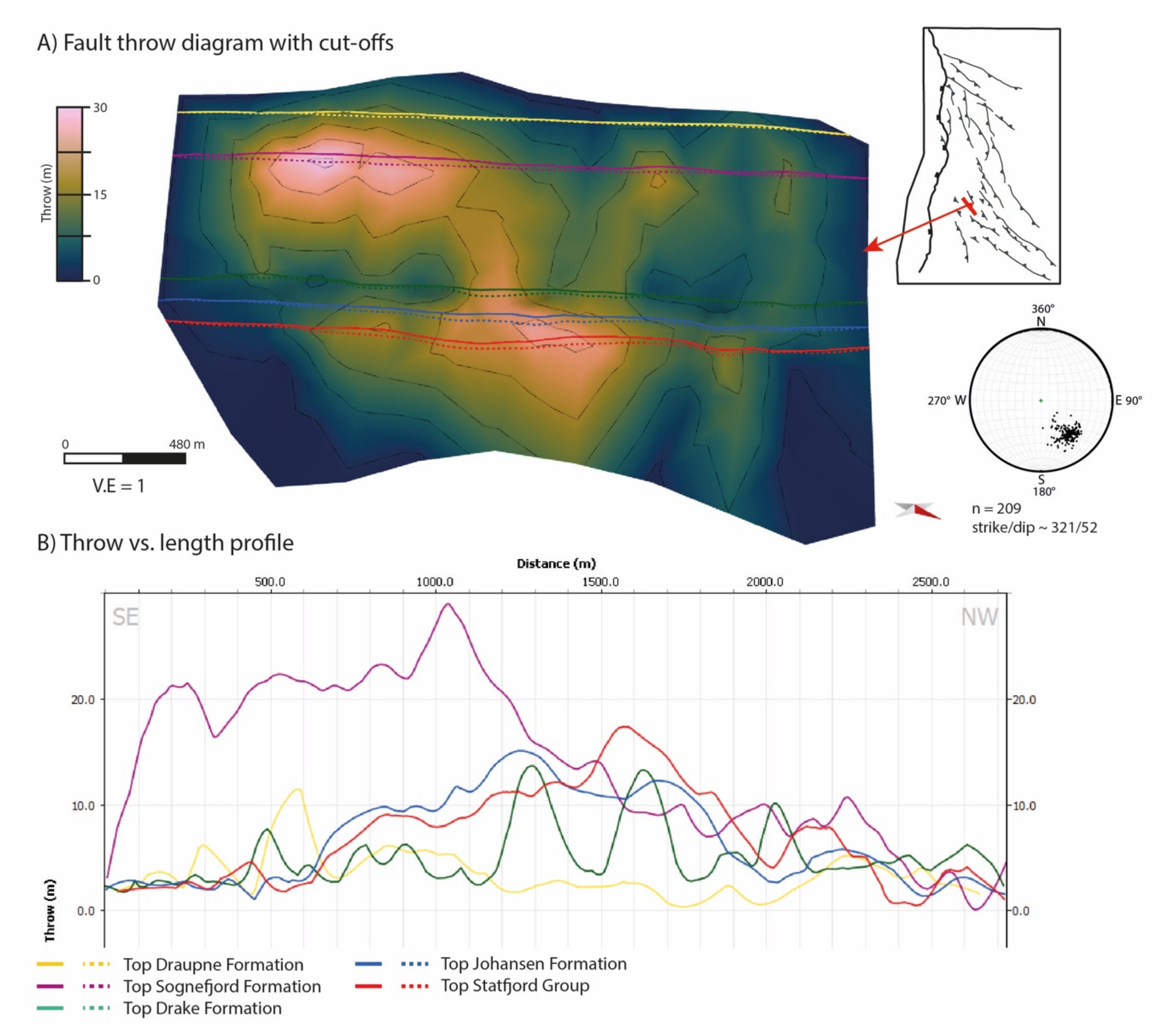

Figure 4.16. A) Gamma 2 fault throw diagram showing cut-off lines and a 5-meter throw contour spacing. The stereonet shows strike and dip variations for Gamma 2, with the fault surface being made of Delaunay triangles. The map shows the location of the fault within the study area, highlighted in red. B) Throw vs. length profile for

Gamma 2. Note that almost all throws fall under the vertical resolution of the seismic (ca.10 m), making the cut-off lines not representative of throw variations.

4.2 Across-fault seal assessment

Since all second-order faults within the study area have similar displacements which are lower than the thicknesses of the storage and seal units, only two faults were chosen for across-fault seal assessment to represent the faults within the study area. As in subsection 4.1.3.4, Gamma 1 and Gamma 2 are chosen.

Gamma 1 is presented in Figure 4.16A as an Allan diagram. The Allan diagram shows that the primary storage unit is mostly self-juxtaposed sandstone except for the uppermost part where sandstone in the footwall is juxtaposed with shale (i.e., the primary seal) in the hanging wall (Figure 4.16A). The satellite storage unit has a similar juxtaposition, where the satellite storage is sandstone on sandstone juxtaposition, except for the upper part where sandstone in the footwall is juxtaposed on shale (i.e., the satellite seal) in the hanging wall (Figure 4.16B). In both storage complexes, a uniform unit of shale-on-shale juxtaposition is present, making the cap rocks for both complexes. The same nature of juxtaposition can be observed for Gamma 2 (Figure 4.16B).

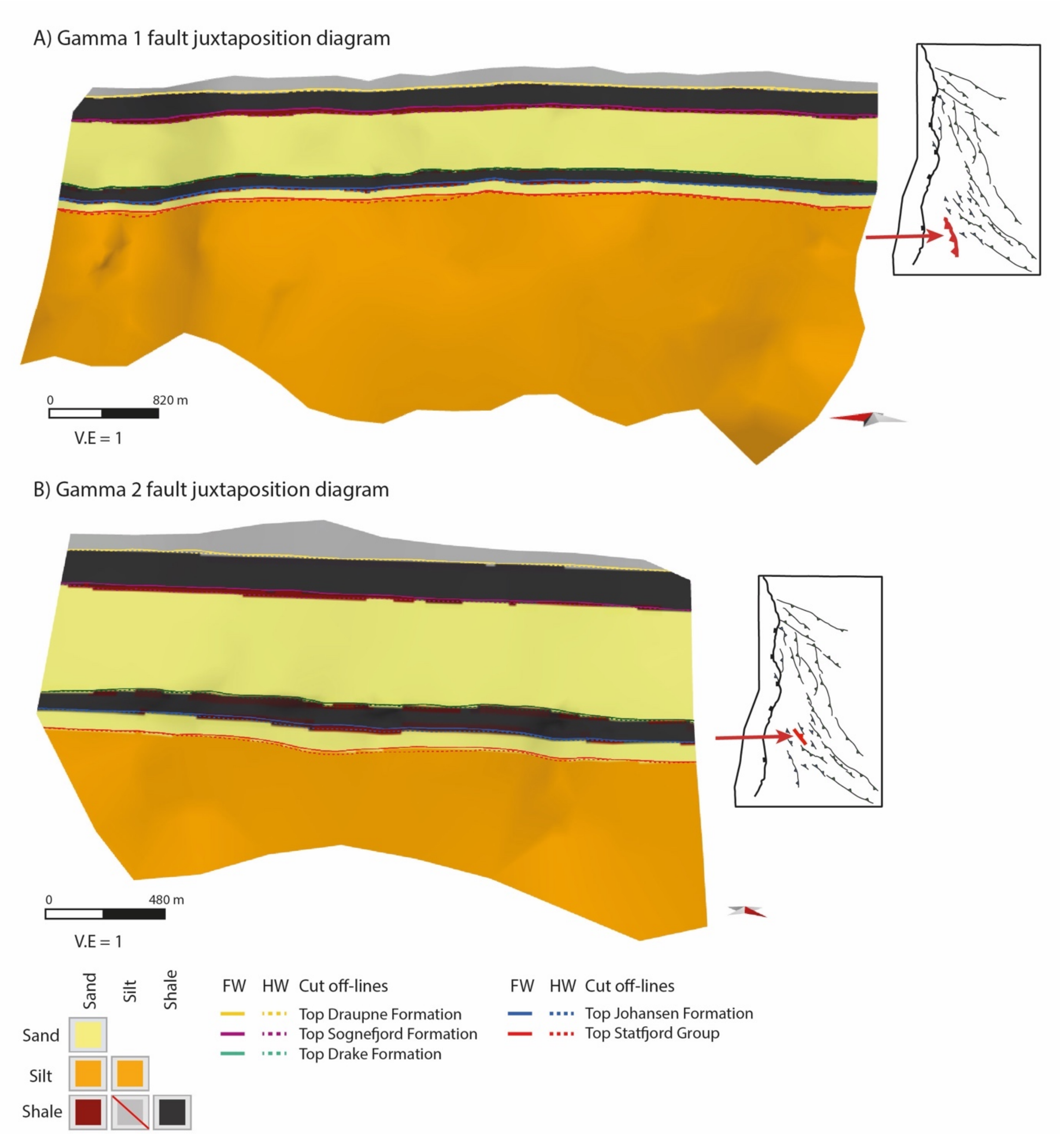

Figure 4.17. Allan diagrams with cut-off lines of A) Gamma 1 and B) Gamma 2. The maps show the location of the faults.

An overview of the nature of juxtaposition for all mapped second-order faults in the top Sognefjord Formation and top Johansen Formation is presented in Figure 4.17. These surfaces represent the interface between the storage units and seal units in the primary and satellite storage complexes. These particular surfaces are chosen because the topography of the seal, together with fault juxtapositions and inferred fault rocks is important when determining migration pathways in the subsurface (Weibull et al., 2010). The only juxtaposition scenario observed is sandstone on shale juxtaposition at the top Sognefjord and top Johansen formations (Figure 4.17). Considering that the faults and primary and satellite seals are at depths of approximately 1200 and 1700 m, respectively, the fault rock to be expected in the sandstone on shale juxtapositions is a clay smear, a low permeability fault rock, as the Draupne and Drake formations have been interpreted as shales due to their high gamma ray and density values, as well as high neutron porosity values, which may indicate a water bearing shale (Figure 4.2). Expected fault rocks in the study area will be discussed further in section 5.3.1.

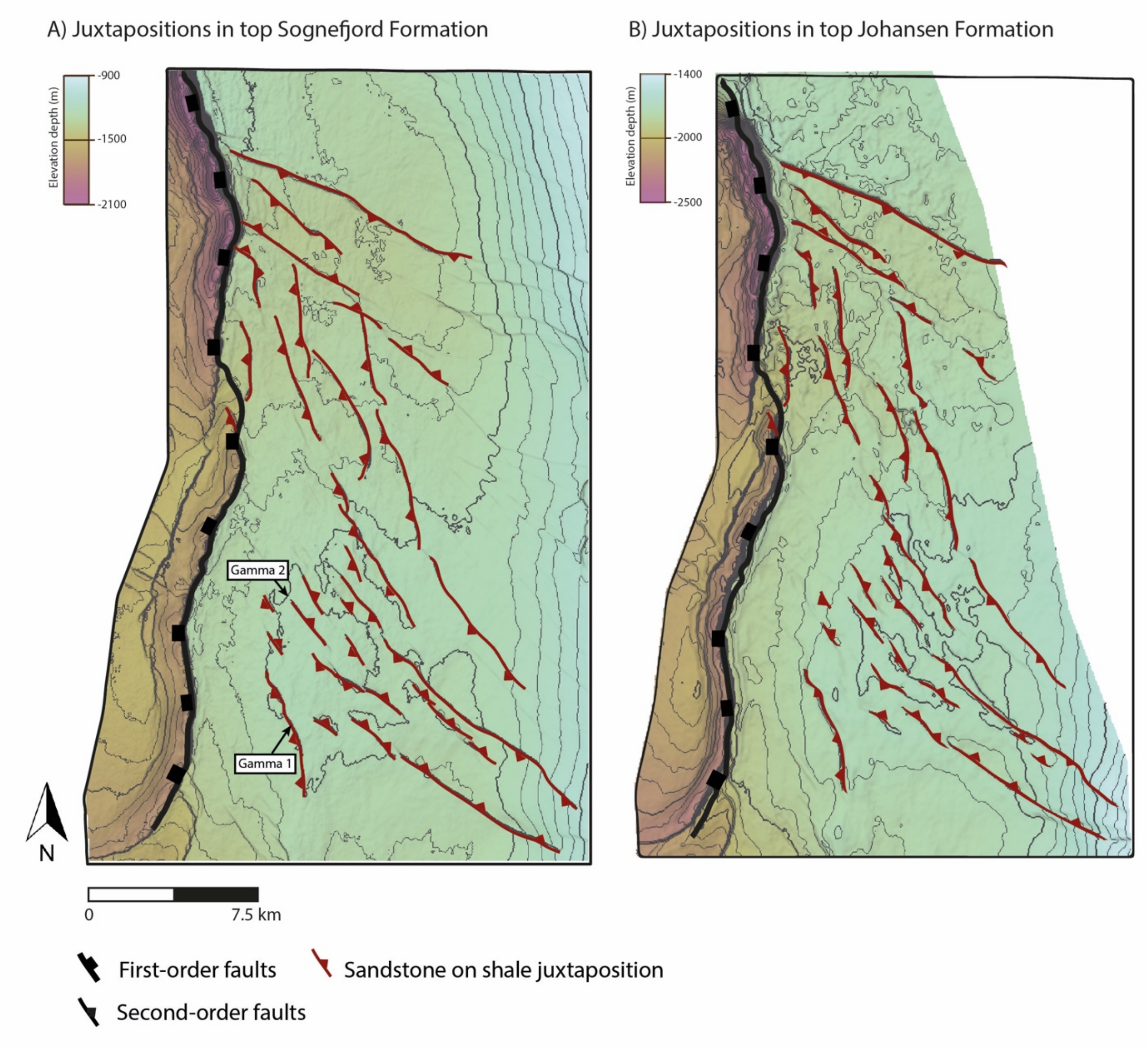

Figure 4.18. Maps showing the possible juxtaposition scenarios for the faults within the study area. A) Juxtapositions of faults in the top Sognefjord Formation. B) Juxtapositions of faults in the top Johansen Formation.

4.3 Volumetric analysis of closures

Several closures, making the Gamma prospect, appear as contour lines in the lower part of the study area in the top Johansen Formation (Figure 4.5B) and the top Sognefjord Formation (Figure 4.5D). The closures appear as closed contour lines where the surfaces dip down in all directions from the closures, making 4-way closures (Figure 4.5B & D). The depth of the closure in the top Sognefjord Formation is approximately 1.2 km and the depth for the closure in the top Johansen Formation is approximately 1.7 km. Faults intersect the closures, both within and at the edges of the topographic contour lines (Figure 4.5B & D). In total, four closures with different spilling points were mapped in this study, two of them being in the primary storage unit and two of them being in the satellite storage unit (Figure 4.19). Depth of closure spill points, bulk volumes, and estimation of storage capacities are provided in Table 4.2.

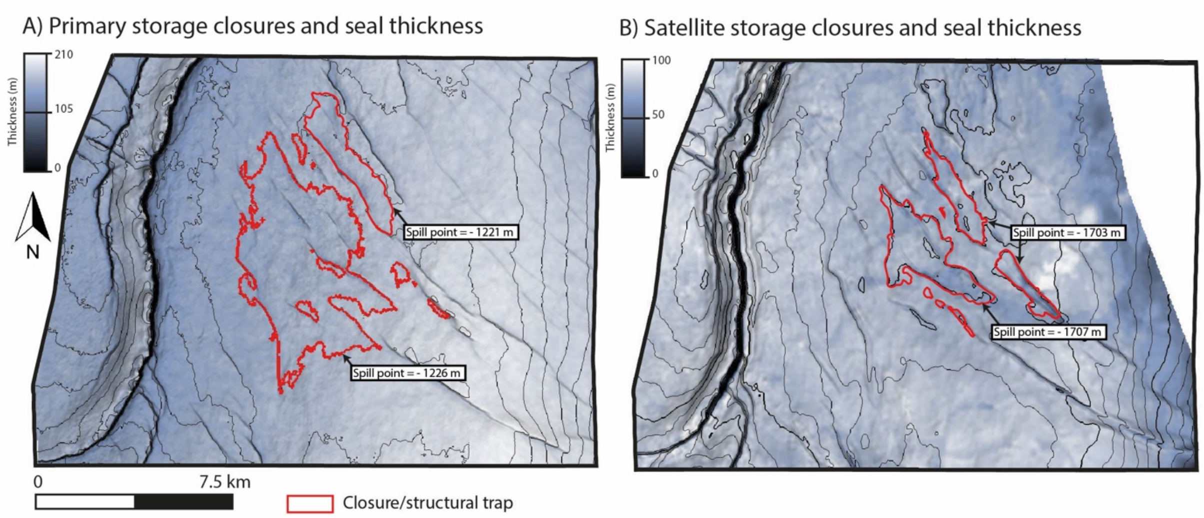

Figure 4.19. Structural traps (closures) within Gamma. Closure areas are shown as polygons overlaid on thickness maps. A) Closures with their spill points in the primary storage unit. Contour line spacing of thickness map of primary seal is 35 m. B) Closures with their spill points in the satellite storage unit. Contour line spacing of thickness of satellite seal is 31.

To estimate the Gamma structure's storage capacity, volumetric analysis was done on prospects in both storage units (subsection 3.3.3). As a reminder, to provide a rough estimate of the storage capacity of the closures herein, the methodology used in NPD CO_2 Storage Atlas is applied using values from the NPD CO_2 Storage Atlas and well 32/4-3 S.

The closures in the primary storage unit have a storage capacity of 4.32 Mt in sum, whereas the satellite storage unit has a storage capacity of 0.55 Mt in sum. In total, the Gamma structure has a storage capacity of 4.88 Mt, considering the storage complexes studied herein.

Table 4.2. Depth of closure spill points, bulk volumes, and estimations of storage capacities for closures mapped in the study area. Details around calculations of storage capacity are provided in subsection 3.3.3.

Stratigraphic unit	**Depth of closure spill point (SSTVD m)**	**Bulk volume (V_b m^3)**	**Estimation of storage capacity (M_{CO2} m^3)**
Sognefjord Fm	- 1221	$3.3 * 10^8$	4.01 Mt
Sognefjord Fm	- 1226	$2.6 * 10^7$	0.32 Mt
Johansen Fm	- 1707	$5.2 * 10^7$	0.33 Mt
Johansen Fm	- 1703	$3.5 * 10^7$	0.22 Mt

5 Discussion

In this chapter, the results of this study are used to discuss the structural evolution, storage aquifer and seal presence, structural traps, possible fault rocks, and possible CO_2 injection points and plausible migration pathways. Finally, limitations and uncertainties in this study are discussed.

5.1 Structural evolution

Numerous studies have described the structural evolution in the northern North Sea and the Horda Platform (Christiansson et al., 2000; Færseth, 1996; Ziegler, 1975), whereas a few studies have described it in Smeaheia (Mulrooney et al., 2020; Wu et al., 2021). The studies completed in the Smeaheia area are of particular interest, as the study area and Gamma are located here. These studies are the basis of comparison against the results in subchapter 4.1, which will be discussed in this subsection, with emphasis on fault timing and nucleation, lateral propagation, and interaction. Inspired by Wu et al. (2021), the fault timing results in the study area are divided into three main phases herein: 1) Synrift 1 faulting in the Permo-Triassic (Rift Phase 1); 2) Synrift 2 faulting in the Late Jurassic-Early Cretaceous; and 3) Post-Rift Phase 2 faulting and reactivation.

5.1.1 Timing and nucleation

The fault timing and nucleation analysis were based on identifying syn-rift/synkinematic growth strata in thickness maps (section 4.2.1), inspecting variance maps, depth-structure maps, and cross-cutting relationships in seismic sections (section 4.1.3).

5.1.1.1 Evolution of the first-order Vette Fault Zone

As presented in section 2.2.3, the rift architecture of the North Sea primarily evolved during the Late Permian to Early Triassic during an E-W oriented phase of extension (Rift Phase 1) (Duffy et al., 2015), which initiated the formation of predominately N-S striking, large displacement (3-5 km) faults that interacts with the basement (e.g., Øygarden Fault Complex, Vette, Tusse, and Svartalv Fault Zones) (Færseth, 1996; Whipp et al., 2014). A detailed structural study on the Vette Fault Zone is beyond the scope of this study, such as throw analysis and interpretation of Permo-Triassic sediments in seismic to assess growth strata, however, some observations were made: The mapped segment of the Vette Fault Zone falls within the category of Rift Phase 1 faults, as it is observed to interact with the basement, offset Jurassic sediments approximately 300 m, have a trace length of 32 km and have an N-S strike within the study area.

Minor thickness variations can be observed for the primary storage unit and the primary seal unit in the study area, with opposite trends: Thinning towards the west for the primary seal unit, northwards along the Vette Fault Zone, whereas thinning toward the east is observed for the primary storage unit (Figure 4.7). The thinning of the primary seal unit in the Smeaheia fault block has been interpreted to be a result of erosion due to footwall rebound (Mulrooney et al., 2020). However, the lack of apparent thickening of the Jurassic primary storage unit in the hanging wall of the Vette Fault Zone and that it thins towards the Øygarden Fault Zone (to the east) (Figure 4.7B), is anomalous as previous works describe these successions as syn-rift further west (Færseth, 1996; Bell et al., 2014; Whipp et al., 2014), but are the same as the results in Mulrooney et al. (2020). Mulrooney et al. (2020) suggested that this anomaly could be explained by the diachronous nature of rifting during Rift Phase 2, and the wedge-shaped strata in the Cretaceous observed in the hanging wall of the Vette Fault Zone (e.g., the Sola

Formation) (Figure 4.3 & Figure 4.4), may indicate movement on the VFZ occurred quite lite in this rift phase.

The majority of the mapped faults terminate up-section in the Cretaceous, whereas an approximately 3 – 4 km segment to the south terminates in the Cenozoic. This is in accordance with observations in Mulrooney et al. (2020). Mulrooney et al. (2020) suggested that the activity of VFZ continued into the Late Cretaceous, with a later pulse of reactivation during the Palaeocene and Eocene.

5.1.1.2 Evolution of second-order faults

As presented in section 2.2.4, a population of NW-SE striking, 2 – 10 km long faults were developed during the Late Jurassic to Early Cretaceous in the northern Horda Platform, where pre-existing faults were not preferentially orientated (Færseth, 1996; Mulrooney et al., 2020; Wu et al., 2021), deviating in strike from Permo-Triassic faults (N-S striking). These faults are smaller than the Permo-Triassic and basement-involved faults, have a closer spacing (0.5 – 5 km) and are thin-skinned (i.e., second-order) – meaning they only cut through post-Upper Jurassic sediments and not the basement rocks (Mulrooney et al., 2020). The mapped second-order faults within the study area show similar trends, having NW-SE strikes and trace lengths within the range of 1.2 – 8.6 km (Figure 4.14), terminating in the Late Jurassic Sognefjord Formation or the Late-Jurassic to Early Cretaceous Draupne Formation (i.e., primary seal unit) (Figure 4.12). Only 4 of the 34 second-order faults, located in the north in the study area, are observed to terminate in the Cenozoic (Figure 4.12).

These observations indicate a NE-SW extension direction in the Smeaheia area. Wu et al. (2021) and Mulrooney et al. (2020) suggest that second-order faults formed during Rift-Phase 2 (i.e., synrift 2 faults, Figure 5.1), whereas the 4 faults in the north reactivated and nucleated and terminated in Cenozoic sediments (Post-Rift Phase 2).

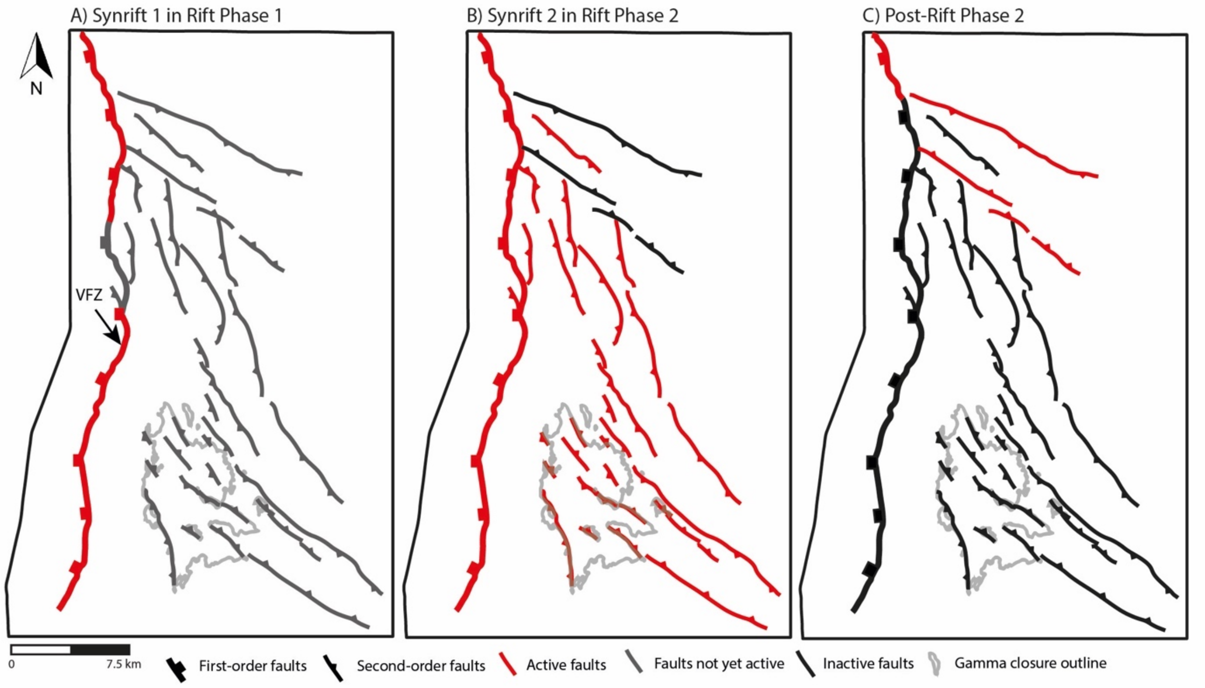

Figure 5.1. Schematic fault timing maps of the study area and Gamma in three tectonic phases based on growth-strata identification and cross-cutting relationships in seismic sections. The fault traces used here are based on the top Sognefjord Formation. A) Synrift 1 in Permo-Triassic (Rift Phase 1). B) Synrift 2 in Late Jurassic to Early Cretaceous (Rift Phase 2). C) Post-Rift Phase 2.

5.1.2 Fault throw and fault population

The maximum throw vs. length plots can be used to assess fault growth trends and validate the analysis of the modeled faults in this study (e.g., Kim & Sanderson, 2005). The results show that all mapped second-order faults within the study area have throw values less than 58 m (section 4.1.4) and that the maximum throw vs. length values fall within the range of normal fault populations, as they plot adjacent to the 1:100 line, with a spread from the 1:10 line to the 1:1000 line (Figure 4.14) (e.g., Kim & Sanderson, 2005). This trend is in accordance with recent measurements of maximum throw vs. length of second-order faults in the Smeaheia fault block (Wu et al., 2021).

In contrast to the expected linear relationship between maximum throw and fault length, that is, longer faults are expected to have greater throws (i.e., propagating fault model) (Kim & Sanderson, 2005), the mapped normal faults within the study area display a different relationship: The trace lengths vary (2.4 – 8.6 km), but no considerable change in throws are observed (46 – 58 m). As introduced in subsection 3.1.1.1, two fault growth models are commonly used, named the ‘propagating’ and ‘constant’ length fault models (Fossen & Rotevatn, 2016; Jackson et al., 2017; Nicol et al., 2005; Rotevatn et al., 2019; Walsh et al., 2002). Rotevatn et al. (2019) demonstrated by using throw-length data from a range of natural and experimentally re-produced faults, that both propagating (synchronous throw-length growth), and constant length (length-dominated followed by displacement-dominated growth) fault behaviors occur in nature. As to why the different models appear in different studies, Rotevatn et al. (2019) suggested that the studies describe kinematic behaviors associated with specific times in the evolution of a fault. For example, the propagating model, which is defined by tip propagation and segment linkage, characterizes the initial, rapid, and transient part of the lifespan of most fault, when fault growth is dominated by lengthening, whereas the constant length model characterizes the later part of the fault evolution when growth is dominated by displacement accrual (Rotevatn et al., 2019). Furthermore, the constant length model appears to be most applicable when a stage of length growth is followed by a stage of displacement accrual without further fault lengthening (Rotevatn et al., 2019). Rotevatn et al. (2019) suggest that normal faults are characterized by hybrid growth behaviors; first, a rapid stage of fault propagation, linkage, and lengthening, followed by a stage of constant length-displacement accrual. In. consideration of this, an explanation of why the faults in this study display varying trace lengths but similar throws, could be that in the early stage of the creation of these faults, they predominately grew in length and died before they could accumulate displacement, in accordance with the hybrid model suggested by Rotevatn et al. (2019).

The second-order Gamma 1 and Gamma 2 faults are representative of multiple NW-SE striking faults within the study area and Gamma, as all mapped faults display low throws and similar strikes. Both faults show two ‘lines’ of throw maxima along the faults, one in the Late Jurassic Sognefjord Formation and one along the Late Triassic Statfjord Group to the Early Jurassic Johansen Formation (Figure 4.15 & 4.16). For Gamma 1 and Gamma 2, this may indicate that two separate faults have nucleated vertically, making one fault, as areas of throw maxima can be interpreted to be former individual fault segments (Kim & Sanderson, 2005). These observations, however, are not conforming to other studies of throw distributions of second-order faults in Smeaheia, which suggest that most fault activity and growth occurred in the Late Jurassic to Early Cretaceous (e.g., Mulrooney et al., 2020; Wu et al., 2021), and further into the Paleocene and Eocene (e.g., Mulrooney et al., 2020). An explanation of the non-conforming throw distribution could be that most throws of Gamma 1 and Gamma 2 are close or falls within the vertical resolution (roughly 10 m), which adds uncertainty. Moreover, horizons were only interpreted in the upper section of the faults, resulting in an area with no data in the lower section of the faults; If lower horizons in the Triassic (lower than top Statfjord Group) were to be interpreted and added to the fault models, the throw distribution could be skewed and distributed differently.

5.2 Storage aquifer and seal presence

An overview of storage aquifers and top seal attributes for the primary and satellite storage complexes, as well as the secondary seal in the study area, is compiled in Table 5.1.

The formations that comprise the storage complexes in this study have been proposed to be suitable for CO_2 containment in this study. The target formations for CO_2 storage in the Gamma closure are the Upper Jurassic Sognefjord Formation (i.e., primary storage), the Upper Jurassic and Lower Cretaceous Draupne Formation (i.e., primary seal unit), the Lower Jurassic Johansen (i.e., satellite storage unit), Drake formations (i.e., satellite seal), and the Cretaceous Sola Formation (i.e., secondary seal unit) (Figure 4.3).

The primary storage unit consists of the Sognefjord formations and the Fensjord, Krossfjord, and Etive formations – as the top Drake Formation is established as the lower boundary of the primary storage unit. The primary storage unit is suggested to be a sandstone within Gamma in this study (section 4.1.4), as it has relativity low gamma ray and density readings in well 32/4-3 S, making it a suitable storage aquifer for CO_2. Other studies support this, as the Sognefjord Formation has been established as a shallow-marine sandstone (Vollset & Doré, 1984), and has been proposed to be a good candidate for CO_2 storage in Smeaheia due to its good reservoir properties (Fawad et al., 2021; Halland et al., 2011). Furthermore, the drilling results of well 32/4-3 S concluded that the Sognefjord Formation has very good to good reservoir quality (NPD, 2019). The primary seal unit, i.e., the Draupne Formation, is suggested to be a mudstone within Gamma in this study (section 4.1.4), as it has high gamma-ray readings, a high density, and high neutron porosity readings (water saturated) in well 32/4-3 S. The top Sognefjord Formations is the lower boundary for the Draupne Formation in the study area. Vollset & Doré states that the Draupne Formation is a marine, non-calcareous, carbonaceous, occasionally fissile claystone in the Horda Platform, with very high radioactivity (often above 100 API units), as observed in this study (Figure 4.2). The Draupne Formation overlies the

Sognefjord Formation in Smeaheia, having good sealing properties (Gabrielsen et al., 2020; Halland et al., 2011).

The deeper satellite storage unit, or the Johansen Formation, consists of shallow-marine sandstones with thin calcite cemented streaks (Vollset & Doré, 1984), and makes a candidate for CO_2 storage, due to its moderate to very good reservoir quality (NPD, 2019). The Drake Formation overlies the Johansen Formation and is a marine mudstone that consists of fissile, micaceous shale, and calcareous nodules (Vollset & Doré, 1984), thus making it a seal in the Lower Jurassic successions. In addition to the Jurassic and Cretaceous caprocks, a secondary seal is considered in this study since the overburden will likely contribute as a secondary seal in Smeaheia (Mulrooney et al., 2020). In this study, the top Sola Formation was chosen to be the top of the secondary caprock, due to its strong reflection within the study area.

5.2.1 Presence in Gamma and the study area

For the Lower Jurassic satellite storage complex, both satellite storage and seal units show predominately uniform thicknesses across the study area, having mean thicknesses of 75 m. However, both the satellite storage unit and satellite seal unit are not present in the entire study area (Figure 4.5B & C), being observed to pinch out in the northeast due to a divergent configuration of associated reflectors in the units. This interpretation of the Johansen Formation in the eastern Smeaheia fault block is consistent with those from Sundal et al., (2016) who proposed that the formation is absent here. The presence of the Upper Jurassic primary storage complex is much more certain throughout the study area: Both the primary storage unit and primary seal unit appear present in the entire study area (Figure 4.5D & E).

It is assumed that that the upper formations in the primary storage complex, the Fensjord, and Sognefjord formations are of good reservoir quality for CO_2 containment (Fawad et al., 2021; Holgate et al., 2013; NPD, 2019). Therefore, the CO_2 storage locations within the Upper Jurassic storage complex within the study area are not limited by the presence of aquifers, but by potential seals, such as the primary seal and the secondary seal. The mean thickness of the primary seal is 167 m within the study area, and at Gamma it has a thickness of 160 m. Furthermore, the secondary seal, or the overburden, has a mean thickness of 494 m. However, at the Gamma prospect, the secondary seal is 200 m, and it varies in thickness in the area where it is mapped, as it thickens toward the east and is truncated by an angular unconformity (Figure 4.3 & Figure 4.5F). Nevertheless, the thicknesses of the primary seal and the secondary seal are sufficient according to the NPD recommendations for CO_2 storage seals (>50 m) (Halland et al., 2011). This is also true for the satellite seal to an extent, as it has sufficient average thickness and thickness over Gamma but is observed to pinch out in the northeast.

Table 5.1. Summary of storage aquifers and seal attributes for the primary storage complex and satellite storage complex, as well as the secondary seal unit in the study area and Gamma.

	Primary storage unit	**Primary seal unit**	**Satellite storage unit**	**Satellite seal unit**	**Secondary seal unit**
Average thickness	416 m	167 m	75 m	75 m	494 m
Minimum thickness	320 m	120 m	40 m	40 m	100 m
Thickness at Gamma	430 m	160 m	70 m	80 m	200 m
Structural traps in Gamma	2	-	2	-	-
Total structural trap bulk volume	$3.6 * 10^8 m^3$	-	$8.7 * 10^7 m^3$	-	-
Total structural trap storage capacity	4.33 Mt	-	0.55 Mt	-	-

5.3 Migration pathways and possible injection points

The structural and stratigraphic architecture of the study area (subchapter 4.1) and faults and structural traps, provides a framework in which plausible CO_2 migration pathways can be inferred. As only one juxtaposition scenario is observed at the interfaces between proposed storage and seal units (shale on sandstone) (Figure 4.18), and only small fault throws are observed for the mapped faults (section 4.1.4), it would be relatively unfruitful to complete an SGR analysis of the faults in the study area. Instead, discussing and predicting the fault rock to be expected in the mapped faults will be done in section 5.4.1. Finally, structural traps and storage capacities, and plausible injection points and migration pathways will be discussed in sections 5.4.2 – 5.4.3.

5.3.1 Fault rocks in Gamma and the study area

In Smeaheia, Rift Phase 2 initiated during the deposition of the Draupne Formation and the Cromer Knoll Group (Whipp et al., 2014). Therefore, the burial depth of the second-order faults in the study area should be quite shallow at the time of faulting, suggested to be approximately 0.1 – 0.5 km (Wu et al., 2021). Thus, given a normal fault regime, the fault rocks to be expected in the sandstones (i.e., primary and satellite storage units) with low clay content, should be disaggregation bands. In such self-juxtaposed sandstones, the grain size and sorting of the fault rock do not change considerably during disaggregation, resulting in no significant change in permeability and porosity, which result in a low probability of sealing (0 – 30%) (e.g., Færseth et al., 2007). Furthermore, Wu et al. (2021) did an SGR analysis on intrablock (i.e., second-order faults) faults in Smeaheia, and found that faults with small throws (<50 m) have low SGR values (<15%), suggesting good communication across most intrablock faults. Therefore, across-fault migration may occur in the intervals of self-juxtaposed sandstone in the study area, and Gamma, acting as conduits. However, the influence of deformation bands on fluid flow is not clear; For example, Fisher & Knipe (2001) suggested that disaggregation bands in phyllosilicate-bearing sandstones reduce the permeability by 0 – 1 orders of magnitude compared to the host rock. It is also important to note that faults comprise heterogeneous damage zones, which could influence the fluid flow in the region ahead of the faults mapped in seismic (Fossen et al., 2007). These zones may not be mappable because of limitations related to resolution in seismic data. The presence of deformation bands could, therefore, act as both conduits and baffles in areas with self-juxtaposed sandstone or in areas not resolved in the seismic data.

The entire study area is covered by a sufficiently thick primary seal unit (>50 m, i.e., Halland et al., 2011), the Draupne Formation, which is interpreted to be a mudstone. Because the throws of the fault in the study are small, the primary seal unit is not offset considerably. Here, fault throws lower than the seal thickness is observed. A fault seal can be expected where the throw of a fault is lower than the seal thickness (Gassnova, 2012; Ingram et al., 1997). Furthermore, clay smear is also expected for shaly strata, such as the Draupne Formation and the Sola Formation (Figure 4.2), which is also the fault rock predicted in Wu et al. (2021).

As for the satellite storage complex, pressure measurements in well 32/4-3 S revealed close to hydrostatic pressure conditions, and that these measurements can be attributed to across-fault communication and vertical communication (Wu et al., 2021): Wu et al. (2021) suggest that the near-hydrostatic pressure from this interval is a result of the thick Drake Formation (i.e., satellite seal) acting as an effective vertical pressure barrier and limited across-fault communication (SGR >30%), and that the Drake Formation can also provide clay smear on the fault surfaces (Wu et al., 2021).

5.3.2 Structural traps and storage capacities

An overview of the structural traps within Gamma with bulk volumes and CO_2 storage capacitates is provided in Table 4.1. The total number of structural traps within the primary and satellite storage complexes is 4. These structural traps appear in the Gamma structure, highlighted in topographic contour lines in depth-structure maps (4.5B & D). All structural traps can be classified as 4-way-closures. The bulk volumes of these traps are $3.6 * 10^8$ m^3 and $8.7 * 10^7$ m^3, respectively. The storage capacities calculated are 4.33 Mt and 0.55 Mt respectively, in a total of 4.88 Mt for the entire Gamma structure.

As mentioned in section 1.1, 1.5 Mt CO_2 per year over 25 years will be injected in the first phase of the Northern Lights project (Equinor, 2019). The estimated storage capacities of the closures mapped herein (Table 5.1), therefore, represents 13% of the total CO_2 to be injected. This is a significant part of the planned CO_2 to be injected, however, as mentioned in section 1.1, the Northern Lights Project moved on from Smeaheia to Aurora as initial storage sites because Smeaheia was found to have unacceptably large uncertainties. Nevertheless, Smeaheia remains an important site for additional volumes of CO_2 because of its scale-up potential and location (Wu et al., 2021).

It is important to note that the storage capacity estimates calculated herein are rough estimates, as the parameters used to calculate storage capacities are considered for the entire Troll area for both Johansen and Sognefjord formations (Halland et al., 2011), and not within the Gamma prospect itself. Furthermore, the estimated bulk closure volumes are solely based on a fill-to-spill model, with the majority of the injected CO_2 accumulating at or near the crest if the structural traps. Moreover, this study did not consider other CO_2 trapping mechanisms, such as residual-, dissolution-, and mineral trapping, which may increase the volume of CO_2 that can be stored within the Gamma prospect. Also, storage capacity depends on other factors, primarily the reservoir pore volume, and the fracturing pressure, and it is important to know if there is communication between multiple reservoirs (Halland et al., 2011). For example, the possibility of cross-fault pressure communication between the Smeaheia fault block and the Tusse fault block (where the Troll East field is located) presents uncertainty (Lauritsen et al., 2018). In total, 6 paths have been observed that are related to relay ramp structures along the Vette Fault Zone, and given these potential pathways, communication with Troll is deemed more likely than not (Lauritsen et al., 2018). For example, the then newly drilled (October 2019) 32/4-3 S, provided valuable insights for predictions of the Smeaheia-Troll pressure communication; Wu et al. (2020) found evidence of depletion from the Viking Group sandstones in Smeaheia, which are the same group considered for CO_2 storage in the primary storage complex in this study. Moreover, the relay ramp in the Vette Fault Zone mapped herein was found to increase the risk of pressure communication between the fault blocks due to self-juxtaposed sandstones in the Viking Group (Mulrooney et al., 2020). Thus, depletion is possible within the Smeaheia fault block owing to over 20 years of hydrocarbon production from the Troll fields and this may have consequences for calculated storage capacities (Mulrooney et al., 2020; Wu et al., 2021). As mentioned in section 5.3.1, the near hydro-static pressure observed in the satellite storage complex promotes effective vertical pressure barrier and very limited across-fault communication (Wu et al., 2021), and as such, the storage capacities calculated for the closures within the top Johansen Formation are more certain.

5.3.3 Plausible injection points and migration pathways

Several closures, making the Gamma prospect, appear as contour lines in the north in the study area (Figure 4.5B & D). The closures appear as closed contour lines where the surfaces dip down in all directions from the closures, making 4-way closures (Figure 4.5B & D). The depth of the closures in the top Sognefjord Formation is approximately 1.2 km and the depth for the closures in the top Johansen Formation is approximately 1.7 km (Figure 4.19).

Both the top Sognefjord Formation and top Johansen Formation, each representing the interface between storage units and seal units, are useful surfaces to interpret in terms of plausible CO_2 migration pathways to the closures mapped herein, as the topography of the seal determines migration routes (Weibull et al., 2010). Thus, depth-structure maps and dip-azimuth maps of the top Sognefjord Formation and top Johansen Formation will be used to assess possible injection points and migration pathways. In summary, approximately along the middle of the study area, the surface dips predominately to the northeast, highlighting a possible migration pathway into the closures, both in the top Sognefjord Formation and top Johansen Formation (Figure 4.6).

The precise flow path into and migration within the Smeaheia fault block is not known. In this analysis, based on the considerations discussed herein, it is assumed that:

1) It is assumed that the CO_2 is mobile, and other trapping mechanisms such as residual-, dissolution-, and mineral trapping are not present. The inferred migration pathways are solely based on a fill-to-spill model, with the majority of the injected CO_2 accumulating at or near the crest of the structural traps.

2) The injected CO_2 would migrate northeast if the CO_2 would be injected in the southwest within the primary and satellite storage units, migrating up-dip at the interface between seal and storage unit for both storage complexes (primary and satellite).

3) The injected CO_2 would migrate southeast if the CO_2 would be injected in the northwest within the primary and satellite storage units, migrating up-dip at the interface between seal and storage unit for both storage complexes (primary and satellite).

4) The second-order faults promote across-fault leakage in areas of self-juxtaposed sandstones in the primary storage complex (discussed in section 5.3.1).

5) The second-order faults act as baffles in the satellite storage complex, due to limited across-fault communication (discussed in section 5.3.1).

Thus, the proposed CO_2 injection points lie to the southeast to the relay ramp in the Vette Fault Zone and in the southwest in the study area (Figure 5.2). At the top Sognefjord Formation, one possible injection point (1) is suggested, in the southwest of the study area (Figure 5.2A). Furthermore, migration pathways from injection point 1 and migration pathways after spill scenarios are suggested (Figure 5.2A). If the CO_2 would be injected into injection point 1, it would migrate up-dip towards the northeast: The CO_2 would migrate across Gamma 1, as the self-juxtaposed sandstones are present here (across-fault migration) until it reaches the Gamma closure. If the column height would reach the height of the estimated closure (maximum 29 m), it would spill into the adjacent closure and further up-dip, through faults that dip southwest (self-juxtaposed sand) toward the Øygarden Fault Complex.

Different injection points are suggested for the top Johansen Formation, 3 and 4, in the northeast of the study area (Figure 5.2B), as the satellite storage complex may have faults that promote limited across-fault communication, and thus act as baffles. If the CO_2 would be injected into injection point 2, the CO_2 would migrate up-dip until it reaches the closure (Figure 5.2B). If the column height would reach the height of the estimated closure (maximum 19 m), it would spill and migrate towards southeast, along faults as they may act as baffles, until it finally reaches the Øygarden Fault Complex (Figure 5.2B). The same scenario would happen if the CO_2 would be injected into injection point 3 (Figure 5.2B). In summary, if the column heights of the CO_2 would reach the height of the closures, the CO_2 would spill and migrate up-dip towards the Øygarden Fault Complex.

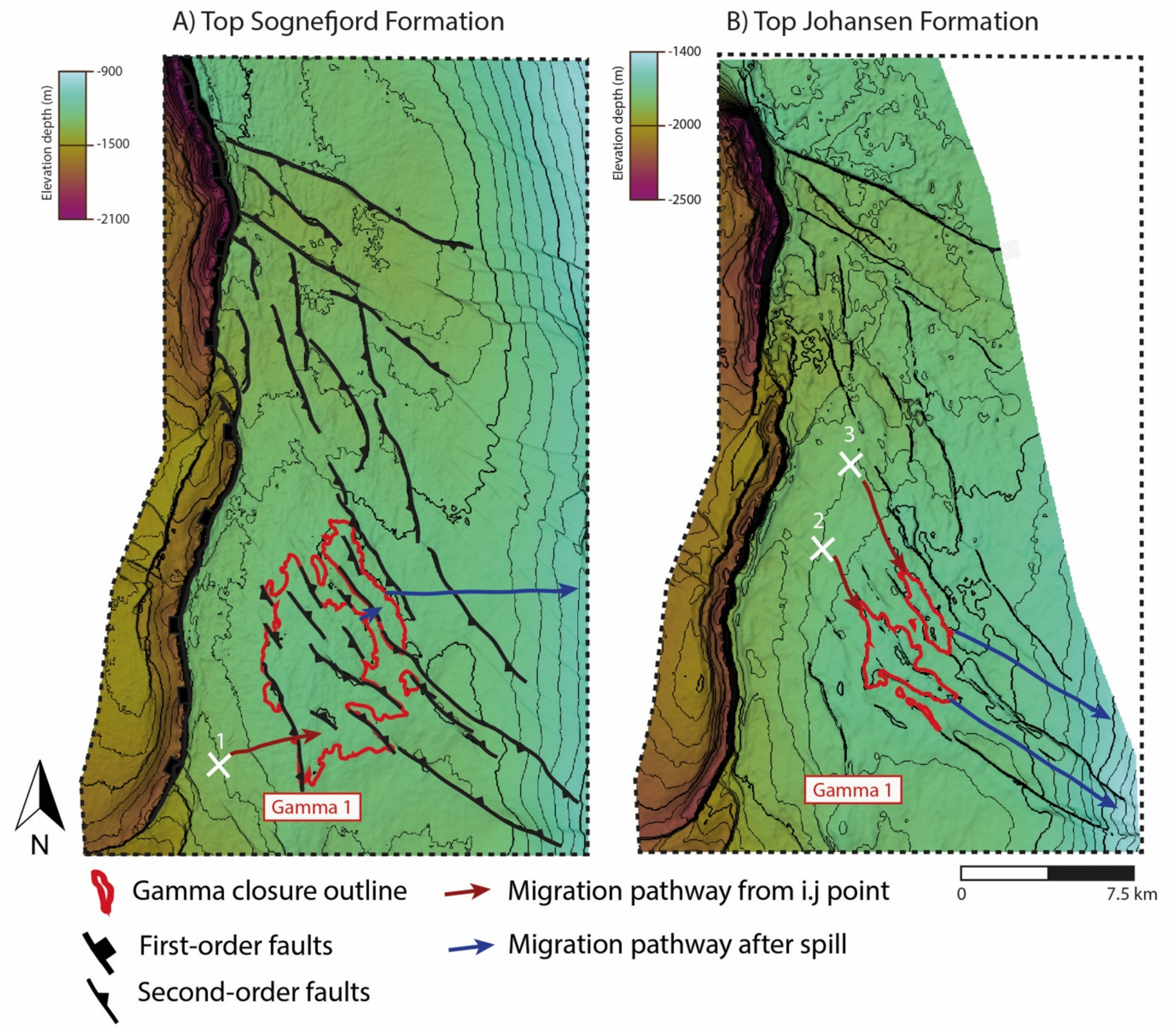

Figure 5.2. Depth-structure maps showing potential migration pathways at the A) top Sognefjord Formation (primary seal topography), 25 m contour spacing, and B) top Johansen Formation, 31 m contour spacing (satellite seal topography). Note that the gamma closure outlines represent different spilling points (see Figure 4.19) and dip directions of faults are only showed in the top Sognefjord Formation. White crosses represent possible injection points (i.j point).

5.4 Limitations

Analysis of the subsurface comes with many uncertainties and limitations. In this subchapter, limitations, and uncertainties related to seismic interpretation in the subsurface and fault throw analysis, the interpreted geomodel, and migration pathways are discussed.

5.4.1 Size of the study area

Limitations related to the interpreted geomodel within this study include the size of the study area and fault throws close to the vertical resolution. Fault throws close to the vertical resolution are discussed in section 5.6.2. Therefore, this section will discuss limitations related to the size of the study area.

The study area in this study covers a small area of the Horda Platform, and not the entire Smeaheia fault block (Figure 1.1 & Figure 3.8). It is therefore challenging to determine the structural evolution based solely on observations within the study area in this study. Comparison with previous studies on the structural evolution within the Smeaheia fault block (Mulrooney et al., 2020; Wu et al., 2021) was, therefore, necessary to support the interpretations in this study.

5.4.2 Seismic interpretation in the subsurface

Analysis of the subsurface has its uncertainties and limitations as the accuracy when interpreting seismic data depends heavily on the seismic resolution, but also human biases and errors during manual interpretation (Faleide et al., 2021). These uncertainties will follow through when creating geomodels of the subsurface and the subsequent analysis. In this section, these uncertainties will be addressed. Uncertainties related to interpreting seismic data can be divided into objective and subjective uncertainties (Faleide et al., 2021). Objective uncertainties are related to the seismic data itself, for example, the vertical resolution within stratigraphic units of interest. Subjective uncertainties are related to human bias and errors when interpreting seismic data, for example, the interpretation of faults.

Faleide et al. (2021) explored the challenges and pitfalls related to interpreting faults seismic data: 20 interpreters with different geoscientific backgrounds interpreted faults in modern conventional seismic data (dominant frequency 40 Hz). Faleide et al. (2021) revealed that there were considerable variations between manually picked faults and that identifying the location of fault tips was challenging for the interpreters. Therefore, this may also be the case in this study, as the faults were manually picked. It has also been shown that significant uncertainties occur through varying methodologies when interpreting faults in seismic data (Cunningham et al., 2021; Michie et al., 2021). For example, the line spacing (increments) chosen to pick fault segments will influence the analyses performed on the faults; wider line spacing may underestimate fault segmentation and cause inaccurate interpretation of the location of fault segments, predict higher SGR values, smooths the fault that subtle variations in strike and dip are lost, and lastly, it can result in predicting a more stable fault (Michie et al., 2021). In an attempt to provide an adequate fault interpretation, the faults in this study were interpreted with increments of 100 – 113 m, close to the suggested spacing of 100 m by Cunningham et al., (2020) and Michie et al. (2021). However, due to the limits of the vertical resolution of the NVG-HORDA-TAMPE seismic cube, together with throws close to the vertical resolution of the mapped second-order faults, there are high uncertainties related to the calculated throws and Allan diagrams in this study.

The vertical resolution is approximately 5 – 10 m within the Jurassic successions in the NVG-HORDA-TAMPE seismic cube. Fault throws less than 5 – 10 m will therefore not be visible within the seismic cube. Furthermore, throws close to the vertical resolution may produce noise in the fault model. For example, horizons interpreted alongside faults with throws close to the vertical resolution may add noise as the offsets displayed by the horizons are barely visible in the seismic image. The noise will be mirrored in the horizons imported into the geomodelling software and further produce erroneous cut-off lines in the fault modeling. These errors will follow through into fault analysis (subsection 3.3.2.3), for example throw analysis or assessment of juxtaposition seals to determine structural traps and their effect on CO_2 migration, as these methods depend heavily on the modeling of cut-off lines. Therefore, it is important to try to preserve the level of detail around the fault planes in the horizons, thus the feasibility of the cut-off lines, when importing them into the geomodelling software, as attempted in this study (subsection 3.3.2.2). However, as the majority of the mapped faults have low throw values in this study, many of them falling close to or within the limits of the vertical resolution, as demonstrated with Gamma 1 and Gamma 2. Therefore, the throws falling under or near the range of vertical resolution should not be considered when assessing fault evolution and interaction. Therefore, it is necessary to improve methods used to interpret faults with throws close to the vertical resolution of the seismic data, thus reducing the uncertainties related to throw analysis and across-fault migration.

6 Conclusions

In order to maximize the CO_2 storage scale-up potential of the Smeaheia fault block, a structural analysis of the Gamma closure has been conducted herein. As a reminder, the main objectives in this study are to i) generate a high-resolution 3D geomodel of the Gamma structure from seismic interpretation, ii) to discern if trapping structures and continuous caprock are present in the Jurassic intervals, iii) to discern the volumetric capacity of the proposed storage formation, and iv), discuss possible CO_2 injection points and migration pathways.

Objective i) was met by creating a high-resolution 3D geomodel of Gamma and the study area, using the CGG NVG 3D seismic survey, 2D seismic lines, and well data. Objective ii) was achieved by examining depth-structure maps, thickness maps, and fault geometries. The key observations from the results from these objectives are:

- Thickness maps of the primary storage complex show that it is present throughout the entire Gamma structure and study area with little signs of thinning. The average thickness of the primary storage unit is 416 m, whereas the average thickness of the primary seal unit is 167 m with a minimum thickness of 120 m, making it an adequate seal according to NPD (>50 m). The satellite storage complex is not present in the northeast of the study area but are present over the Gamma structure. The average thickness of the satellite storage and seal units are 75 m.

- The study area and Gamma consist of two fault populations: A first-order fault (VFZ) which interact with the basement and strikes N-S (180°), dipping west. Second-order faults exhibit minor variations in strike, NW-SE to WNW-ESE, with an average strike of 148°. The second-order faults have trace lengths in the range of 1.2 – 8.6 km and maximum throws in the range of 14 – 50 m. Furthermore, they show no preferred dip direction and are predominately restricted to Late Triassic to Early Cretaceous sediments.

- Second-order NW-SE striking faults within Gamma likely formed during the Late Jurassic to Early Cretaceous (Rift Phase 2), in accordance with previous studies in Smeaheia. The faults may have grown predominately in length and died before they could accumulate throws.

- There are uncertainties, however, with the geomodel, as mapped second-order faults display low throws, close to or within the limits of the vertical resolution of the CGG NVG seismic survey. Therefore, there are high uncertainties related to the calculated throws and Allan diagrams in this study.

Objectives iii) and iv) were met by calculating gross rock volumes and storage capacities of mapped closures and the presence of across-fault juxtaposition seals and membrane seals. Data from well 32/4-3 S (October 2019) add increased well control within the Smeaheia fault block. Results from Wu et al. (2021) are compared and used to infer migration pathways to closures. The key observations and results from objectives iii) and iv) are:

- Juxtaposition and throw analysis show that second-order faults have throws that are smaller than the primary seal (<167 m) and satellite seal (<75 m).

- Four structural traps (4-way-closures), two in the primary storage unit and two in the satellite storage unit are present in Gamma. The bulk volumes of these traps are $3.6 * 10^8$ m^3 and $8.7 * 10^7$ m^3, respectively. The storage capacities calculated are 4.33 Mt and 0.55 Mt respectively, in a total of 4.88 Mt for the entire Gamma structure. However, uncertainties are associated with the calculated storage capacity for the closures in the primary storage complex, as previous studies postulate that there is pressure-communication between the Smeaheia fault block and Tusse fault block through relay ramps, due to 20 years of hydrocarbon production in the Troll Field.

- Self-juxtaposed sands are observed in the primary storage unit, with possible disaggregation bands, which may promote across-fault migration. As for the satellite storage complex, clay smear may be present in the self-juxtaposed sandstones, as the satellite seal unit (i.e., the Drake Formation) is a shale (high API-values and density-values). Furthermore, previous studies have suggested the same fault rock here and that there is limited across-fault communication, resulting in baffles or barriers.

- Proposed CO_2 injection points lie to the southwest of the relay ramp in the Vette Fault Zone and southwest in the study area. In a fill-to-spill scenario, buoyant CO_2 is likely to accumulate within the structural traps in Gamma, improving the storage capacity in the Smeaheia fault block. If the column heights of the CO_2 would reach the height of the closures, the CO_2 would spill and migrate up-dip towards the Øygarden Fault Complex to the west.

References

Allan, U. S. (1989). Model for hydrocarbon migration and entrapment within faulted structures. *AAPG bulletin*, *73*(7), 803-811. https://doi.org/10.1306/44B4A271-170A-11D7-8645000102C1865D

Andersen, O., & Sundal, A. (2021). Estimating Caprock Impact on CO2 Migration in the Gassum Formation Using 2D Seismic Line Data. *Transport in porous media*, *138*(2), 459-487. https://doi.org/10.1007/s11242-021-01622-1

Anell, I., Thybo, H., & Rasmussen, E. (2012). A synthesis of Cenozoic sedimentation in the North Sea. *Basin Res*, *24*(2), 154-179. https://doi.org/10.1111/j.1365-2117.2011.00517.x

Badley, M. E., Price, J. D., Rambech Dahl, C., & Agdestein, T. (1988). The structural evolution of the northern Viking Graben and its bearing upon extensional modes of basin formation. *Journal of the Geological Society*, *145*(3), 455-472. https://doi.org/10.1144/gsjgs.145.3.0455

Barnett, J. A. M., Mortimer, J., Rippon, J. H., Walsh, J. J., & Watterson, J. (1987). Displacement geometry in the volume containing a single normal fault. *AAPG bulletin*, *71*(8), 925-937. https://doi.org/10.1306/948878ED-1704-11D7-8645000102C1865D

Bartholomew, I. D., Peters, J. M., & Powell, C. M. (1993). Regional structural evolution of the North Sea: Oblique slip and the reactivation of basement lineaments. *Petroleum Geology Conference Proceedings*, *4*(1), 1109-1122. https://doi.org/10.1144/0041109

Bell, R. E., Jackson, C. A. L., Whipp, P. S., & Clements, B. (2014). Strain migration during multiphase extension: Observations from the northern North Sea. *Tectonics*, *33*(10), 1936-1963. https://doi.org/10.1002/2014TC003551

Bjørlykke, K. (2010). *Petroleum Geoscience*. https://doi.org/10.1007/978-3-642-02332-3

Bouvier, J. D., Kaars-Sijpesteijn, C. H., Kluesner, D. F., Onyejekwe, C. C., & van der Pal, R. C. (1989). Three-dimensional seismic interpretation and fault sealing investigations, Nun River Field, Nigeria. *AAPG bulletin*, *73*(11), 1397-1414. https://doi.org/10.1306/44B4AA5A-170A-11D7-8645000102C1865D

Bretan, P., Yielding, G., & Jones, H. (2003). Using calibrated shale gouge ratio to estimate hydrocarbon column heights. *AAPG bulletin*, *87*(3), 397-413. https://doi.org/10.1306/08010201128

Bretan, P., Yielding, G., Mathiassen, O. M., & Thorsnes, T. (2011). Fault-seal analysis for CO2 storage: an example from the Troll area, Norwegian Continental Shelf. *Petroleum Geoscience*, *17*(2), 181-192. https://doi.org/10.1144/1354-079310-025

Christiansson, P., Faleide, J. I., & Berge, A. M. (2000). Crustal structure in the northern North Sea: an integrated geophysical study. *Geological Society special publication*, *167*(1), 15-40. https://doi.org/10.1144/GSL.SP.2000.167.01.02

Clarke, S. M., Burley, S. D., & Williams, G. D. (2005). A three-dimensional approach to fault seal analysis: fault-block juxtaposition argillaceous smear modelling. *Basin Research*, *17*(2), 269-288. https://doi.org/10.1111/j.1365-2117.2005.00263.x

Clausen, J. A., Gabrielsen, R. H., Reksnes, P. A., & Nysæther, E. (1999). Development of intraformational (Oligocene–Miocene) faults in the northern North Sea: influence of remote stresses and doming of Fennoscandia. *Journal of Structural Geology*, *21*(10), 1457-1475. https://doi.org/10.1016/S0191-8141(99)00083-8

Cosgrove, J. W. (2001). Hydraulic fracturing during the formation and deformation of a basin; a factor in the dewatering of low-permeability sediments. *AAPG bulletin*, *85*(4), 737-748. https://doi.org/10.1306/8626C997-173B-11D7-8645000102C1865D

Cunningham, J. E., Cardozo, N., Townsend, C., & Callow, R. H. T. (2021). The impact of seismic interpretation methods on the analysis of faults: A case study from the Snøhvit field, Barents Sea. *Solid earth (Göttingen)*, *12*(3), 741-764. https://doi.org/10.5194/se-12-741-2021

Davies, R. J., Turner, J. D., & Underhill, J. R. (2001). Sequential dip-slip fault movement during rifting; a new model for the evolution of the Jurassic trilete North Sea rift system. *Petroleum Geoscience*, *7*(4), 371-388. https://doi.org/10.1144/petgeo.7.4.371

Deegan, C. E., & Scull, B. J. (1977). A standard lithostratigraphic nomenclature for the Central and Northern North Sea. *Norwegian Petroleum Directorate Bulletin no. 1* https://www.nhm2.uio.no/norges/litho/Bulletinnr1.pdf

Deng, C., Fossen, H., Gawthorpe, R. L., Rotevatn, A., Jackson, C. A. L., & FazliKhani, H. (2017). *Influence of fault reactivation during multiphase rifting: The Oseberg area, northern North Sea rift* [1252-1272]. [Guildford, Surrey] :.

Dreyer, T., Whitaker, M., Dexter, J., Flesche, H., & Larsen, E. (2005). From spit system to tide-dominated delta: Integrated reservoir model of the upper Jurassic Sognefjord formation on the Troll West Field. *Petroleum Geology Conference Proceedings*, *6*(1), 423-448. https://doi.org/10.1144/0060423

Duffy, O. B., Bell, R. E., Jackson, C. A. L., Gawthorpe, R. L., & Whipp, P. S. (2015). Fault growth and interactions in a multiphase rift fault network: Horda Platform, Norwegian North Sea. *Journal of Structural Geology*, *80*, 99-119. https://doi.org/10.1016/j.jsg.2015.08.015

E. U. Comission. (2018, 28.11.2018). *Communication from the commission to the European parliament, the European Council, the Council, the European economic and social committee, the committee of the regions and the European investment bank. A Clean Planet all. A Eur. Strateg. long-term Vis. a prosperous* Brussels.

Egholm, D. L., Clausen, O. R., Sandiford, M., Kristensen, M. B., & Korstgard, J. A. (2008). The mechanics of clay smearing along faults. *Geology (Boulder)*, *36*(10), 787-790. https://doi.org/10.1130/G24975A.1

Equinor. (2019). *Northern Lights Project Concept report*. https://ccsnorway.com/app/uploads/sites/6/2020/05/Northern-Lights-Project-Concept-report.pdf

Færseth, R. B. (1996). Interaction of Permo-Triassic and Jurassic extensional fault-blocks during the development of the northern North Sea. *Journal of the Geological Society*, *153*, 931-944. https://doi.org/10.1144/gsjgs.153.6.0931

Færseth, R. B., Johnsen, E., & Sperrevik, S. (2007). Methodology for risking fault seal capacity; implications of fault zone architecture. *AAPG bulletin*, *91*(9), 1231-1246. https://doi.org/10.1306/03080706051

Faleide, J. I., Kyrkjebo, R., Kjennerud, T., Gabrielsen, R. H., Jordt, H., Fanavoll, S., & Bjerke, M. D. (2002). Tectonic impact on sedimentary processes during Cenozoic evolution of the northern North Sea and surrounding areas. *Geological Society special publication*, *196*(1), 235-269. https://doi.org/10.1144/GSL.SP.2002.196.01.14

Faleide, T. S., Braathen, A., Lecomte, I., Mulrooney, M. J., Midtkandal, I., Bugge, A. J., & Planke, S. (2021). Impacts of seismic resolution on fault interpretation: Insights from seismic modelling. *Tectonophysics*, *816*, 229008. https://doi.org/10.1016/j.tecto.2021.229008

Fawad, M., Rahman, M. D. J., & Mondol, N. H. (2021). Seismic reservoir characterization of potential CO2 storage reservoir sandstones in Smeaheia area, Northern North Sea. *Journal of petroleum science & engineering*, *205*, 108812. https://doi.org/10.1016/j.petrol.2021.108812

Fazlikhani, H., Aagotnes, S. S., Refvem, M. A., Hamilton-Wright, J., Bell, R. E., Fossen, H., Gawthorpe, R. L., Jackson, C. A. L., & Rotevatn, A. (2021). Strain migration during multiphase extension, Stord Basin, northern North Sea rift. *Basin Research*, *33*(2), 1474-1496. https://doi.org/10.1111/bre.12522

Fazlikhani, H., Fossen, H., Gawthorpe, R. L., Faleide, J. I., & Bell, R. E. (2017). Basement structure and its influence on the structural configuration of the northern North Sea rift. *Tectonics (Washington, D.C.)*, *36*(6), 1151-1177. https://doi.org/10.1002/2017TC004514

Fisher, Q. J., & Knipe, R. J. (1998). Fault sealing processes in silisiclastic sediments. *Geological Society, London, Special Publications*, *147*, 117-134.

Fisher, Q. J., & Knipe, R. J. (2001). The permeability of faults within siliciclastic petroleum reservoirs of the North Sea and Norwegian Continental Shelf. *Marine and Petroleum Geology*, *18*(10), 1063-1081. https://doi.org/10.1016/S0264-8172(01)00042-3

Fossen, H. (1992). The role of extensional tectonics in the Caledonides of south Norway. *Journal of Structural Geology*, *14*(8), 1033-1046. https://doi.org/10.1016/0191-8141(92)90034-T

Fossen, H., Khani, H. F., Faleide, J. I., Ksienzyk, A. K., & Dunlap, W. J. (2017). Post-Caledonian extension in the West Norway-northern North Sea region: The role of structural inheritance. *Geological Society special publication*, *439*(1), 465-486. https://doi.org/10.1144/SP439.6

Fossen, H., & Rotevatn, A. (2016). Fault linkage and relay structures in extensional settings—A review. *Earth-Science Reviews*, *154*, 14-28. https://doi.org/10.1016/j.earscirev.2015.11.014

Fossen, H., Schultz, R. A., Shipton, Z. K., & Mair, K. (2007). Deformation bands in sandstone; a review. *Journal of the Geological Society*, *164*(4), 755-769. https://doi.org/10.1144/0016-76492006-036

Freeman, B., Yielding, G., Needham, D. T., & Badley, M. E. (1998). Fault seal prediction: the gouge ratio method. *Geological Society special publication*, *127*(1), 19-123,125. https://doi.org/10.1144/GSL.SP.1998.127.01.03

Furre, A.-K., Eiken, O., Alnes, H., Vevatne, J. N., & Kiær, A. F. (2017). 20 Years of Monitoring CO2-injection at Sleipner. *Energy Procedia*, *114*, 3916-3926. https://doi.org/10.1016/j.egypro.2017.03.1523

Gabrielsen, R. H., Skurtveit, E., & Faleide, J. I. (2020). Caprock integrity of the Draupne Formation, Ling Depression, North Sea, Norway. *Norwegian Journal of Geology*. https://doi.org/10.17850/njg100-4-2

Gassnova. (2012). *Geological storage of CO2 from Mongstad. Interim report Johansen Formation*. https://ccsnorway.com/earlier-norwegian-ccs-projects/

Gauthier, B. D. M., & Lake, S. D. (1993). Probabilistic modeling of faults below the limit of seismic resolution in Pelican Field, North Sea, offshore United Kingdom. *AAPG bulletin*, *77*(5), 761-777. https://doi.org/10.1306/BDFF8D4E-1718-11D7-8645000102C1865D

Gee, D. G., Fossen, H., Henriksen, N., & Higgins, A. K. (2008). From the Early Paleozoic Platforms of Baltica and Laurentia to the Caledonide Orogen of Scandinavia and Greenland. *Episodes*, *31*(1), 44-51. https://doi.org/10.18814/epiiugs/2008/v31i1/007

Halland, E. K., Johansen, W. T., Riis, F., & Norge, O. (2011). *CO_2 storage atlas: Norwegian North Sea*. Norwegian Petroleum Directorate.

Hancock, N. J. (1992). Quick-look Lithology from logs. In *ME 10: Development Geology Reference Manual* (pp. 174-179). American Association of Petroleum Geologists. https://archives.datapages.com/data/specpubs/methodo1/data/a095/a095/0001/0150/0174.htm

Hansen, O., Gilding, D., Nazarian, B., Osdal, B., Ringrose, P., Kristoffersen, J.-B., Eiken, O., & Hansen, H. (2013). Snøhvit: The History of Injecting and Storing 1 Mt CO2 in the Fluvial Tubåen Fm. *Energy Procedia*, *37*, 3565-3573. https://doi.org/10.1016/j.egypro.2013.06.249

Holden, N. (2021). *Structural characterization and across-fault seal assessment of the Aurora CO2 storage site, northern North Sea* University of Oslo]. Oslo.

Holgate, N. E., Jackson, C. A. L., Hampson, G. J., & Dreyer, T. (2013). Sedimentology and sequence stratigraphy of the Middle-Upper Jurassic Krossfjord and Fensfjord Formations, Troll Field, northern North Sea. *Petroleum Geoscience*, *19*(3), 237-258. https://doi.org/10.1144/petgeo2012-039

Ingram, G. M., Urai, J. L., & Naylor, M. A. (1997). Sealing processes and top seal assessment. In (Vol. 7, pp. 165-174). Elsevier. https://doi.org/10.1016/S0928-8937(97)80014-8

Intergovernmental Panel on Climate Change. (2005). *Carbon Dioxide Capture and Storage*. C. U. Press.

International Energy Agency. (2013). *CO2 Emissions from Fuel Combustion 2013*. International Energy Agency. https://doi.org/https://doi.org/10.1787/co2_fuel-2013-en

Jackson, C. A. L., Bell, R. E., Rotevatn, A., & Tvedt, A. B. M. (2017). Techniques to determine the kinematics of synsedimentary normal faults and implications for fault growth models. *Geological Society special publication*, *439*(1), 187-217. https://doi.org/10.1144/SP439.22

Jev, B. I., Kaars-Sijpesteijn, C. H., Peters, M. P. A. M., Watts, N. L., & Wilkie, J. T. (1993). Akaso Field, Nigeria; use of integrated 3-D seismic, fault slicing, clay smearing, and RFT pressure data on fault trapping and dynamic leakage. *AAPG bulletin*, *77*(8), 1389-1404. https://doi.org/10.1306/BDFF8EA2-1718-11D7-8645000102C1865D

Jolley, S. J., Dijk, H., Lamens, J. H., Fisher, Q. J., Manzocchi, T., Eikmans, H., & Huang, Y. (2007). Faulting and fault sealing in production simulation models; Brent Province, northern North Sea. *Petroleum Geoscience*, *13*(4), 321-340. https://doi.org/10.1144/1354-079306-733

Karolyte, R., Johnson, G., Yielding, G., & Gilfillan, S. M. V. (2020). Fault seal modelling; the influence of fluid properties on fault sealing capacity in hydrocarbon and CO2 systems. *Petroleum Geoscience*, *26*(3), 481-497. https://doi.org/10.1144/petgeo2019-126

Kim, Y.-S., & Sanderson, D. J. (2005). *The relationship between displacement and length of faults: a review* [317-334]. Amsterdam :.

Knipe, R. J. (1997). Juxtaposition and Seal Diagrams to Help Analyze Fault Seals in Hydrocarbon Reservoirs. *AAPG bulletin*, *81*(2), 187-195. https://doi.org/DOI: 10.1306/522B42DF-1727-11D7-8645000102C1865D

Knox, R. W. O. B., & Morton, A. C. (1988). *The record of early Tertiary N Atlantic volcanism in sediments of the North Sea Basin* [407-419]. Oxford ; Boston :.

Koson, S., Chenrai, P., & Choowong, M. (2014). Seismic Attributes and Their Applications in Seismic Geomorphology. *Bulletin of Earth Sciences of Thailand*, *6*, 1-9.

Kyrkjebo, R., Gabrielsen, R. H., & Faleide, J. I. (2004). Unconformities related to the Jurassic-Cretaceous synrift-post-rift transition of the northern North Sea. *Journal of the Geological Society*, *161*(1), 1-17. https://doi.org/10.1144/0016-764903-051

Lauritsen, H., Kassold, S., Meneguolo, R., Furre, A.-K., & Equinor. (2018). *Assessing Potential Influence of Nearby Hydrocarbon Production On CO2 Storage At Smeaheia* Fifth CO2 Geological Storage Workshop, Utrecht, Netherlands.

Lervik, K.-S. (2006). Triassic lithostratigraphy of the Northern North Sea Basin. *Norsk Geologisk Tidsskrift*, *86*(2), 93-115.

Lervik, K. S., Spencer, A. M., & Warrington, G. (1989). Outline of Triassic stratigraphy and structure in the central and northern North Sea. In J. D. Collinson, *Correlation in Hydrocarbon Exploration* Dordrecht.

Lindsay, N. G., Murphy, F. C., Walsh, J. J., & Watterson, J. (1993). Outcrop Studies of Shale Smears on Fault Surface. In *The Geological Modelling of Hydrocarbon Reservoirs and Outcrop Analogues* (pp. 113-123). Blackwell Scientific Publications. https://doi.org/https://onlinelibrary.wiley.com/doi/10.1002/9781444303957.ch6

Lohr, T., Krawczyk, C. M., Tanner, D. C., Samiee, R., Endres, H., Thierer, P. O., Oncken, O., Trappe, H., Bachmann, R., & Kukla, P. A. (2008). Prediction of subseismic faults and fractures; integration of three-dimensional seismic data, three-dimensional retrodeformation, and well data on an example of deformation around an inverted fault. *AAPG bulletin*, *92*(4), 473-485. https://doi.org/10.1306/11260707046

Lothe, A. E., Bergmo, P. E. S., & Grimstad, A.-A. (2019). *Storage Resources for Future European CCS Deployment; A Roadmap for a Horda CO2 Storage Hub, Offshore Norway*. SINTEF Academic Press.

Lyon, P. J., Boult, P. J., Mitchell, A., & Hillis, R. R. (2004, 19-22 September). *Improving Fault Geometry Interpretation through 'Pseudo-Depth' Conversion of Seismic Data in the Penola Trough, Otway Basin* Eastern Australasian Basin Symposium II, Adelaide.

Michie, E. A. H., Mulrooney, M. J., & Braathen, A. (2021). Fault interpretation uncertainties using seismic data, and the effects on fault seal analysis: a case study from the Horda Platform, with implications for CO<sub>2</sub> storage. *Solid Earth*, *12*(6), 1259-1286. https://doi.org/10.5194/se-12-1259-2021

Miocic, J. M., Johnson, G., & Bond, C. E. (2019). Uncertainty in fault seal parameters: implications for CO2 column height retention and storage capacity in geological CO2 storage projects. *Solid earth (Göttingen)*, *10*, 951-967. https://doi.org/10.5194/se-10-951-2019

Mulrooney, M. J., Osmond, J. L., Skurtveit, E., Faleide, J. I., & Braathen, A. (2020). Structural analysis of the Smeaheia fault block, a potential CO2 storage site, northern Horda

Platform, North Sea. *Marine and Petroleum Geology*, *121*. https://doi.org/10.1016/j.marpetgeo.2020.104598

Nazarian, B., Thorsen, R., & Ringrose, P. (2018). *Storing CO2 in a reservoir under continuous pressure depletion: A simulation study* 14th international Conference on Greenhouse Gas Control Technologies (GHGT-14), Melbourne, Australia.

Nelson, R. A., Patton, T. L., Serra, S., Beaumont, E. A., & Foster, N. H. (1999). Exploring for Structural Traps. In *Exploring for Oil and Gas Traps* (Vol. 3, pp. 0). American Association of Petroleum Geologists. https://doi.org/10.1306/TrHbk624C21

Nicol, A., Walsh, J., Berryman, K., & Nodder, S. (2005). Growth of a normal fault by the accumulation of slip over millions of years. *Journal of Structural Geology*, *27*(2), 327-342. https://doi.org/10.1016/j.jsg.2004.09.002

NPD. (2019). *Tørr brønn nær Troll-feltet i Nordsjøen – brønn 32/4-3 S*. Norwegian Petroleum Directorate. Retrieved 02.05.2022 from https://www.npd.no/fakta/nyheter/Resultat-av-leteboring/2019/torr-bronn-nar-troll-feltet-i-nordsjoen--bronn-324-3-s/

Odinsen, T., Reemst, P., Beek, P. V. D., Faleide, J. I., & Gabrielsen, R. H. (2000). Permo-Triassic and Jurassic extension in the northern North Sea: results from tectonostratigraphic forward modelling. *Geological Society special publication*, *167*(1), 83-103. https://doi.org/10.1144/GSL.SP.2000.167.01.05

Osmond, J. L., Mulrooney, M. J., Holden, N., Skurtveit, E., Faleide, J. I., & Braathen, A. (2021). Structural traps and seals for expanding CO2 storage in the northern Horda Platform, North Sea. https://doi.org/https://doi.org/10.31223/X5534H

Ottesen Ellevset, S., Knipe, R. J., Svava Olsen, T., Fisher, Q. J., & Jones, G. (1998). Fault controlled communication in the Sleipner Vest Field, Norwegian Continental Shelf; detailed, quantitative input for reservoir simulation and well planning. *Faulting, Fault Sealing and Fluid Flow in Hydrocarbon Reservoirs*, *147*(1), 283-297. https://doi.org/10.1144/GSL.SP.1998.147.01.19

Peacock, D. C. P., & Sanderson, D. J. (1991). Displacements, segment linkage and relay ramps in normal fault zones. *Journal of Structural Geology*, *13*(6), 721-733. https://doi.org/10.1016/0191-8141(91)90033-F

Pei, Y., Paton, D. A., Knipe, R. J., & Wu, K. (2015). A review of fault sealing behaviour and its evaluation in siliciclastic rocks. *Earth-Science Reviews*, *150*, 121-138. https://doi.org/10.1016/j.earscirev.2015.07.011

Phillips, T. B., Fazlikhani, H., Gawthorpe, R. L., Fossen, H., Jackson, C. A. L., Bell, R. E., Faleide, J. I., & Rotevatn, A. (2019). The Influence of Structural Inheritance and

Multiphase Extension on Rift Development, the NorthernNorth Sea. *Tectonics (Washington, D.C.)*, *38*(12), 4099-4126. https://doi.org/10.1029/2019TC005756

Pigott, J. D., Kang, M.-H., & Han, H.-C. (2013). First order seismic attributes for clastic seismic facies interpretation: Examples from the East China Sea. *Journal of Asian earth sciences*, *66*, 34-54. https://doi.org/10.1016/j.jseaes.2012.11.043

Rawson, P. F., & Riley, L. A. (1982). Latest Jurassic-Early Cretaceous events and the "late Cimmerian unconformity" in North Sea area. *AAPG bulletin*, *66*(12), 2628-2648. https://doi.org/10.1306/03B5AC87-16D1-11D7-8645000102C1865D

Ringrose, P. S., Furre, A.-K., Gilfillan, S. M. V., Krevor, S., Landrø, M., Leslie, R., Meckel, T., Nazarian, B., & Zahid, A. (2021). Storage of Carbon Dioxide in Saline Aquifers: Physicochemical Processes, Key Constraints, and Scale-Up Potential. *Annu Rev Chem Biomol Eng*, *12*(1), 471-494. https://doi.org/10.1146/annurev-chembioeng-093020-091447 (Annual Review of Chemical and Biomolecular Engineering)

Roksandic, M. M. (1978). SEISMIC FACIES ANALYSIS CONCEPTS. *Geophysical Prospecting*, *26*(2), 383-398. https://doi.org/10.1111/j.1365-2478.1978.tb01600.x

Rotevatn, A., Jackson, C. A. L., Tvedt, A. B. M., Bell, R. E., & Blækkan, I. (2019). How do normal faults grow? *Journal of Structural Geology*, *125*, 174-184. https://doi.org/10.1016/j.jsg.2018.08.005

Steel, R. J. (1993). Triassic-Jurassic megasequence stratigraphy in the Northern North Sea: Rift to post-rift evolution. *Petroleum Geology Conference Proceedings*, *4*(1), 299-315. https://doi.org/10.1144/0040299

Stewart, S. A. (2001). Displacement distributions on extensional faults; implications for fault stretch, linkage, and seal. *AAPG bulletin*, *85*(4), 587-599. https://doi.org/10.1306/8626C951-173B-11D7-8645000102C1865D

Ter Voorde, M., Faerseth, R. B., Gabrielsen, R. H., & Cloetingh, S. A. P. L. (2000). Repeated lithosphere extension in the northern Viking Graben: a coupled or a decoupled rheology? *Geological Society special publication*, *167*(1), 59-81. https://doi.org/10.1144/GSL.SP.2000.167.01.04

Tonstad, D. I. K. (1989). A revised Cretaceous and Tertiary lithostratigraphic nomeclature for the Norwegian North Sea. *Norwegian Petroleum Directorate Bulletin no. 5*. https://www.npd.no/globalassets/1-npd/publikasjoner/npd-bulletins/npd-bulletin-5-1989.pdf

Underhill, J. R., & Partington, M. A. (1993). Jurassic thermal doming and deflation in the North Sea: Implications of the sequence stratigraphic evidence. *Petroleum Geology Conference Proceedings*, *4*(1), 337-345. https://doi.org/10.1144/0040337

Vetti, V. V., & Fossen, H. (2012). Origin of contrasting Devonian supradetachment basin types in the Scandinavian Caledonides. *Geology (Boulder)*, *40*(6), 571-574. https://doi.org/10.1130/G32512.1

Vollset, J., & Doré, A. G. (1984). A revised Triassic and Jurassic lithostratigraphic nomeclature for the Norwegian North Sea. *Norwegian Petroleum Directorate Bulletin 3*. https://www.npd.no/globalassets/1-npd/publikasjoner/npd-bulletins/npd-bulletin-3-1984.pdf

Vrolijk, P., Maze, W., Teletzke, G., & Jones, T. E. (2011). Subsurface CO2 storage in geologic traps–Procedures for evaluating trap adequacy. *Energy Procedia*, *4*, 4617-4624. https://doi.org/10.1016/j.egypro.2011.02.421

Walsh, J. J., Nicol, A., & Childs, C. (2002). An alternative model for the growth of faults. *Journal of Structural Geology*, *24*(11), 1669-1675. https://doi.org/10.1016/S0191-8141(01)00165-1

Walsh, J. J., & Watterson, J. (1987). Distributions of cumulative displacement and seismic slip on a single normal fault surface. *Journal of Structural Geology*, *9*(8), 1039-1046. https://doi.org/10.1016/0191-8141(87)90012-5

Weibull, W., Mienert, J., Bünz, S., & Hustoft, S. (2010). Fluid migration directions inferred from gradient of time surfaces of the sub seabed. *Marine and Petroleum Geology*, *27*(9), 1898-1909. https://doi.org/10.1016/j.marpetgeo.2010.07.014

Whipp, P. S., Jackson, C. A. L., Gawthorpe, R. L., Dreyer, T., & Quinn, D. (2014). Normal fault array evolution above a reactivated rift fabric; a subsurface example from the northern Horda Platform, Norwegian North Sea. *Basin Res*, *26*(4), 523-549. https://doi.org/10.1111/bre.12050

Wrona, T., Magee, C., Jackson, C. A. L., Huuse, M., & Taylor, K. G. (2017). Kinematics of polygonal fault systems: Observations from the northern north sea. *Frontiers in earth science (Lausanne)*, *5*. https://doi.org/10.3389/feart.2017.00101

Wu, L., Thorsen, R., Ottesen, S., Meneguolo, R., Hartvedt, K., Ringrose, P., & Nazarian, B. (2021). Significance of fault seal in assessing CO2 storage capacity and containment risks – an example from the Horda Platform, northern North Sea. *Petroleum Geoscience*, *27*(3). https://doi.org/10.1144/petgeo2020-102

Xu, G., & Haq, B. U. (2022). Seismic facies analysis: Past, present and future. *Earth-Science Reviews*, *224*, 103876. https://doi.org/10.1016/j.earscirev.2021.103876

Yielding, G., Bretan, P., & Freeman, B. (2010). Fault seal calibration: a brief review. *Geological Society special publication*, *347*(1), 243-255. https://doi.org/10.1144/SP347.14

Yielding, G., Freeman, B., & Needham, D. T. (1997). Quantitative fault seal prediction. *AAPG bulletin*, *81*(6), 897-917. https://doi.org/10.1306/522B498D-1727-11D7-8645000102C1865D

Yielding, G., Needham, T., & Jones, H. (1996). Sampling of fault populations using sub-surface data: a review. *Journal of Structural Geology*, *18*(2), 135-146. https://doi.org/10.1016/S0191-8141(96)80039-3

Yielding, G., Øverland, J. A., & Byberg, G. (1999). Charcterization of fault zones for reservoir modeling: an example from the Gullfaks field, northern North Sea. *AAPG bulletin*, *83*(6), 925-951.

Ziegler, P. A. (1975). Geologic Evolution of North Sea and Its Tectonic Framework. *The American Association of Pelroleum Geologists Bulletin*, *59*, 1073-1097.

Ziegler, P. A. (1982). Triassic rifts and facies patterns in Western and Central Europe. *Geologische Rundschau*, *71*(3), 747-772. https://doi.org/10.1007/BF01821101